

Project Number: ME – CF –MO08

MINIATURIZATION OF AN OPTOELECTRONIC HOLOGRAPHIC OTOSCOPE FOR  
MEASUREMENT OF NANODISPLACEMENTS IN TYMPANIC MEMBRANES

A Major Qualifying Project Report

Submitted to the Faculty

of the

WORCESTER POLYTECHNIC INSTITUTE

in partial fulfillment of the requirements for the

Degree of Bachelor of Science

in Mechanical Engineering

by

---

Geoffrey Karasic

---

Nathan Largesse

---

Lucas Samuel Lincoln

Date: 30 April, 2009

Keywords:

1. laser interferometry
2. tympanic membrane
3. ray tracing

---

Professor Cosme Furlong

## **Abstract**

A first generation optoelectronic holographic otoscope (OEHO) is currently in use in a major hospital. The OEHO allows for nanometer-displacement measurements of the deformation of mammalian tympanic membrane (TM) under acoustic stimulation and consists of a laser delivery system, an optical head, a data acquisition PC, and an acoustic excitation system. The optical head in the current system is sufficient for laboratory use, but requires improved thermomechanical stability, depth of field, and focusing ability to be suitable for the clinic. Additionally, the medical doctors working with the current device have indicated miniaturization and improved ease of use are necessary for full-scale clinical deployment.

In this project, in order make the improvements required for clinical deployment, the optical and biomechanical properties of the tympanic membrane are reviewed; design parameters determined; and a design synthesized with the aid of ray tracing analysis and consideration of optical characteristics. An optical head is prototyped, the optical performance is quantified and the device is validated through comparison of measured data with analytical and computational solutions. Measurements of a post-mortem chinchilla membrane are used to compare the device performance to the previous generation.

The resulting optical head has an improved depth of field, focusing ability; and reduced size compared to the previous generation. Drawbacks of the design are discussed and recommendations are made for future work.

## **Acknowledgements**

The group would like to thank Professor Cosme Furlong for his dedication, guidance, and expertise throughout the duration of this project. We also would like to acknowledge the graduate and post-graduate students working beside us in the Center for Holographic Studies and Laser micro-mechaTronics for their assistance and instruction. We are also thankful for Dr. Rosowski of the Massachusetts Eye and Ear Infirmary for his time, efforts, and feedback; and to Adriana Hera for her endless knowledge and support.

Lastly, we are grateful to the Mechanical Engineering Department of Worcester Polytechnic Institute for the opportunity and privilege to work on a challenging, state-of-the-art project.

# Table of Contents

Abstract .....	i
Acknowledgements .....	ii
List of Figures .....	vi
List of Tables .....	viii
1. Introduction .....	9
2. Tympanic Membrane Function, Histology, and Characteristics .....	11
2.1. Function of Tympanic Membrane .....	11
2.2. Physical Characteristics of the Tympanic Membrane .....	12
2.2.1. Young's Modulus .....	14
2.3. Histology of the Tympanic Membrane .....	14
2.4. Hearing Capabilities and Vibration Modes .....	19
2.5. Techniques for Studying Displacements .....	21
2.5.1. Clinical Relevance for Studying Displacements .....	21
2.5.2. State of the Art .....	21
2.5.3. Mathematical Models of the Tympanic Membrane .....	22
2.5.4. Design Requirements for an Optical System .....	24
2.6. Light Tissue Interactions .....	24
2.7. Optical Characteristics .....	25
2.7.1. Reflection Spectra of the Human Tympanic Membrane .....	25
2.7.2. Coatings to Increase Reflectivity .....	27
3. Interferometry .....	29
3.1. Fundamentals .....	29
3.2. Double-exposure holography .....	30
3.3. Time-averaged holography .....	32
4. Previous Work .....	35
4.1. Laser Delivery System .....	36
4.2. Optical Head .....	37
4.3. Image Processing Software .....	38
4.4. Performance of Previous Generation .....	39
5. Objective .....	40
6. Computer Modeling .....	42
6.1. Ray Tracing Principles .....	43
6.2. Ray Tracing Computational Model .....	47

7. Optical Head Configuration .....	50
8. Realization .....	54
8.1. Building the Prototype .....	54
8.2. Characterization of Optical Performance.....	56
8.2.1. Field of View .....	56
8.2.2. Magnification.....	57
8.2.3. Resolution .....	59
8.2.4. Depth of Field .....	60
8.2.5. Image Aberration .....	63
9. Validation.....	66
9.1. Analytical Validation .....	66
9.2. Computational Validation .....	72
9.3. Experimental Validation .....	74
9.3.1. Experimental Procedure.....	74
9.3.2. Experimental Results .....	76
9.4. Validation Results Comparison .....	78
10. Testing.....	79
11. Recommendations and Future Work.....	83
12. References.....	85
13. Appendix A. Biology Summary – Human TM.....	88
14. Appendix B. TracePro Model Details.....	89
14.1. Introduction to TracePro .....	90
14.1.1. Defining Geometry and Optical Characteristics .....	90
14.1.2. Light sources and ray trace options.....	95
14.1.3. Tracing Rays and Analysis Tools .....	101
14.2. Oscope Head Model Details .....	107
14.2.1. GRIN Lens ILW .....	107
14.2.2. GRIN ROD .....	108
14.2.3. Imaging Lens Achromat.....	111
14.2.4. Beamsplitter Cube.....	116
14.2.5. Optical Fibers.....	119
14.2.6. CMOS sensor chip .....	122
15. Appendix C. Optical Characterization Details.....	123
15.1. Resolution Algorithm.....	123
15.2. Depth of Field Algorithm.....	124

15.3. Image Aberration Algorithm.....	125
16. Appendix D. Component Specifications.....	128
16.1. GRIN Lens .....	129
16.2. 5mm Diameter Imaging Lens .....	131
16.3. 6.35mm Diameter Imaging Lens .....	135
16.4. Beam Splitter .....	139
16.5. Patch Cable .....	142
16.6. si1280 Camera .....	144

## List of Figures

Fig. 1. Components of middle ear.....	11
Fig. 2. Tympanic membrane to stapes area ratio <sup>2</sup> .....	12
Fig. 3. Human tympanic membrane showing two parts <sup>7</sup> .....	13
Fig. 4. Relative sizes of mammalian tympanic membranes <sup>9</sup> .....	14
Fig. 5. Two sections of human tympanic membrane. Upper - Pars Flaccida. Lower - Pars Tensa. ..	15
Fig. 6. Artist's conception of the migrating pattern of the epidermis in the tympanic membrane of humans and guinea pigs <sup>11</sup> .....	17
Fig. 7. A SEM photomicrograph of the outer radial and inner circular fibers and the parabolic fibers in the fibrous layer of the para tensa <sup>11</sup> .....	18
Fig. 8. Artist's conception of the fiber arrangement of the human tympanic membrane. SP: short process of the malleus; U: umbo; TIR: trigonum interradiale; C: circular fibers; R(1): radial fibers which attach straight into the annular ring; R(2): a few radial fibers which cross paths; T: transverse fibers; P: parabolic fibers; SMR: sub-mucous fine radial fibers <sup>11</sup> .....	18
Fig. 9. Calculated Vibration Modes of Human TM at 80 dB SPL <sup>8</sup> .....	20
Fig. 10. Common Examples of Sound Pressure Levels.....	20
Fig. 11. Tympanic Membrane Displacement at approximately 0.5kHz; FEM (a) vs. Measured (b) <sup>8</sup> .....	23
Fig. 12. Reflection spectra of healthy human adult taken in vivo. <sup>23</sup> .....	26
Fig. 13. Schematic of the three OEHO subsystems.....	35
Fig. 14. Previously Developed Otoscope Head <sup>18</sup> .....	37
Fig. 15. Laboratory environment of previous generation.....	39
Fig. 16. Existing otoscope form,.....	41
Fig. 17. Flowchart of design process used.....	42
Fig. 18. Geometry of ray translation between two reference surfaces.....	44
Fig. 19. Geometry of refraction at a curved surface <sup>3</sup> .....	45
Fig. 20. Gaussian distribution through system; showing input, post imaging lens, and output on CMOS chip.....	49
Fig. 21. Schematic of the optical head showing object beam and reference beam optical fibers (OB and RB, respectively), gradient-index rod lens (GRIN), imaging lens achromat (IL), beam combiner cube (BC) and CMOS camera (CAM).....	50
Fig. 22. GRIN lens Pitch concept illustration.....	51
Fig. 23. Off-axis performance of achromatic doublet versus plano-convex lens.....	52
Fig. 24. Spectral response of SI-1280 Camera.....	53
Fig. 25. Miniaturized Otoscope Head.....	54
Fig. 26. Previous Generation Otoscope Head <sup>18</sup> (Left); Miniaturized Otoscope Head (Right).....	55
Fig. 27. Field of View And Magnification Image.....	57
Fig. 28. 1951 USAF Resolution Target.....	59
Fig. 29. Depth of Field Test.....	61
Fig. 30. Depth of Field Contrast Trace Graph.....	62
Fig. 31. Grid Distortion Target.....	63
Fig. 32. Distortion Function.....	64
Fig. 33. Prismatic Beam.....	66
Fig. 34. Finite Element Beam.....	72
Fig. 35. Cantilever Test Setup.....	74
Fig. 36. Nitrile Membrane Test Setup.....	79

Fig. 37. (a) Nitrile Membrane at 4.228kHz; (b) Nitrile Membrane at 10.66 kHz; (c) 3-D Representation of Nitrile Membrane at 10.66kHz. ....	80
Fig. 38. Chinchilla Test.....	81
Fig. 39. Time-Averaged Image of Chinchilla.....	81
Fig. 40. Annotated screenshot of TracePro environment.....	90
Fig. 41. TracePro: 'View' Menu.....	91
Fig. 42. TracePro: 'Insert' toolbar.....	91
Fig. 43. TracePro: 'Insert' dialog.....	91
Fig. 44. TracePro: Boolean toolbar.....	92
Fig. 45. TracePro: Example Model Tree.....	92
Fig. 46. TracePro: 'Apply Properties' dialog.....	93
Fig. 47. TracePro: Material Property Editor.....	94
Fig. 48. TracePro: Menu for editing of property data catalogs.....	95
Fig. 49. TracePro: Source Tree.....	96
Fig. 50. TracePro: 'Define' menu.....	96
Fig. 51. TracePro: Definition of a grid source.....	97
Fig. 52. TracePro: Accessing 'Raytrace Options'.....	98
Fig. 53. TracePro: 'Raytrace Options' Dialog.....	99
Fig. 54. TracePro: Importance Sampling target definition.....	101
Fig. 55. TracePro: 'Analysis' Toolbar.....	101
Fig. 56. TracePro: 'Ray Sorting' Dialog.....	102
Fig. 57. TracePro: Raytrace with no ray sorting.....	103
Fig. 58. TracePro: Ray trace with ray sorting, 'Selected Surface', enabled.....	104
Fig. 59. TracePro: Analysis Tool Buttons.....	104
Fig. 60. TracePro: Ray table excerpt.....	105
Fig. 61. TracePro: Sample Irradiance Map.....	105
Fig. 62. TracePro: Image of raytrace through ILW component, with characteristic result.....	108
Fig. 63. TracePro: Image of raytrace through SRL (ILW and Rod combination) component, with characteristic result.....	108
Fig. 64. TracePro: 'Apply Properties' dialog for Gradient Index definition.....	109
Fig. 65. TracePro: Selecting the step size of the gradient index.....	110
Fig. 66. Achromat diagram with variable convention.....	111
Fig. 67. TracePro: Image of raytrace through achromatic doublet component, with characteristic result.....	112
Fig. 68. TracePro: Building the achromat crown, showing the untrimmed surfaces.....	114
Fig. 69. TracePro: Building the achromat crown, showing the tube used to trim for diameter specification.....	115
Fig. 70. TracePro: Resulting achromat crown.....	115
Fig. 71. TracePro: Image of raytrace through beamsplitter component, with characteristic result.....	116
Fig. 72. TracePro: Construction of the BS cube, showing the base block and trimming rectangle.....	117
Fig. 73. TracePro: Beamsplitter prism.....	117
Fig. 74. TracePro: BS construction image, showing the three bodies required to create the splitter.....	118
Fig. 75. TracePro: Distribution plot and raytrace of grid source with Nufern 460HP optical fiber characteristics. Block for distribution monitoring.....	120
Fig. 76. TracePro: Grid source testing block.....	121

## List of Tables

Table 1. Contents of various mammalian tympanic membranes <sup>9</sup> .....	16
Table 2. Hearing Frequency Ranges of Different Mammalian Species. ....	19
Table 3. Illustrative component ray traces and construction notes. ....	48
Table 4. Analytically Determine Natural Frequencies.....	71
Table 5. Finite Element Modes of Cantilever. ....	73
Table 6. Experimental Modal Frequencies obtained with .....	77
Table 7. Analytical and Computational Percent Error. ....	78
Table 8. ILW Tracepro specifications.....	107
Table 9. GRIN rod TracePro parameters. ....	108
Table 10. AC050-010-A1 TracePro parameter table. ....	112
Table 11. Beamsplitter (BS010) TracePro parameter table. ....	116
Table 12. Grid Source parameters for Nufern 460HP optical fiber. ....	119
Table 13. SI1280 CMOS sensor parameter table.....	122

# 1. Introduction

The tympanic membrane (TM) is a component of the middle ear which helps transmit sound energy into psychoacoustic signals to provide the sensation of hearing. Despite its important and irreplaceable function in human and other mammalian bodies, the current understanding of the function of the TM leaves much to be desired. Diagnosis of hearing disorders and malfunction are almost exclusively performed via qualitative investigation of the membrane. The medical community has desired a tool for the quantitative measurement of the tympanic membrane's response to acoustic stimulus.

This desire was recently answered with the development of an opto-electronic holographic otoscope<sup>1</sup> (OEHO). This tool provides a full-field of view, video rate deformation measurement system of the tympanic membrane, and has a resolution on the order of nanometers. It is installed at the Massachusetts Eye and Ear Infirmary (MEEI) and has provided the medical professionals the ability to gather previously unavailable information on the response of mammalian tympanic membranes to acoustic stimulation.

This modern tool has proved an invaluable resource to the MEEI laboratory researchers, and a full scale clinical deployed is desired. The current generation requires a number of improvements prior to this clinical deployment, primarily a miniaturized size; an increased depth of field; an intuitive magnification and focusing system; and an increased thermomechanical stability.

The goal of this MQP, and the task described herein, was to redesign the OEHO in order to address these improvements. Special attention was paid to creating a device which requires little technical training and can be packaged in a otoscope-like package; while reducing the overall size of the OEHO and achieving better optical performance.

In order to achieve this task, the biology of the tympanic membrane was first investigated to understand the requirements of the system, as well as what potential difficulties are encountered by measuring a biological sample and how these can be addressed.

Following this, an optical configuration was developed utilizing existing optical design tools and auxiliary research. The configuration was designed to meet the constraints of the project as well as address the improvements indicated above.

Finally, the device was prototyped and evaluated, as well as validated through the comparison of analytical, computational, and experimental solutions to a known dynamic system. The device was used by the medical professionals at MEEI to measure the tympanic membrane deformations of a post-mortem chinchilla and conclusions and further improvements are described.

## 2. Tympanic Membrane Function, Histology, and Characteristics

### 2.1. Function of Tympanic Membrane

To understand the function and importance of the tympanic membrane, one must have a general knowledge of how a vibration in the air becomes a sound heard in the human brain. A sound wave travels into the ear via the auditory canal. It then contacts directly the tympanic membrane. It is here that the sound energy is transferred from a gas (air) medium to a solid (the tympanic membrane). This can be related to the opposite of how a loudspeaker functions<sup>2</sup>. The vibrating air causes the tympanic membrane to vibrate accordingly, in simple or complex patterns. Attached to the membrane is a bone, the malleus, which moves precisely as the membrane vibrates. Next, the energy passes through two additional bones, the incus and then the stapes. See Fig. 1. The energy moves from the footplate (end) of the stapes to the inner ear, now traveling through a fluid. The energy is channeled through the cochlea, the auditory input of the inner ear. The sound energy stimulates hair cells, which produce synaptic activity that evokes action potentials that travel down the cochlea and to the brain<sup>2</sup>.

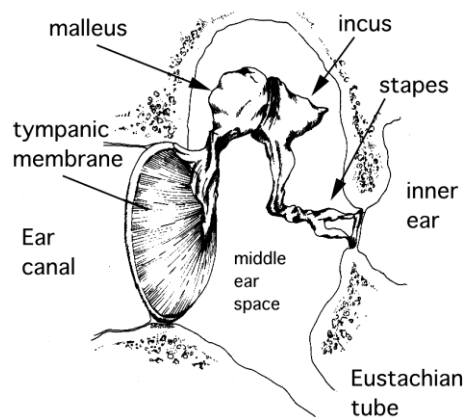


Fig. 1. Components of middle ear<sup>3</sup>.

Hearing requires the transfer of sound from a gaseous medium, to a solid, and finally a fluid, where it is translated into an electric potential<sup>4</sup>. If one can imagine listening to someone speak in air while submerged underwater, one can appreciate the brilliance of how the ear functions. The primary purpose of the tympanic membrane is to receive the sound energy from air, and then amplify it through solid tissue and bones. This amplification is possible due to what Katz calls the Areal relationship<sup>4</sup>. For the sake of explanation, ignore the malleus and incus bones, as they do little to affect the sound energy and only link the tympanic membrane to the stapes. The tympanic membrane has a much greater area (15 to 20 times) than the footplate of the stapes, the bone responsible for transmitting the sound energy into a fluid<sup>5</sup>. The sound pressure ( $P_{TM}$ ) acting on the TM produces a force ( $F$ ) equal to the product of the pressure and the TM area ( $A$ ). This force is conducted to the stapes footplate, which produces a pressure in the inner ear ( $P_S$ ) equal to the ratio of the force and the area of the footplate as described by the relationship  $P_S/P_{TM} = A_{TM}/A_S$ . This transformer process helps overcome the difference in impedance between air and cochlear fluid<sup>6</sup>, see Fig. 2.

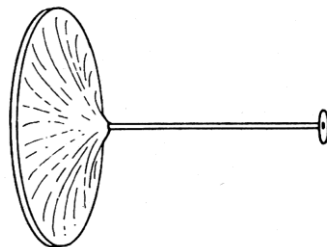


Fig. 2. Tympanic membrane to stapes area ratio<sup>2</sup>.

## ***2.2. Physical Characteristics of the Tympanic Membrane***

The human tympanic membrane is elliptical in shape. Tympanic membranes of all mammalian species consist of two parts: the Pars Flaccida and the Pars tensa, see Fig. 3. Although

there is variation in shape and size among humans, it is generally accepted that the horizontal axis is 9 to 10mm long and the vertical axis is 8 to 9mm long<sup>7</sup>. The approximate density of the tympanic membrane is 1200 kg/m<sup>3</sup><sup>8</sup>. The pars tensa portion of the tympanic membrane has an approximate thickness of 34µm and the pars flaccida portion measures approximately 110µm<sup>9</sup>. Very loud sounds produce a displacement of the TM up to 1µm<sup>4</sup>. Changes in pressure due to swallowing can produce displacements of up to 0.5mm<sup>6</sup>.

The size and shape of the tympanic membrane varies greatly in other mammalian species, see Fig. 4. In all species, the pars flaccida is thicker than the pars tensa. There are, however, large differences between species in regards to size and shape of the pars flaccid relative to the pars tensa<sup>9</sup>.

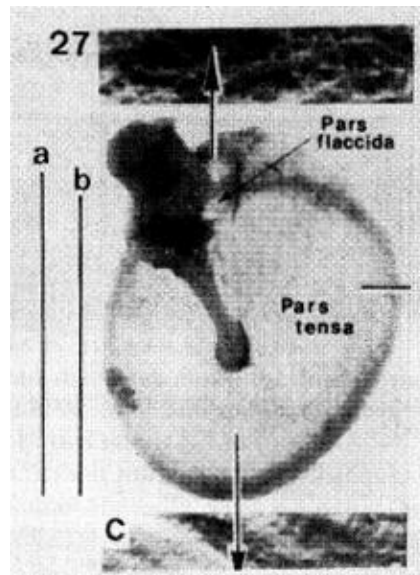


Fig. 3. Human tympanic membrane showing two parts<sup>7</sup>.

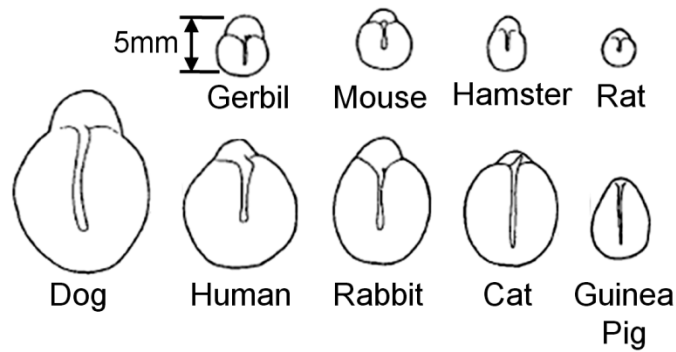


Fig. 4. Relative sizes of mammalian tympanic membranes<sup>9</sup>.

### 2.2.1. Young's Modulus

In humans, the data suggest that the elastic modulus of the TM lies in the range 0.1–0.3 GPa. This is unconfirmed, however, as recent experimental studies and mathematical models continue to produce different results. Mathematical models are based largely off of the known physical properties of collagen fibers. Experimental studies utilized both tension and bending tests of human tympanic membrane. The uncertainty in this area would suggest little confidence in the mathematical models said to represent the tympanic membrane as a whole. This suggests the usefulness of better tools for measuring deformations in the human tympanic membrane<sup>10</sup>.

### 2.3. *Histology of the Tympanic Membrane*

The ultra-structure of the TM is made up of four primary components: collagen, keratin, elastin, and mast cells. The pars flaccida and pars tensa of the human tympanic membrane are easily distinguishable from one another; The pars tensa contains tightly packed, highly ordered collagen bundles and the pars flaccida contains loose and inhomogeneous bundles. Collagen is a protein and is generally found in connective tissue in mammals. It exists as long fibers held together, forming a larger structure. Keratin, another fibrous protein, is found on the surface of both the pars tensa and pars flaccida. Elastin, a fibrous protein much like collagen, is found throughout the tympanic membrane in lesser amounts than collagen. Finally, mast cells are found in the pars flaccida and not

the pars tensa<sup>11</sup>. Mast cells are responsible for combating pathogens. A cross section of the human tympanic membrane is shown in Fig. 5.

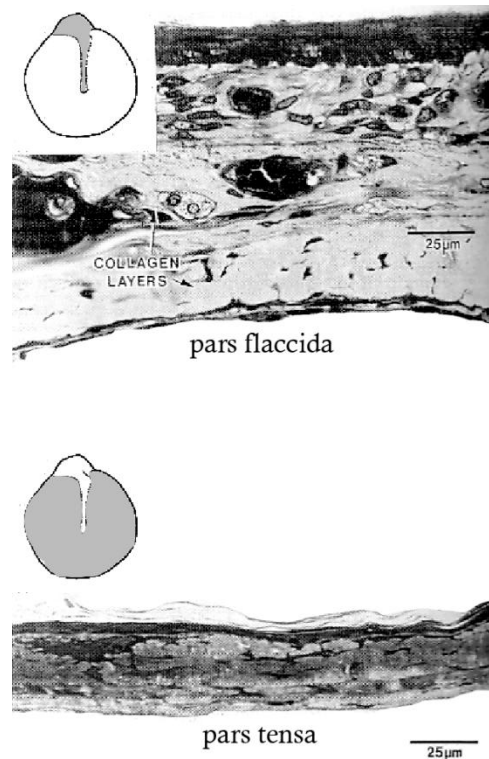


Fig. 5. Two sections of human tympanic membrane. Upper - Pars Flaccida. Lower - Pars Tensa<sup>12</sup>.

In other mammalian species, amounts and locations of these substances varied greatly. Mast cells were found in all tympanic membranes, suggesting their importance to the healthy maintenance of the tympanic membrane. A chart comparing the relative proportions of collagen, mast cells, keratin, and elastin species-to-species if found in Table 1. By further investigating the individual properties of these four materials, and also quantifying their amounts in the tympanic membrane, one could gain insight into mechanical and optical properties of the tympanic membrane in a number of species<sup>9</sup>.

Table 1. Contents of various mammalian tympanic membranes<sup>9</sup>.

PRESENCE OF VARIOUS SUBSTANCES IN TYMPANIC MEMBRANES					
	<i>Collagen</i>	<i>Elastin</i>	<i>Mast Cells</i>	<i>Macrophages</i>	<i>Keratin</i>
Human					
Pars flaccida	+	+	+	0	++
Pars tensa	++++	++	+	0	++
Dog					
Pars flaccida	+++	+	+	+	+++
Pars tensa	++++	+	0	0	++
Cat					
Pars flaccida	++	0	+	0	+++
Pars tensa	++++	0	+	+	++
Rabbit					
Pars flaccida	++	+	+	++	+
Pars tensa	++++	+	+	+	+
Guinea pig					
Pars flaccida	+	0	++	0	+
Pars tensa	++++	0	0	0	+
Rat					
Pars flaccida	+	0	+	+	++
Pars tensa	++++	0	0	0	+
Hamster					
Pars flaccida	+++	++	+	+	++
Pars tensa	++++	+	0	0	++
Gerbil					
Pars flaccida	+	+	++	+	++
Pars tensa	+++	++	0	0	+
Mouse					
Pars flaccida	+	0	+	0	++
Pars tensa	+++	+	0	0	+
Arbitrary scale indicates relative amounts.					

The tympanic membrane is composed of three distinct layers. The epidermis, mucosal epithelium, and lamina propria. The epidermis is a common keratinizing epithelium containing no hair follicles, glands, or other skin appendages. In humans, the epidermis slowly migrates away from the umbo towards the edges of the tympanic membrane. It is believed that this behavior is a method

of self cleaning, see Fig. 6. This is not necessarily the case for other mammalian species, as a different behavior has been observed in guinea pig tympanic membrane<sup>11</sup>.

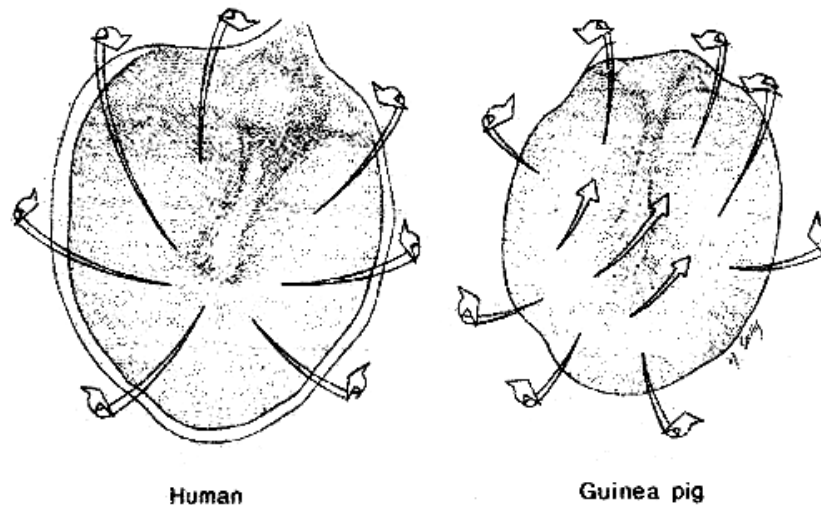


Fig. 6. Artist's conception of the migrating pattern of the epidermis in the tympanic membrane of humans and guinea pigs<sup>11</sup>.

The lamina propria is the largest layer of the tympanic membrane. It is largely consisting of loose connective tissue, collagen and elastic fibers. This layer is where mast cells are located, and it is responsible for the vascular and nerve supply to the tympanic membrane. Most importantly, the fibers in the lamina propria are arranged in a very particular way that determine the precise patterns the tympanic membrane creates when contacted by a sound. These fibers have been studied in a number of different methods including laser-Doppler-vibrometry and moiré shift interferometry<sup>11</sup>. The majority of fibers are categorized as either radial or circular, all centered around the umbo. A smaller number of transverse and parabolic fibers also are present, See Fig. 7 and Fig. 8 . It has also been observed that spontaneously healed tympanic membranes are unable to re-create these complex fiber layer accurately<sup>11</sup>.

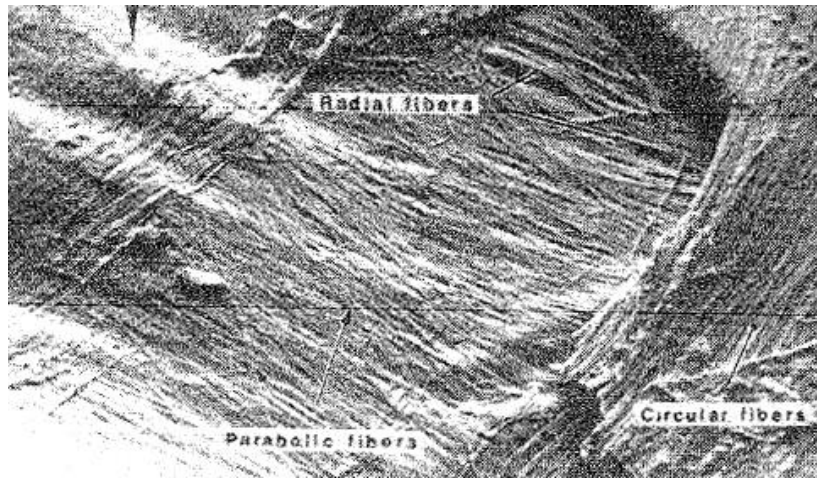


Fig. 7. A SEM photomicrograph of the outer radial and inner circular fibers and the parabolic fibers in the fibrous layer of the pars tensa<sup>11</sup>.

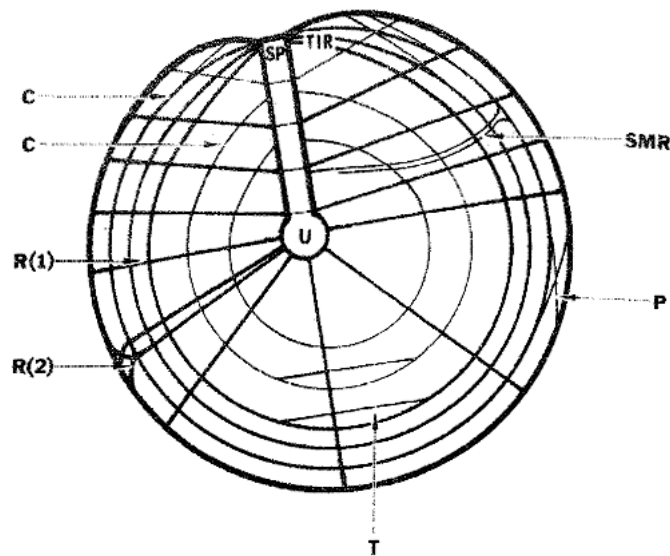


Fig. 8. Artist's conception of the fiber arrangement of the human tympanic membrane. SP: short process of the malleus; U: umbo; TIR: trigonum interradianale; C: circular fibers; R(1): radial fibers which attach straight into the annular ring; R(2): a few radial fibers which cross paths; T: transverse fibers; P: parabolic fibers; SMR: sub-mucous fine radial fibers<sup>11</sup>.

## 2.4. Hearing Capabilities and Vibration Modes

The human ear is capable of hearing frequencies of 16 to 20,000 Hz<sup>13</sup>. This range is different among other mammals, see

Table 2. The threshold for hearing is approximated at 0 dB SPL (sound pressure level). The maximum SPL for humans is 100 dB, as levels above 120 dB become damaging to the hair cells and can produce hearing loss<sup>5</sup>. Typical SPL levels for common situations are shown in Fig. 10.

The natural frequencies of the human tympanic membrane are not confirmed, however mathematical models have been used to calculate predicted these frequencies. Generally it is understood that vibration patterns rapidly become more complex at frequencies above 3 kHz<sup>14</sup>.

Williams and Lesser found using FEA the first six natural frequencies to be 1102.4 Hz, 1125.4 Hz, 1126.7 Hz, 1171.8 Hz, 1174.4 Hz, and 1236.9 Hz<sup>13</sup>. Examples of calculated natural frequencies and their respective vibration modes are shown in Fig. 9.

Table 2. Hearing Frequency Ranges of Different Mammalian Species<sup>15</sup>.

<b><u>Species</u></b>	<b><u>Lowest Frequency (Hz)</u></b>	<b><u>Highest Frequency (Hz)</u></b>
<b>Human</b>	16	20000
<b>Dog</b>	67	45000
<b>Cat</b>	45	64000
<b>Horse</b>	55	33500
<b>Rabbit</b>	360	42000
<b>Rat</b>	200	76000
<b>Mouse</b>	1000	91000
<b>Gerbil</b>	100	60000
<b>Guinea</b>		
<b>Pig</b>	54	50000
<b>Ferret</b>	16	44000
<b>Chinchilla</b>	90	22800
<b>Bat</b>	2000	110000
<b>Elephant</b>	16	12000

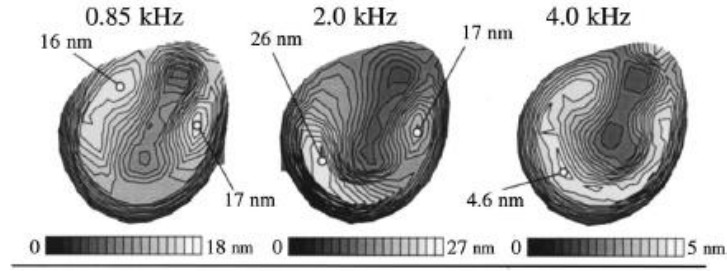


Fig. 9. Calculated Vibration Modes of Human TM at 80 dB SPL<sup>8</sup>.

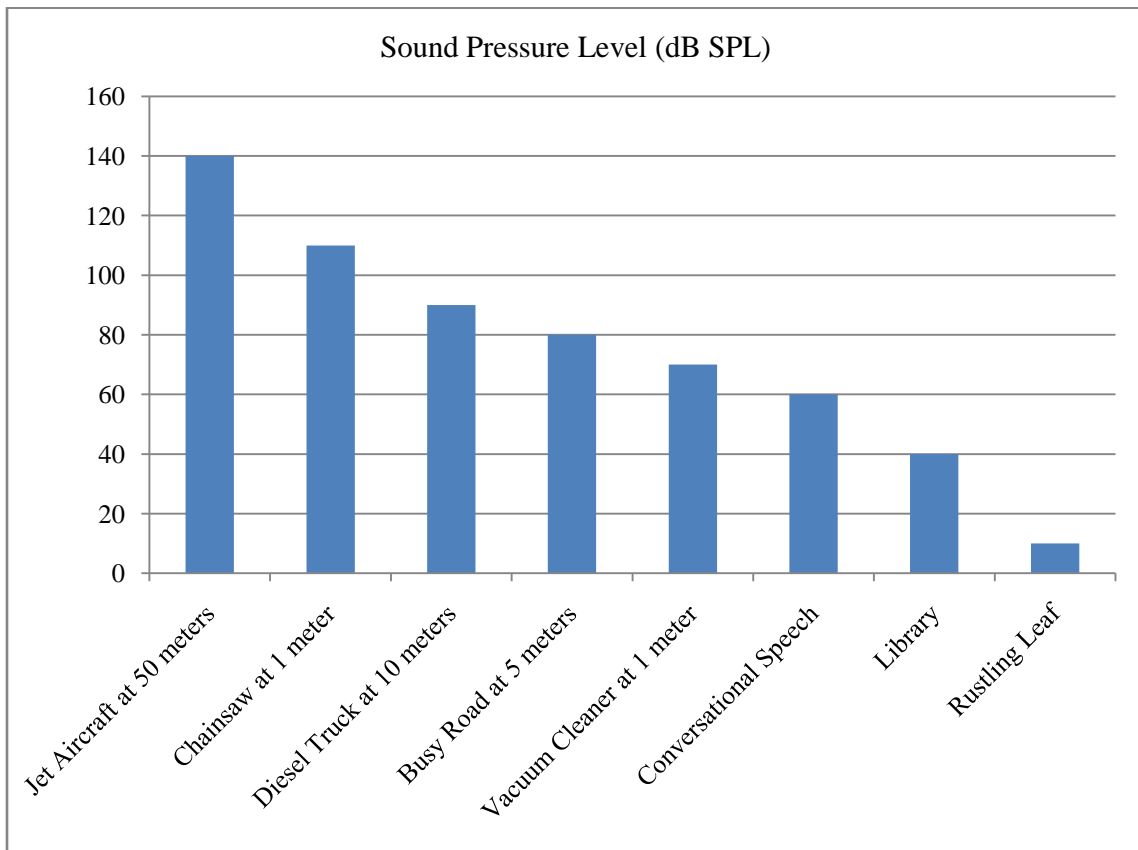


Fig. 10. Common Examples of Sound Pressure Levels<sup>16</sup>.

## ***2.5. Techniques for Studying Displacements***

### **2.5.1. Clinical Relevance for Studying Displacements**

Each year, doctors conduct tens of thousands of tympanoplasties, in which the tympanic membrane is reconstructed along with its ossicular connections. These procedures are often effective in curing and preventing ear disease, however many result in some level of hearing loss.

Tympanoplasties conducted alongside ossicular reconstructions produce hearing loss greater than 30 dB 50% of the time.

To better study the physical properties of the tympanic membrane and its vibration patterns and behaviors at different SPL's and frequencies, our device studies displacements of the tympanic membrane<sup>17</sup>.

### **2.5.2. State of the Art**

Tympanometry has been one means of examining the function of the tympanic membrane. A sound is applied to the tympanic membrane and a device is used to read the reflected sound. This sound can be compared against standards to evaluate the function of a specific tympanic membrane subject. Although this method accomplishes some objectives, it is very limited in close examination of the tympanic membrane, and provides no information in regards to vibration patterns or actual measures of displacement.

Laser Doppler Vibrometers (LDVi's) are the latest method for studying displacements in the tympanic membrane. This device measures the velocity of a surface using a laser, and from this data further information can be obtained. It was believed that this method would eliminate the need to conduct traditional tympanometry exam. This method is limited because it provides point by point

data. Scanning Laser Vibrometers (SLVi's) were developed to collect data from multiple points simultaneously. This test can only be conducted on a small area, however.<sup>18</sup>

The OEHO device has incredible clinical potential as it obtains quantitative displacement data of the entire tympanic membrane in real-time, visually demonstrating the vibration patterns and any other displacement behaviors.

### **2.5.3. Mathematical Models of the Tympanic Membrane**

Mathematical models have been developed for many important components of the human body. Models make it possible to, with some accuracy, predict how body parts will react to new scenarios. This is very important for doctors, scientists, and engineers, as it reduces the need for expensive and time-consuming experimental study. Many body parts, like the tympanic membrane, are very difficult to study in vivo. It is in these cases that mathematical models are most beneficial, and also most difficult to correctly develop. There is currently no model of any kind that accurately and reliably demonstrates the behavior of the tympanic membrane. Improved methods and tools for taking direct measurements of the tympanic membrane are required. Subjects of interest regarding the tympanic membrane include displacement measurements, special pressure distributions, and effects of pathologies<sup>8</sup>.

An analytical model of the tympanic membrane has been developed. Curvilinear shell equations were used in addition to the geometry and anisotropic ultrastructure of the tympanic membrane. Calculated vibration shapes resembled those experimentally acquired in cat tympanic membrane. This model is limited, however, as many geometric assumptions had to be made to reduce parameters. Also, because the asymptotic solution is linear, the model cannot be applied to high sound-pressure levels. Regardless, it is believed that this model can be applied to humans and other mammals with some accuracy<sup>19</sup>.

A number of studies have been conducted to model the tympanic membrane using the finite element method with limited success. Differences between the studies include the level of division of the tympanic membrane, other components of the outer and middle ear included in the model, and level of technology utilized in the development of the model. Presented in 2001 by Koike *et al* is a finite element model taking into account features of the middle ear previously omitted including ligaments, tendons, cavities, and the external auditory meatus. The tympanic membrane was divided up into two hundred and thirty-two triangular elements. There was also a focus on including the tympanic ring in the model, which suspends the membrane in place in the middle ear. This ring was modeled using linear and torsional springs<sup>8</sup>. Previously published values for Young's modulus and density were used. It was stated that this model is highly valid, as it accurately simulates the behavior of the middle ear. When compared with experimental measurements by Tonndorf and Khanna, it is demonstrated that there are clear differences between model and reality, see Fig. 11.

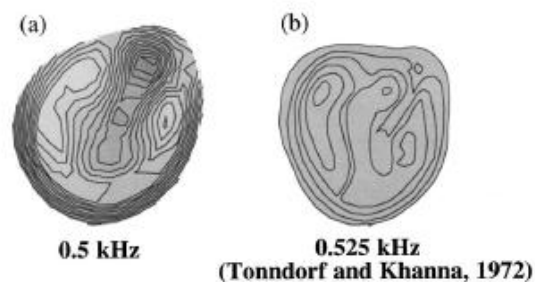


Fig. 11. Tympanic Membrane Displacement at approximately 0.5kHz; FEM (a) vs. Measured (b)<sup>8</sup>.

A mathematical model of the tympanic membrane is critical to advancements in middle-ear examination, repair, and general understanding. Existing models must be verified and further developed. An accurate, available tool to better measure displacement of the tympanic membrane is crucial to achieving these goals.

#### **2.5.4. Design Requirements for an Optical System**

To measure deformation of the tympanic membrane, the device must be able to measure a range of displacement of  $1\mu\text{m}$  in depth. In complex vibrations patterns, displacement differentiations as small as  $1\text{nm}$  are important, so the measuring resolution out-of-plane should be on the order of nanometers.

To view the human tympanic membrane in its entirety, and the vibration patterns, the field of view of the device should be  $10\text{mm} \times 10\text{mm}$ . This will ensure the full view of membranes regardless of orientation or variations in shape or size, all of which can differ between human subjects. This field of view will also accommodate mammals smaller than humans, with the possible exception of dogs.

How one stimulates the tympanic membrane for testing is very open. For humans, frequencies should be in the range of  $16$  to  $20,000\text{ Hz}$ <sup>12</sup>. Vibration patterns will become more complex at frequencies above  $3000\text{ Hz}$ . One should experiment with different sound-pressure levels to determine what is best for the given test. SPL should not exceed  $100\text{ dB}$ . Generally, tests conducted on human tympanic membrane in other studies utilize between  $40$  and  $100\text{ dB SPL}$ .

### ***2.6. Light Tissue Interactions***

Biological tissues are a challenge to study optically due to their in-homogeneity, multilayered structures, and the anisotropy of their physical characteristics. Strong light scattering is very common in biological tissues<sup>20</sup>. The Monte Carlo simulation technique is a method for directly calculating light distribution in skin or biological tissues. It uses the concept of multiple scattering in densely packed random media. A skin model was constructed by Tuchin including an epidermis, dermis, dermis with plexus superficialis, dermis, and finally dermis with plexus profundus. Different optical properties were used for each type of layer<sup>21</sup>. It is possible to improve OEHO designs with

the limited understanding of the optical characteristics of the tympanic membrane currently available. Future generations, however, could be produced much more rapidly, and predictably, if Monte Carlo simulation methods were used and a tympanic membrane model was developed.

## ***2.7. Optical Characteristics***

### **2.7.1. Reflection Spectra of the Human Tympanic Membrane**

Identifying the optical characteristics of the tympanic membrane is challenging due to its thickness of approximately 34 $\mu\text{m}$ , complex cellular composition, and deep seated location in the human body<sup>22</sup>. Like all biological tissues, the tympanic membrane is naturally an inhomogeneous light absorbing media. It has been found in reflectivity studies of the tympanic membrane that a large fraction of light directed at the membrane penetrates through. The reflectivity of the object behind the tympanic membrane therefore greatly influences measurements if not accounted for<sup>23</sup>.

A study by Doladov *et al* counter-screened the tympanic membrane with Indian black ink. The ink was applied to the middle ear cavity behind the membrane in both cadaveric and healthy subjects. This produced consistent results in the healthy specimens, shown in Fig. 12.

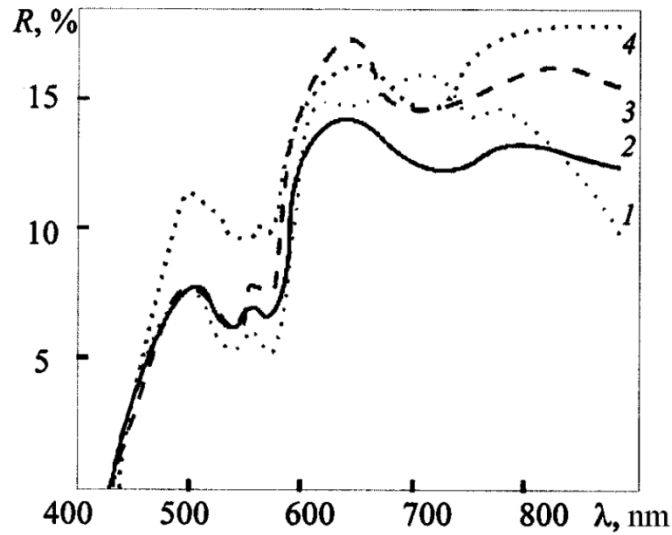


Fig. 12. Reflection spectra of healthy human adult taken in vivo.<sup>23</sup>

When reflectivity of the tympanic membrane is measured in vivo without consideration for the material behind the membrane, different results are observed<sup>23</sup>. Sundberg *et al* measured reflectivity in children both healthy and those affected by otitis media, a middle ear infection. It was shown that affected specimens can be distinguished from healthy specimens. The spectrum obtained through the study of the healthy tympanic membranes, however, clashed somewhat with the 2001 Dolodov study. In this case, the middle ear cavities were reflecting back naturally<sup>22</sup>.

Considering our device requires reflection of light from the tympanic membrane exclusively, and not the middle ear cavities behind, we have concluded that the reflectivity spectrum produced by the Dolodov study is more relevant to laser selection. Further, upon study of the Dolodov reflectivity spectrum, it can be concluded that a laser should be chosen with a wavelength between 600 and 700 nanometers, and as close to 650nm as possible.

### 2.7.2. Coatings to Increase Reflectivity

It has been hypothesized that powder or liquid coatings could be applied to the tympanic membrane to increase its reflectivity at all or one specific wavelength. Concerns for such a procedure include damaging the tympanic membrane or affecting the vibration patterns of the tympanic membrane in some way, invalidating data<sup>24</sup>.

Dirckx and Decraemer studied bronze powder, white Chinese ink, and magnesium oxide as coatings on tympanic membrane. Areas of examination included specular reflections, diffuse reflectivity, intensity distribution, and displacement of the tympanic membrane under static pressure both with and without coatings. All tests were conducted in vitro. For holographic measurement of the tympanic membrane, specular reflections should be minimized and diffuse reflection maximized. The tympanic membrane's surface must reflect light<sup>24</sup>.

White Chinese ink can be applied using a brush, or by spraying, which prevents direct contact with the sample. A disadvantage to a water-based ink is that it can crack upon drying, and is difficult to remove after an experiment. The use of white Chinese ink eliminated specular reflections, narrowed the intensity distribution of reflected light, and increased the mean reflected intensity by approximately 40%. It was shown that the 7.5 $\mu\text{m}$  layer had no measurable effect on the deformation of 50 $\mu\text{m}$  synthetic membrane at a static pressure of 2.5kPa at a resolution of 2.5 $\mu\text{m}$ . White Chinese ink is worthy of further investigation for use on human tympanic membrane<sup>24</sup>.

Magnesium oxide was applied by burning a wire of magnesium under the sample. The magnesium oxide smoke produced an opaque coating without touching the subject. It was found that this coating was easy to remove after the experiment. The magnesium oxide, like the Chinese ink, eliminated specular reflections, narrowed the intensity distribution of light and increased the mean reflected intensity by approximately 40%. The layer produced was approximately 17 $\mu\text{m}$  in thickness

and had no measurable effect on the deformation of the same synthetic membrane at a static pressure of 2.5kPa. Magnesium oxide also has potential for applications in holography and with the tympanic membrane<sup>24</sup>.

The bronze powder was chosen because it was first used by Tonndorf and Khanna in their historic paper studying the tympanic membrane. It was shown to be inferior to both white Chinese ink and magnesium oxide. The grain size of the bronze powder used was 1 $\mu$ m and it did eliminate specular reflections. It did not, however, narrow intensity distribution or increase mean reflected intensity<sup>24</sup>.

Due to the definitive results of these tests, it can be concluded that magnesium oxide and white Chinese ink should be further investigated for use with the OEHO.

## 3. Interferometry

### 3.1. Fundamentals

Interferometry is a method of measuring displacements, vibrations, temperature, pressure, and more based on the interference of light. When two light waves depart from the same origin but take paths of different lengths, they create fringes; or light and dark patterns; when they are recombined. A fringe represents a change in distance on the objects surface equal to one-half the wavelengths of the light used.

Classical interferometry required very controlled surfaces, limiting its versatility. When lasers became available, however, holographic interferometry opened new doors in nondestructive evaluation methods. In Holographic interferometry, light strikes an object from different locations, and is then reconstructed with interference. Fringe patterns (due to this interference) show how the object has moved. In near-ideal conditions, utilizing a highly reflective object and high-resolution CCD or CMOS camera, measurement resolution can be on the scale of nanometers.

Light, an electromagnetic wave, has two components perpendicular to one another: electric field and magnetic field. Holography only involves the electric field component, specifically, its intensity, which is defined

$$I = \epsilon v (E^2). \tag{3.1}$$

$I$  represents intensity.  $\epsilon$  represents the electric permittivity of the propagation medium.  $v$  is the velocity, and  $E^2$  represents the time-average of the electric field squared. For our purposes, we only require proportionality between  $I$  and  $E^2$ ,

$$I \propto (E^2). \tag{3.2}$$

Interference is generated when any number of waves from the same source interact. This results in a wave in a new, different direction, shown in Eq. 3.3 as,

$$E = E_1 + E_2. \quad (3.3)$$

The resultant intensity is shown as  $I$ ,

$$I = E^2 = E_1^2 + E_2^2 + 2(E_1 \cdot E_2). \quad (3.4)$$

Assuming two waves are polarized linearly in the same direction, electric field vectors for waves 1 and 2 are calculated using Eq. 3.5 and 3.6.

$$E_1 = A_1 \cos[\omega t - k_1 \cdot r] \quad (3.5)$$

$$E_2 = A_2 \cos[\omega t - k_2 \cdot r + \emptyset] \quad (3.6)$$

$A$  represents vector amplitude,  $\omega$  represents circular carrier frequency,  $t$  represents time,  $\emptyset$  is the relative phase between the two waves, and finally,  $k$  is the constant wave number  $(2\pi)/\lambda$ .

Combining Eq. 3.5 and 3.6, the resultant intensity of two overlapping electric fields is

$$I = A_1^2 + A_2^2 + 2A_1A_2 \cos[k_2 \cdot r - k_1 \cdot r - \emptyset]. \quad (3.7)$$

### ***3.2. Double-exposure holography***

Mechanical displacement data in double-exposure methods is based on light's optical path change, extracted from the interference patterns of two beams. The object beam,  $F_o$  is directed at the subject, and the reference beam,  $F_r$  is directed at the camera. The fields of light belonging to both beams are:

$$F_o = A_o \exp[i(\phi_o + \theta_n)], \quad (3.8)$$

$$F_r = A_r \exp[i(\phi_r)]. \quad (3.9)$$

The intensity of the combined wavefronts, recorded by the  $n^{\text{th}}$  video frame, is expressed in the Eq. 3.10. This is applicable after the beam splitter and considering phase stepping.

$$\begin{aligned}
I_n &= (F_o + F_r)(F_o + F_r)^* \\
&= \{A_o \exp[j(\phi_o + \theta_n)] + A_r \exp[j(\phi_r)]\} \{A_o \exp[-j(\phi_o + \theta_n)] + \\
&\quad A_r \exp(-j \phi_r)\} \\
&= |A_o|^2 + |A_r|^2 + 2A_o A_r \cos[(\phi_o - \phi_r) + \Delta\theta_n]
\end{aligned} \tag{3.10}$$

Amplitudes of objects and reference beams are shown as  $A_o$  and  $A_r$  respectively. The randomly changing phase of the object beam is shown as  $\phi_r$ , and the phase of the reference beam is  $\phi_o$ . The known phase step introduced between frames is shown as  $\Delta\theta$ . The periodic term from Eq.3.10 is used to facilitate double exposure investigations. It has been modified to include phase change due to deformations of the subject under study. The fringe-locas function ( $\Omega$ ) characterizes this phase change.

$$\begin{aligned}
\Omega(x,y) &= 2\pi n(x,y) = [\mathbf{K}_2(x,y) - \mathbf{K}_1(x,y)] \cdot \mathbf{L}(x,y) \\
&= \mathbf{K}(x,y) \cdot \mathbf{L}(x,y)
\end{aligned} \tag{3.11}$$

The interferometric fringe order at known location  $(x,y)$  is shown as  $n(x,y)$ ,  $\mathbf{K}$  represents the sensitivity vector, and lastly,  $\mathbf{L}$  is the displacement vector. Using Eq. 3.11 one can determine that the intensity  $I_n$  from the deformed object to be,

$$I_n = I_o + I_r + 2A_o A_r \cos[\Delta\phi + \Omega + \Delta\theta_n]. \tag{3.12}$$

In Eq. 3.12,  $\Delta\phi$  represents the random phase difference between fields  $\phi_o$  and  $\phi_r$ . Intensities of the object (constant) and reference beams are represented by  $I_o$  and  $I_r$  respectively. The mechanical data is contained in  $\Omega$ . Video processing software utilizes an algorithm to eliminate  $\Delta\phi$  from the

function by recording four images, or frames, each phase shifted 90 degrees from the prior. The computer solves two sets of four simultaneous equations. Using intensity modulated by the periodic function, with  $\Omega$  as its argument, an image and qualitative data is produced.

To view interference patterns at video frame rates, “display mode” is used, in which the patterns are modulated by Eq. 3.13. This mode is used specifically for adjusting the system for qualitative tests.

$$8A_0A_r \cos(\Omega/2) \quad (3.13)$$

To obtain quantitative results, “data mode” is used, utilizing Eq. 3.14 and 3.15. These two results are processed utilizing Eq. 3.16. Because this result is discontinuous, continuous spatial phase distribution data  $\Omega(x,y)$  is acquired using phase unwrapping algorithms.

$$D = 64A_0^2 A_r^2 \cos(\Omega) \quad (3.14)$$

$$N = 64 A_0^2 A_r^2 \sin(\Omega) \quad (3.15)$$

$$\Omega = \tan^{-1} (N/D) \quad (3.16)$$

### ***3.3. Time-averaged holography***

In Time-averaged holography, the subject of study undergoes a continuous vibration as a single holographic recording is taken. In this method, the fringe locus function  $\Omega_t(x,y,t)$  must be considered, as it relates to the sinusoidal vibration of the subject. Intensity distribution is calculated:

$$I_t(x,y,t) = I_0(x,y) + I_r(x,y) + 2A_0(x,y) A_r(x,y) \cos [\Delta\phi(x,y) + \Omega t(x,y,t) + \Delta\theta n]. \quad (3.17)$$

A CCD or CMOS camera reads average intensity at video frame rate of period  $\Delta t$ , therefore intensity observed is Eq. 3.18. Utilizing phase stepping, intensity distribution for the  $n^{\text{th}}$  frame is shown in Eq. 3.19.

$$I(x, y) = \frac{1}{\Delta t} \int_t^{t+\Delta t} I_t(x, y, t) dt \quad (3.18)$$

$$I_m(x, y) = I_o(x, y) + I_r(x, y) + 2A_o(x, y) A_r(x, y) \cos[\Delta\phi(x, y) + \Delta\theta n] M[\Omega_t(x, y)] \quad (3.19)$$

In Eq. 3.19 the term  $M[\Omega(x, y)]$  represents the characteristic function that modulates the interference of the two fields due to the agitation of the subject. The objective here is to determine  $\Omega_t(x, y)$  which can be related directly to movements in the subject. There are three other variables:  $I_o$ ,  $I_r$ , and  $\Delta\phi$ , which is eliminated using an algorithm in software. Four frames are obtained to solve for  $\Omega_t(x, y)$ , each one a 90 degree phase shift beyond the prior, Eq. 3.20. By evaluating these equations, an image is produced with intensity modulated by a periodic function,  $\Omega$  as the argument.

$$I_{t1} = I_t + I_r + 2A_o A_r \cos(\Delta\phi_t + 0^\circ) M(\Omega_t) \quad (3.20)$$

$$I_{t2} = I_t + I_r + 2A_o A_r \cos(\Delta\phi_t + 90^\circ) M(\Omega_t)$$

$$I_{t3} = I_t + I_r + 2A_o A_r \cos(\Delta\phi_t + 180^\circ) M(\Omega_t)$$

$$I_{t4} = I_t + I_r + 2A_o A_r \cos(\Delta\phi_t + 270^\circ) M(\Omega_t)$$

Time-averaged holography also has two modes, “display” and “data”. The display modulation function is shown as Eq. 3.21.

$$4A_o A_r |M(\Omega_t)| \quad (3.21)$$

Because time-averaged holography produces an infinite series, each term containing continuous phase information, it is very difficult to extract qualitative data in “data” mode. For this reason, Time-averaged holography is generally used for qualitative, image-based observations<sup>25</sup>.

## 4. Previous Work

The previous generation of this MQP<sup>18</sup>, in parallel with graduate-level projects, developed the OEHO to a functional device which was installed at the Massachusetts Eye and Ear Infirmary in Boston, Massachusetts.

The OEHO consists of three subsystems: The laser delivery system (LDS), the optical head, and the image processing computer.

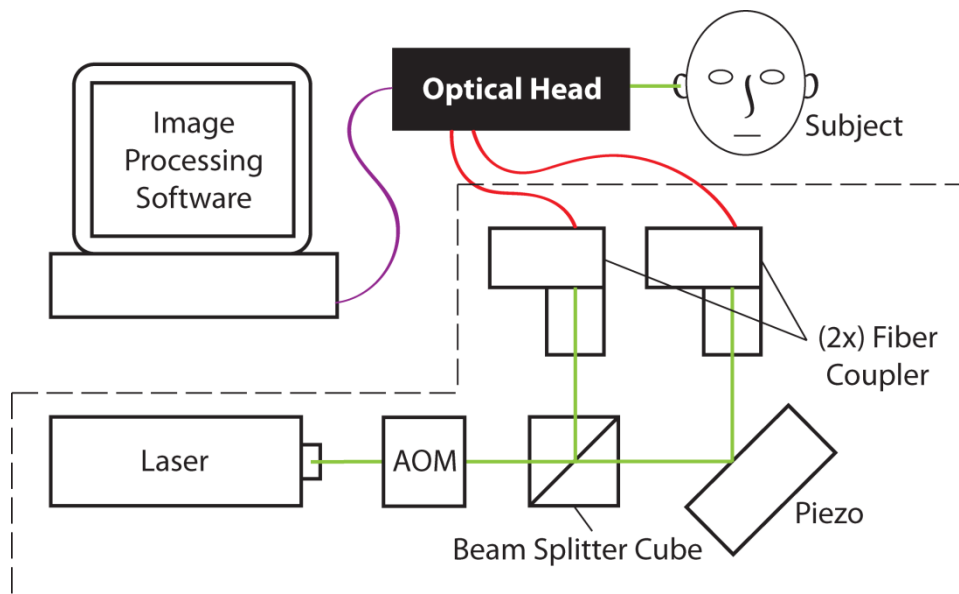


Fig. 13. Schematic of the three OEHO subsystems;  
Detailed laser delivery system in dashed box.

#### ***4.1. Laser Delivery System***

The laser delivery system is shown in Fig. 13 inside the dashed outline. It consists of a DPSS laser, acousto-optic modulator, beam splitter cube, piezoelectric phase shifter, and two five-axis fiber couplers. The basic function of each component will be discussed below in order to provide the necessary background for an understanding of the project.

The laser is a diode-pumped solid state, 473 nanometer wavelength laser with a 20mW output.

The acousto-optic modulator, or AOM, is used to strobe the laser light when stroboscopic illumination is desired. The AOM contains a quartz element, which the light is passed through, and a piezo-electric excitation system which passes an acoustic wave through the quartz. The wave causes localized variations in the refractive index of the quartz, deflecting the beam into several paths. The angle between these paths is typically measured in micro radians. By aligning the remaining optics to a particular output it is possible to create a strobing system varied by the acoustic signal input to the AOM transducer.

A standard 50/50 beam splitter cube is used to separate the beam into the object and reference paths.

A mirror attached to a stack-type piezo-translator provides the phase shifting of one beam, which is required to produce the solvable system of equations for optical phase measurements (Refer to the Interferometry section of this paper for more information).

Two fiber couplers are used to couple the light into single-mode optical fibers, which carry the light to the optical head.

## 4.2. Optical Head

The optical head is used to illuminate the tympanic membrane, image the reflected light, recombine the object and reference beams, record the interferograms, and provide an acoustic input for exciting the sample.

The previous generation optical head is shown in Fig. 14.

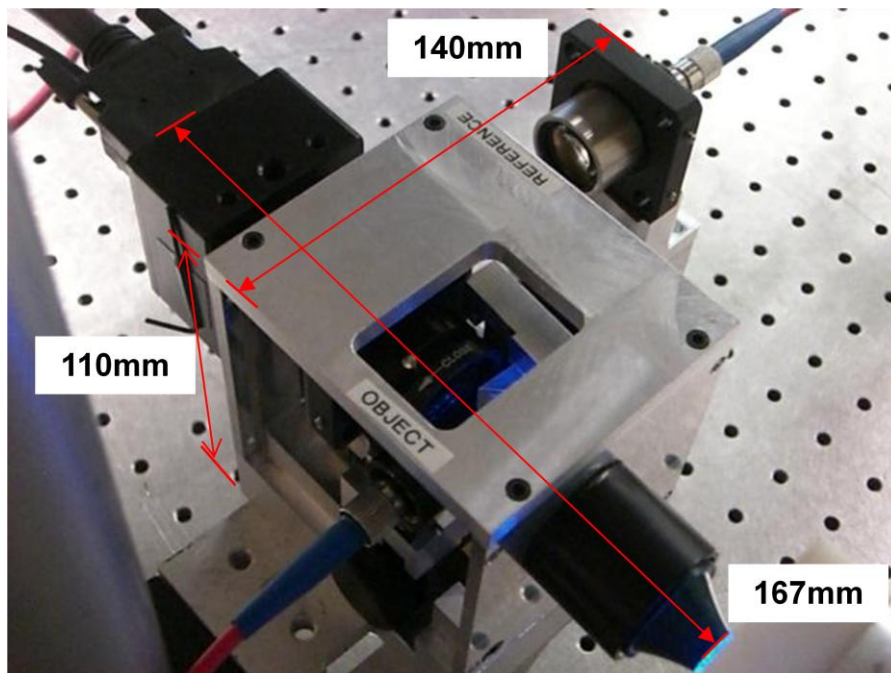


Fig. 14. Previously Developed Otoscope Head<sup>18</sup>.

Note the object and reference beams input via optical fibers from the LDS, as well as the otoscope speculum located in the bottom right of the figure. The camera for recording the interferograms is located in the top right of the photo. Nominal dimensions are shown.

### ***4.3. Image Processing Software***

The third subsystem is the image processing (IP) software, which performs the required algorithms for recording and displaying the interferograms. The IP also controls the phase shifting piezoelectric translator, the stroboscopic illumination (via the AOM), and the acoustic signal generation. The software has several view modes and can perform time-average and double-exposure measurement.

#### ***4.4. Performance of Previous Generation***

The generation of the OEHO device discussed in this section was installed at the Massachusetts Eye and Ear Infirmary to allow for measurements of tympanic membrane. The installation has been overall successful and has allowed for the gathering of data on numerous tympanic membranes, including normal and pathological samples from various small mammals and cadaveric humans.

The performance of the system has proved adequate for the laboratory use. The system and its environment is shown in Fig. 15.

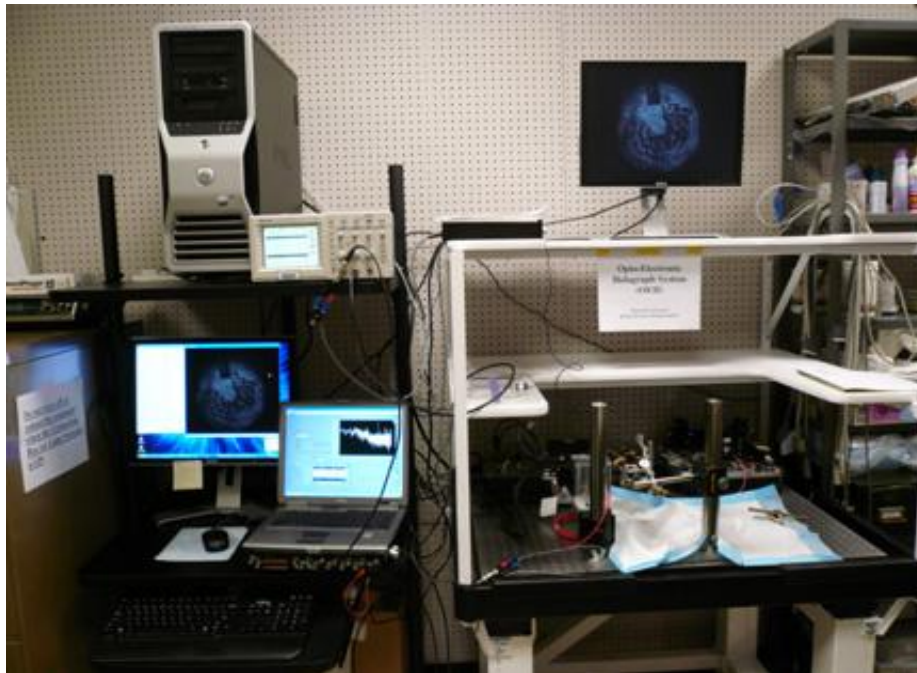


Fig. 15. Laboratory environment of previous generation.

Note the IP software and hardware system located on the left of the image. The LDS and Optical Head are both located on the optical table at the right of the photo. A sample must be clamped to the table where the white cloth is located.

## 5. Objective

The ultimate goal of the OEHO project is to install the OEHO in clinics around the country, providing a standard tool for the measurement and diagnosis of middle ear conditions. The medical doctors who have used the system in the laboratory environment from Fig. 14 have noted a number of improvements which must be addressed prior to this clinical deployment. These improvements are: increased thermomechanical stability; miniaturization; an easier and more intuitive focusing and magnification system; and increased ergonomics.

The increased thermomechanical stability requirement stems from a tendency for the system to drift out of a static reference point in the time it takes to take a thorough data set across all phases of the frequencies of interest.

Miniaturization refers to the size of the optical head. The previous generation is too large to be comfortably handheld and manipulated to interface with a subject.

An easier and more intuitive focusing and magnification system was requested by the physicians. Currently, the doctors often focus on the membrane by moving the subject, rather than using the translator installed in the otoscope head. This is a result of the location of the focusing system, which makes it unintuitive and difficult.

Increased ergonomics refers primarily to the shape of the device. Clinicians and doctors are comfortable with existing otoscope devices, an example of which is shown in Fig. 16. Recognizing that the system will be better received by, and faster incorporated into, the medical community if it resembles and behaves like the current standard provides inspiration for an overall design form.



Fig. 16. Existing otoscope form, used to qualitatively diagnose hearing<sup>26</sup>.

As these improvements are focused around the device's physical interaction with the physician, it is proposed that the improvements be addressed by a redesign of the component which interacts with the physician, the optical head. It was decided that the laser delivery system and image processing subsystem remain unchanged as the current system provides the functionality required (full-field of view, nanometer scale, video rate measurements) via phase-shifted laser interferometry.

Therefore, the objective of this MQP is to address the improvements noted above via a redesign of the otoscope head, while maintaining its function and incorporation with the previous generation laser delivery and image processing subsystems.

## 6. Computer Modeling

The previous generation's optical head was optimized for size and shape given the optical configuration, meaning that in order to address the size and ergonomic improvements required it was necessary to synthesize a new optical configuration. This resulted in a ground-up approach for the design of the otoscope head, where first the required functionality (illumination, imaging, recombination of beams, and interferogram recording) was assured via the optical design, and subsequently the configuration's miniaturization and ergonomic improvement potential were evaluated. Fig. 17 shows a flowchart of the design process proposed.

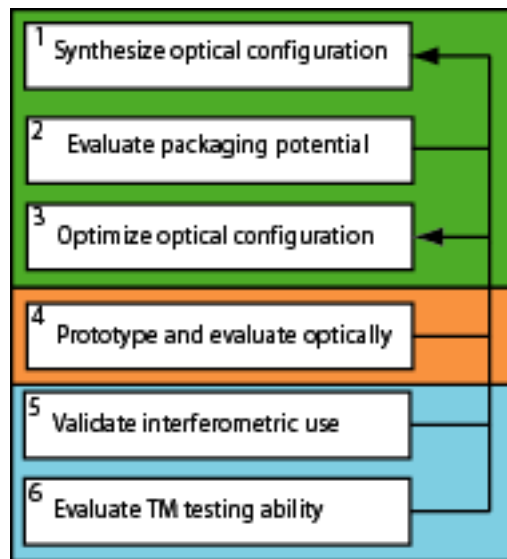


Fig. 17. Flowchart of design process used.

Steps 1-3 are the tasks supported directly with ray tracing CAD software. Step 4 represents the physical characterization of the system, where it can be verified that the configuration meets the design requirements in terms of optical performance. Steps 5 and 6 involve experimentation, and subsequent comparison with the analysis and computational investigations.

## 6.1. Ray Tracing Principles

In order to develop and analyze a new optical system for the otoscope head we explored a computational technique known as ray tracing. Ray tracing is an optical analysis technique where light is treated as a finite number of discrete rays which propagate through space. When a ray encounters an optical component its location and direction are changed via a ray-transfer matrix (RTM)<sup>27</sup>:

$$\begin{bmatrix} A & B \\ C & D \end{bmatrix} \begin{bmatrix} y_1 \\ V_1 \end{bmatrix} = \begin{bmatrix} y_2 \\ V_2 \end{bmatrix} \quad (6.1)$$

This matrix describes the effect of the optical component (characterized by A, B, C, and D) on the input ray ( $y_1$  and  $V_1$ ), the result of which is the output ray position and direction ( $y_2$  and  $V_2$ ). This matrix is capable of describing a combination of translation, refraction, or a combination of translation and refraction. To illustrate the principle, a translation and refraction matrix will be derived below:

The basic translation matrix is derived by first considering the geometric solution of a ray passing through two reference planes,  $RP_1$  and  $RP_2$ .

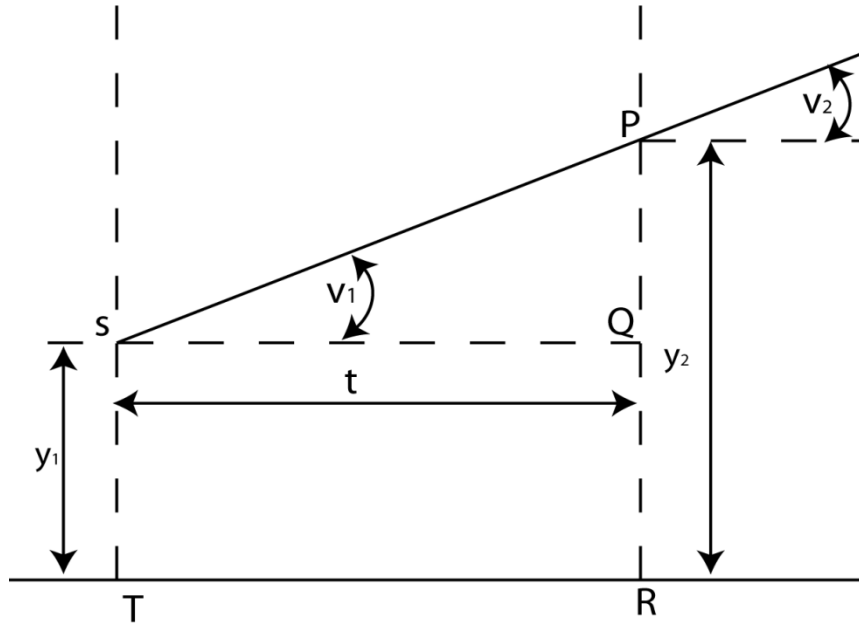


Fig. 18. Geometry of ray translation between two reference surfaces<sup>28</sup>.

Geometrically;

$$y_2 = RQ + QP \quad (6.2)$$

$$= TS + t * \tan(v_1) \quad (6.3)$$

and by a paraxial approximation of rays;

$$= y_1 + t * v_1 \quad (6.4)$$

Likewise, considering the geometry;

$$v_2 = v_1 \quad (6.5)$$

Combining these into matrix form provides a simple translation matrix;

$$\mathcal{S} = \begin{bmatrix} 1 & T \\ 0 & 1 \end{bmatrix} = \begin{bmatrix} A & B \\ C & D \end{bmatrix}, \quad (6.6)$$

Where  $T$  is the reduced thickness of the lens;

$$T = \frac{t}{n}, \quad (6.7)$$

and the directions  $V_1$  and  $V_2$  correspond to the angles  $v_1$  and  $v_2$  via;

$$V_i = n * v_i, \quad (6.8)$$

The other case to consider is refraction, which takes place at optical surfaces. A refraction matrix ( $\mathbf{R}$ ) will be developed using the variables shown:

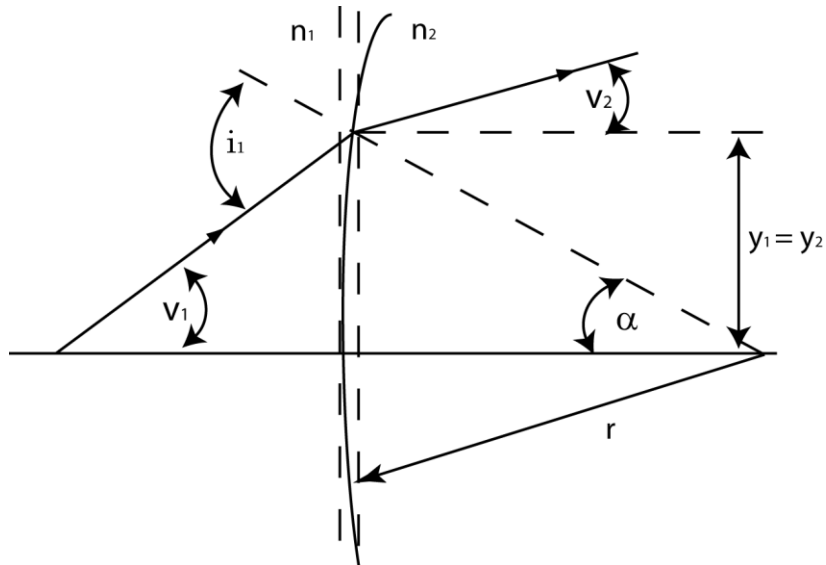


Fig. 19. Geometry of refraction at a curved surface<sup>3</sup>.

To begin, by Snell's law and the paraxial assumption;

$$n_1 * i_1 = n_2 * i_2 \quad (6.9)$$

Substituting in for angles  $i_1$  and  $i_2$  provides;

$$n_1 * (v_1 + \frac{y_1}{r}) = n_2 * (v_2 + \frac{y_2}{r}). \quad (6.10)$$

Or, in matrix form (with the replacements for V and T as noted in the translation matrix derivation);

$$\mathcal{R} = \begin{bmatrix} 1 & 0 \\ \frac{-(n_2-n_1)}{r} & 1 \end{bmatrix} = \begin{bmatrix} A & B \\ C & D \end{bmatrix}. \quad (6.11)$$

## ***6.2. Ray Tracing Computational Model***

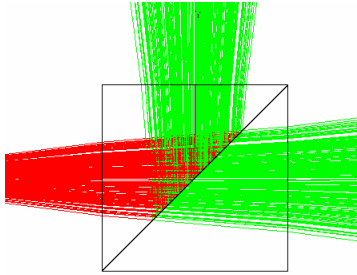
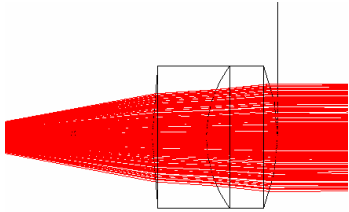
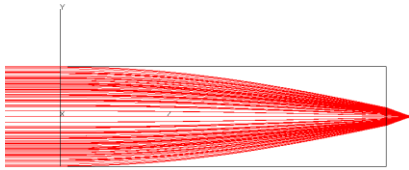
The RTM method above requires a matrix computation for each ray at each optical interface. Adding complexity, each optical surface can result in six possible actions, or a combination thereof. These are: refraction, reflection, absorption, forward scatter, and backward scatter. If a combination of these actions takes place at an optical surface, a single ray is split into multiple rays, which are then propagated to more optical surfaces which can result in more ray splitting and more ray matrix computations. Considering that a raytrace which correctly approximates a physical system can require hundreds of thousands of starting rays; not to mention the exponential increase due to the splitting of rays at optical surfaces; it is natural and necessary to extend the RTM method to a computational system for rapid calculation of ray paths.

Lambda Research's *TracePro*, an existing ray tracing CAD suite, was selected to perform the required ray tracing for optimization and design iteration of the otoscope head. The system performs a Monte-Carlo method of probabilistic ray tracing to determine the ray throughput of a system in three dimensions. ACIS CAD geometry is used to create the volumes and surfaces of an optical system, and the additional optical characteristics of a volume or surface (such as refraction and absorption coefficients; and refractive indices) are input and maintained by the *TracePro* suite.

The system was used to investigate a series of optical components and possible layouts. Considerations of packaging of the system were paramount, as a small size and otoscope like appearance were the primary goals of this generation of otoscope head.

The optical elements used in the ray tracing system are illustrated below with a short description of each element. For further discussion of the benefits of each optical component please refer to the Optical Head Configuration section of this report. For an in depth tutorial of the construction of the ray tracing model see Appendix B.

Table 3. Illustrative component ray traces and construction notes.

Component and Illustrative Screenshot	Notes
<b>Beam Combiners/Splitters</b> 	<p>50/50 beam combiner/splitter cube            Constructed from two separate bodies            3 layer AR coating applied to external surfaces            Beamsplitter properties applied to angled, interior surface.            Validated via equal intensities from each output beam.</p>
<b>Achromatic Imaging Lenses</b> 	<p>Imaging lens achromats where built from their specified geometries.            Two separate material properties define the different indices of refraction of the crown and flint.            Validated by verifying focal points with specifications.</p>
<b>GRIN Imaging Lens (ILW)</b> 	<p>GRIN lens built from given geometry.            SELFOC material used to define refractive index coefficients.            Validated by predicted ray trajectory behavior and focal point.</p>
<b>GRIN Rod Lenses (SRL)</b> 	<p>GRIN lens built from specified length and diameter            SELFOC material used to define refractive index coefficients.            Validated via faithful recreation of pitch number given in specifications.</p>

In addition to the validations noted in the table, each component; and the system as a whole; was validated by monitoring the throughput of a Gaussian distribution of light intensity. Laser light is inherently Gaussian in distribution, and RTM analysis has the ability to faithfully describe the effect of each optical component on a Gaussian distribution. In order to validate that the components were modeled correctly, the distribution throughput of each component was investigated.

The distribution behavior throughout the entire system is shown in Fig. 20. Note the faithful reproduction of the Gaussian intensity. Line profiles are provided through the center of the input and output intensities for comparison.

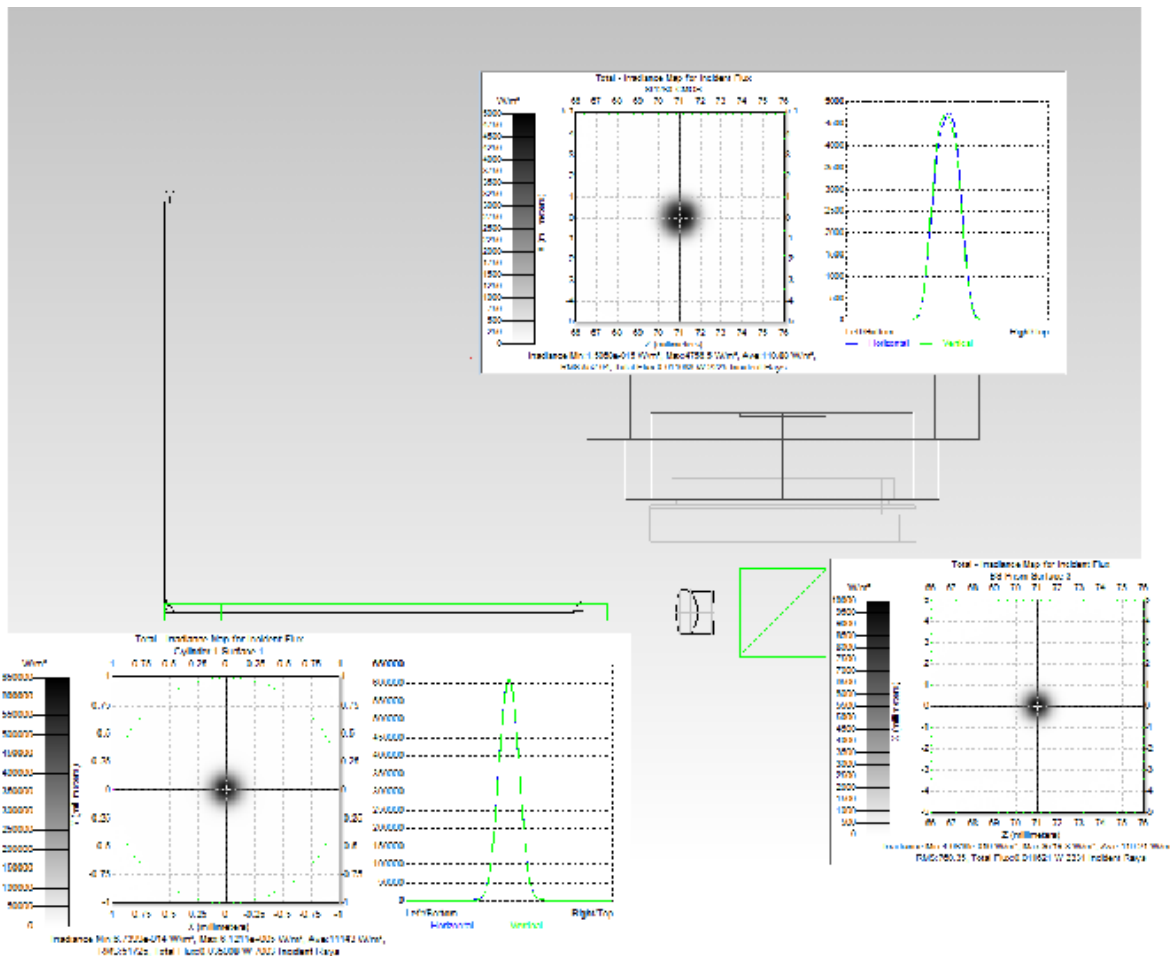


Fig. 20. Gaussian distribution through system; showing input, post imaging lens, and output on CMOS chip.

## 7. Optical Head Configuration

The configuration of the optical head developed is shown in Fig. 21. It consists of 6 components: An object beam (OB), reference beam (RB), Gradient Index (GRIN) rod lens (GRIN), Imaging Lens (IL), beam combiner (BC), and CMOS digital camera (CAM).

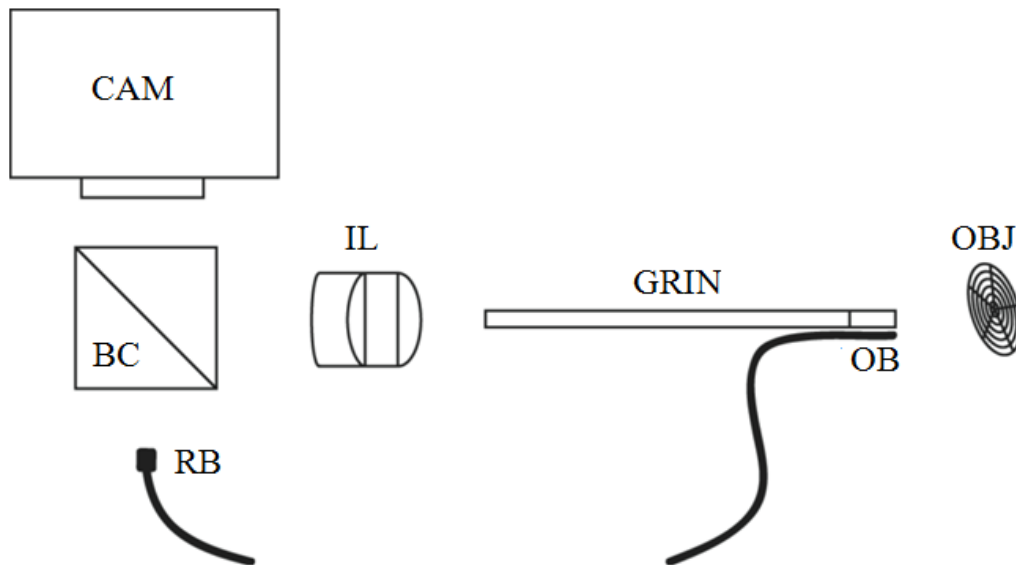


Fig. 21. Schematic of the optical head showing object beam and reference beam optical fibers (OB and RB, respectively), gradient-index rod lens (GRIN), imaging lens achromat (IL), beam combiner cube (BC) and CMOS camera (CAM).

The object and reference beams are incorporated via single-mode optical fibers from the laser delivery system. The object beam is attached via a bare fiber secured in the otoscope packaging. The distance required between the OB fiber output and the object, given an object beam fiber with a numerical aperture of 0.13<sup>29</sup> and a desired coverage of 12mm x 12mm (increased by 20% to account for the Gaussian distribution of intensity), is:

$$\frac{12mm * 1.2}{\tan(2 * 0.13)} = 54.1mm. \quad (7.1)$$

Likewise, the reference beam is required to provide full illumination across the CMOS chip, which has a size 6.9 mm x 8.6 mm<sup>30</sup>. Again, the desired area is increased 20% to account for the uneven distribution of light from the fiber.

$$\frac{8.6mm * 1.2}{\tan(2 * 0.13)} = 3.88mm \quad (7.2)$$

A small diameter (2mm) gradient index lens was incorporated into the system for several reasons. First, the small diameter makes it appropriate for packaging inside an otoscope speculum. Gradient index lenses are commonly used in endoscopy in order to focus an image in a small cavity<sup>31</sup>. Second, the gradient index lens has a numerical aperture (NA) of 0.100<sup>32</sup>. The small NA should provide an increased depth of field, as NA and depth of field are inversely proportional<sup>33</sup>.

The pitch of a gradient index lens refers to the number of cycles of the sinusoidal variation of light throughout its length. Fig. 22 shows a variety of pitch possibilities when selecting a GRIN rod lens.

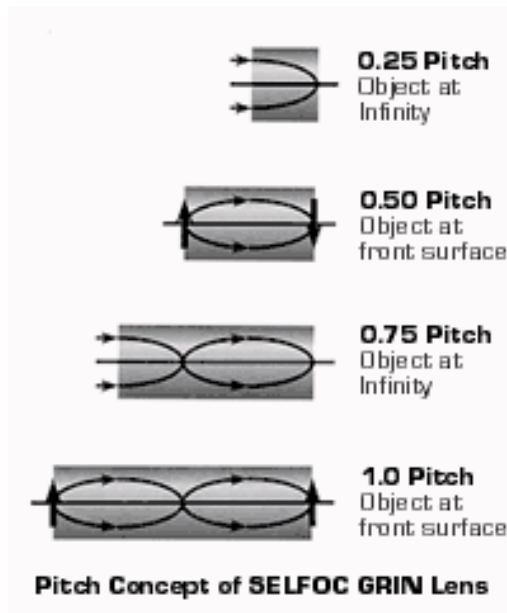


Fig. 22. GRIN lens Pitch concept illustration<sup>34</sup>.

The lens selected has a pitch of 0.50, resulting in the image on the front surface inverted on the back surface.

The imaging lens (IL) is used to collimate the light from the GRIN back surface. The lens selected is an achromat of diameter 5mm. An achromat was selected as to reduce any potential spherical or chromatic aberrations from the imaging lens. Transverse aberrations are also reduced, and off axis rays are more tightly focused when compared to traditional lens singlets<sup>35</sup>. See Fig. 23.

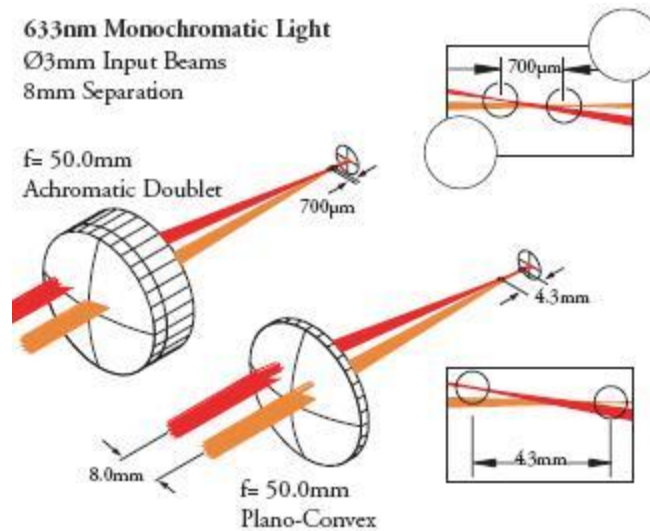


Fig. 23. Off-axis performance of achromatic doublet versus plano-convex lens<sup>36</sup>.

The focal length of the lens is 7.9mm, which is the distance the lens should be placed from the GRIN lens back surface.

To recombine the two beams, a 50/50 beam splitter cube is used (BC).

Two cameras were examined for use with the system, the PixelLink PL-A741 and the selected camera, a Silicon Imaging SI-1280. The SI-1280 is 1024x1280 pixel, 12bit CMOS type camera. The pixel size is 6.7microns square. The camera selected for its small size, full-frame shutter, and active spectral response in the near-infrared range (as a near infrared laser is suggested for use). It is important to select a camera which captures the maximum amount of light reflected off the tympanic membrane. Fig. 24 shows the response curve of this camera over a variety of wavelengths.

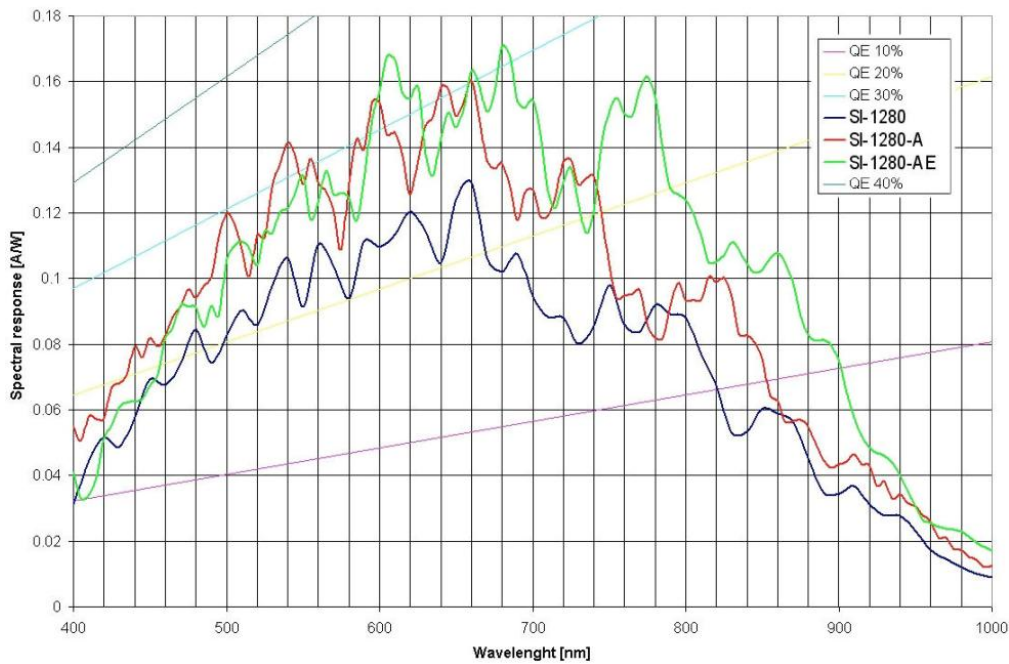


Fig. 24. Spectral response of SI-1280 Camera<sup>37</sup>.

Complete properties of all the optical components selected, including manufacturer's part numbers, can be found in Appendix D.

## 8. Realization

### 8.1. Building the Prototype

With the otoscope head design optimized theoretically the device was prototyped. Miniaturization was the primary focus when manufacturing the prototype, while also incorporating the design considerations from the computer model. The ray tracing analysis determined that stray light reaching the camera needed to be minimized; therefore all of the components were housed in enclosures. Fig. 25 shows the otoscope head that was manufactured.

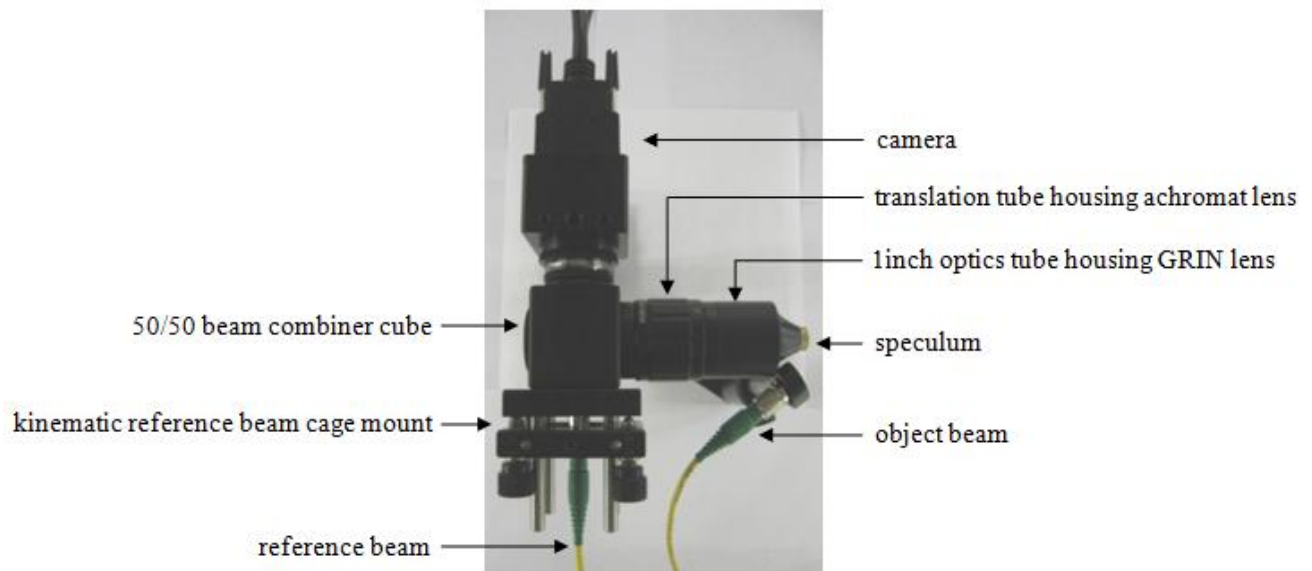


Fig. 25. Miniaturized Otoscope Head.

The nominal dimensions of the otoscope head were significantly reduced when compared to the previous design. The reduced size of is attributed in large part to the folding of the longest optical path, as the optical path from the object being imaged to the camera is bent at 90 degrees by means of a 50/50 beam combiner. Also, the miniaturized design has much fewer adjustable mounts in comparison to the previous generation, which further reduces the overall size. It should be noted

that the rotating translation mount used in the miniaturized design is smaller than the linear translation mounts used in the previous design. The combination of these features led to a much more compact design.

A comparison of the nominal dimensions of the miniaturized otoscope head and the previous generation otoscope head is shown in Fig. 26.

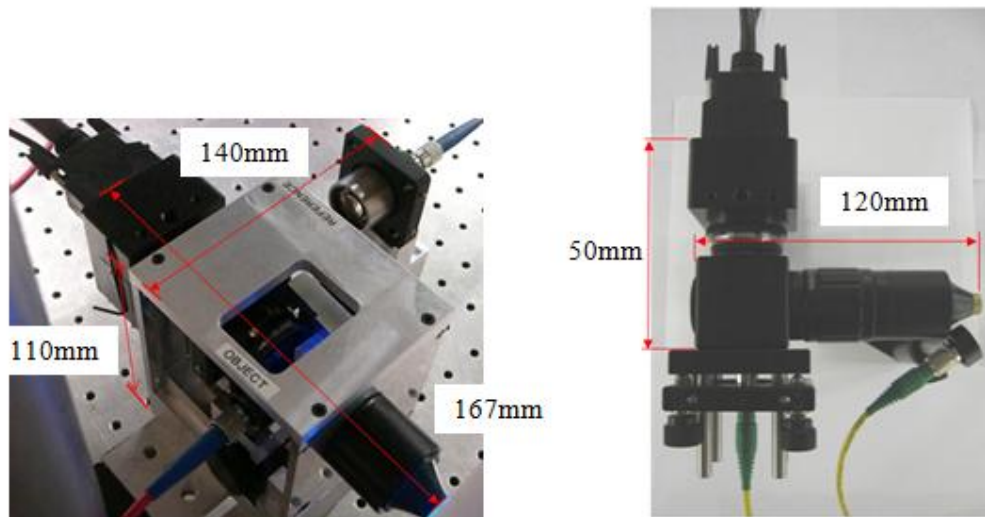


Fig. 26. Previous Generation Otoscope Head<sup>18</sup> (Left); Miniaturized Otoscope Head (Right).

The height of the miniaturized otoscope, the dimension into the page in Fig. 26, is only 50mm compared to the previous generation's 110mm height. This height is limited by the height of the camera, and could be feasibly reduced to approximately 25mm if the printed circuit board version of the Silicon Imaging 1280i camera was used. The significant reduction in otoscope head size resulted in a much more compact, otoscope like design.

## ***8.2. Characterization of Optical Performance***

Not only was the new otoscope developed intended to be smaller than the previous generation, but the optical performance required improvement in specific areas. It was necessary to characterize the optical performance of the miniaturized otoscope head in order to make a quantitative comparison of it to the prior generation. Unfortunately, a standardized procedure for characterizing the field of view, magnification, depth of field, resolution and image aberration was not developed and implemented in the characterization of the prior generation otoscope head. Therefore, such a procedure with the appropriate targets, image analysis algorithms, and documented parameters was developed for the characterization of the miniaturized otoscope head.

### **8.2.1. Field of View**

The first characteristic that was determined was the field of view. The background biology determined the required field of view needed to be 10mm. To determine the distance the object needed to be away from the optical system to allow a 10mm by 10mm region of it be imaged, a target comprised of vertical white and black line pairs at a frequency of one line pair per millimeter was used. A field of view of 10mm was achieved when ten line pairs perfectly fit within the field of view. At a working distance of 13mm the ten line pairs fit within the field of view. The working distance for the previous generation otoscope head to get an equivalent field of view was approximately 90mm. The shorter working distance of the miniaturized otoscope makes measurement of in vivo tympanic membrane much more feasible, as the device can be more easily packaged in a design similar to existing otoscopes. Fig. 27 compares the an image of the target used to determine the field of view at the working distance to a image of the same target scaled to the actual size.

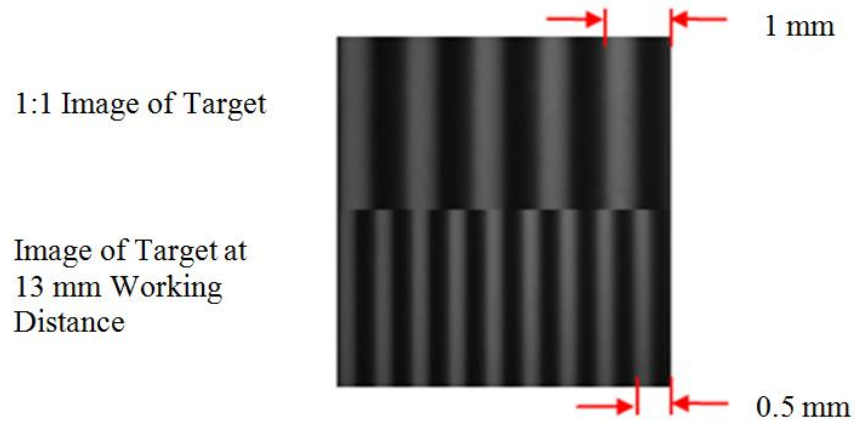


Fig. 27. Field of View And Magnification Image.

### 8.2.2. Magnification

The magnification shown in Fig. 27 is approximately 0.5, this can be calculated from the geometry of the system. The CMOS chip used has dimensions of 1280 pixels wide by 1024 pixels tall. Each pixel is a square with edge length of  $6.7\mu\text{m}$ . The size of the region of interest on the camera being used is 800 pixels by 800 pixels. Because at a 13mm working distance 10mm fit within the field of view the magnification can be calculated by finding the ratio of the length of 800 pixels on the CMOS chip to the actual length of the region being imaged:

$$M = \frac{\left(\frac{800 \text{ pixels}}{1280 \text{ pixels}}\right) \cdot \left(1280 \text{ pixels} \cdot \frac{6.7 \times 10^{-3} \text{ mm}}{1 \text{ pixel}}\right)}{10 \text{ mm}} = 0.536 \quad (8.1)$$

This means that a 10mm by 10mm region of the object is being imaged on a 5.36mm by 5.36mm region of the CMOS chip.

### 8.2.3. Resolution

The resolution was determined using a 1951 United States Air Force resolution target. The target is comprised of many groups of white and black line pairs at various frequencies. The better the resolution an imaging system has the greater the line pair frequency the system is able to resolve. A systems ability to resolve a line pair is determined by how well the system can maintain contrast between the white and black regions of the line pair. The determination of how faithfully a system images the contrast is accomplished by implementing image analysis algorithms in computer software capable of pixel-to-pixel contrast comparisons. Because a pixel-to-pixel intensity comparison is used to determine the contrast, uniform object illumination is necessary.

Uniform illumination across an entire target allows for valid comparison of the various line pair frequencies. In the case of the resolution target used, even illumination can be achieved by illuminating the target from behind. This was accomplished by using either a fiber optic illuminator with a glass diffuser or a compact fluorescent light bulb to disperse the light evenly over the back of the glass target slide. Fig. 28 is an image taken with the miniaturized otoscope head of the resolution target.

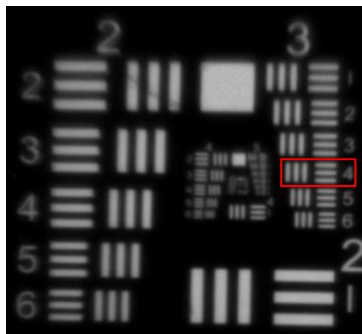


Fig. 28. 1951 USAF Resolution Target.

By performing a contrast trace across all of the line pair elements on the target, and noting the maximum and minimum values of the gray scale variation between the white and black lines the contrast was determined. At a 13mm working distance the miniaturized otoscope head is able to resolve element 4 of group 3, shown encompassed by a red rectangle in Fig. 28. This correlates to a line pair per millimeter resolution of  $11.30^{38}$  at 59% contrast. A more in depth description of the algorithm used can be found in Appendix C.

#### **8.2.4. Depth of Field**

Doctors using the previous generation otoscope requested a larger depth of field to allow for easier focusing and measurement acquisition. The depth of field of the miniaturized otoscope was characterized experimentally with a depth of field 45 degree wedge target. The target has horizontal lines spaced at known intervals that correspond to a distance parallel to the optical axis. A contrast trace can be performed on the image of the target. The point where the contrast drops below a certain percentage of the maximum contrast is said to be beyond the depth of field. Further description of the algorithm used can be found in Appendix C. The test setup used to characterize the depth of field is shown in Fig. 29.

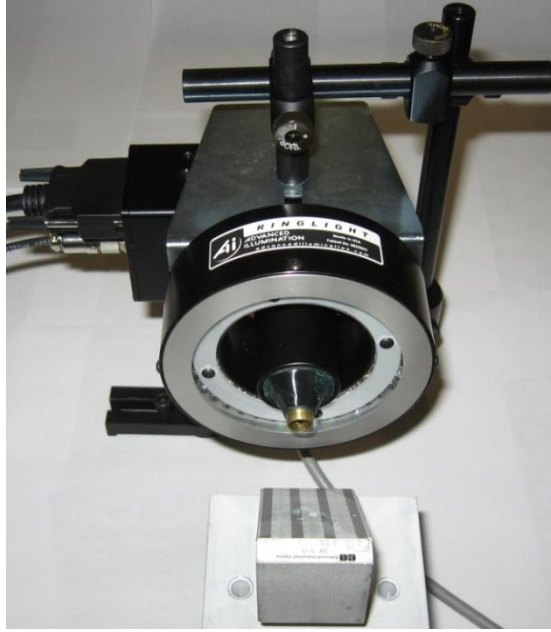


Fig. 29. Depth of Field Test.

The optical head is shown inserted through a bright field/dark field ring illuminator. The purpose of the ring illuminator is to provide an even light distribution on targets that require front illumination. The target is positioned at approximately the 13mm away from the GRIN lens. The depth of field target has multiple groups of line pair frequencies; to perform the characterization of the miniaturized otoscope head the five line pair per millimeter group was used. Fig. 30 is a graph generated from the contrast trace of the imaged used to characterize the depth of field.

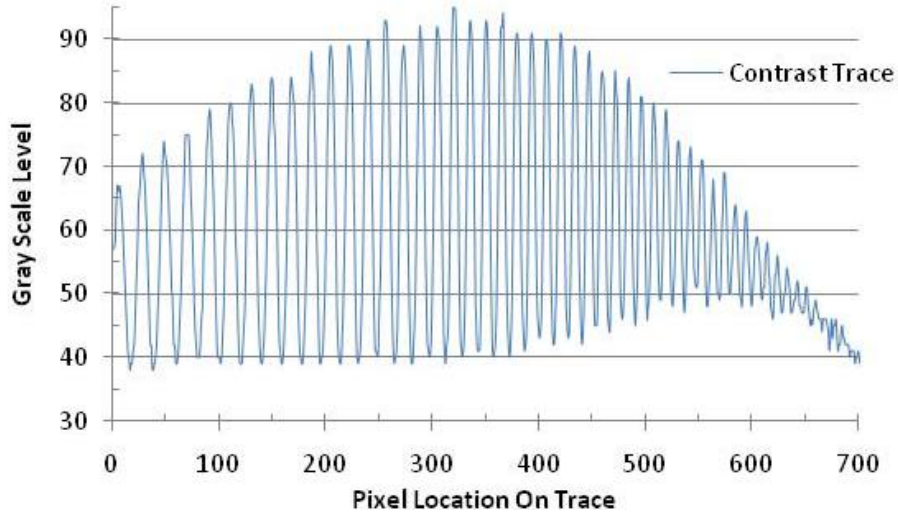


Fig. 30. Depth of Field Contrast Trace Graph.

Each oscillation on the graph corresponds to a white and black line pair. The minimum contrast level required to be considered ‘in focus’ for the depth of field test was 60% of the maximum contrast oscillation in the image. The maximum contrast in the image is seen at approximately pixel 340, where the peak gray scale value is 95 and the minimum gray scale value is approximately 40. The difference of these two values gives the maximum gray scale contrast in the trace; therefore 60% of 55 is the minimum contrast level to be considered in focus. Thirty-one oscillations have a contrast of 33 or greater. Because every 5 oscillations correspond to 1 mm, the depth of field can be calculated as;

$$DoF = \frac{31lp}{5 \frac{lp}{mm}} = 6.2mm \quad (8.2)$$

A depth of field of 6.2mm is attained with the miniaturized optical head when performing a contrast trace across the 5 line pair per millimeter group at 60% contrast of the 45 degree depth of field wedge target. The previous generation claimed a depth of field of 5mm<sup>39</sup>. To make a quantitative comparison to the new optical head the same methodology described in this section

should be used to characterize the depth of field of the previous generation otoscope. It was noted, qualitatively, that the miniaturized optical head had a noticeably improved depth of field.

### 8.2.5. Image Aberration

All lenses introduce optical distortions. Depending on a number of parameters the degree to which the lenses distort the image varies. The optical distortions the miniaturized optical head introduced were characterized to better understand the degree to which distortions affect image quality. To characterize the image aberration a fixed frequency grid distortion target was used. This target is comprised of a grid of evenly spaced black dots on a glass substrate. The entire grid has dimensions of 25mm by 25mm, and dots are located every 0.25mm. The distortion can be compensated for by characterizing how the imaged distorted dot positions are shifted from their original undistorted positions.

The grid target was placed at the working distance of 13mm, and evenly back illuminated. The image acquired is shown in Fig. 31.

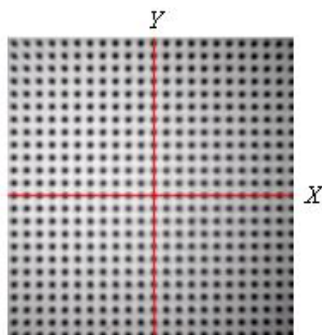


Fig. 31. Grid Distortion Target.

Dots lying on the red perpendicular axes labeled  $X$  and  $Y$  are distorted along the line they lie on. This one dimensional distortion is the same along both axes. In order to determine the amount of distortion on said axes an algorithm was developed that utilized centroid analysis techniques.

The algorithm developed to determine the distortion function first labels each dot as a separate region based on contrast. The centroid of each region is determined and a matrix of the location of the distorted centroids is created. By comparing the distorted centroid locations to the undistorted centroid locations the deviation of each centroid is calculated. Fig. 32 shows the plot generated with the algorithm of the distorted centroid locations versus original centroid locations and the function fit to the data. Function fitting is built in to the algorithm developed; therefore iteratively determining the appropriate function is fast and seamless. A more in depth description of the algorithm used, as well as the code, can be found in Appendix C.

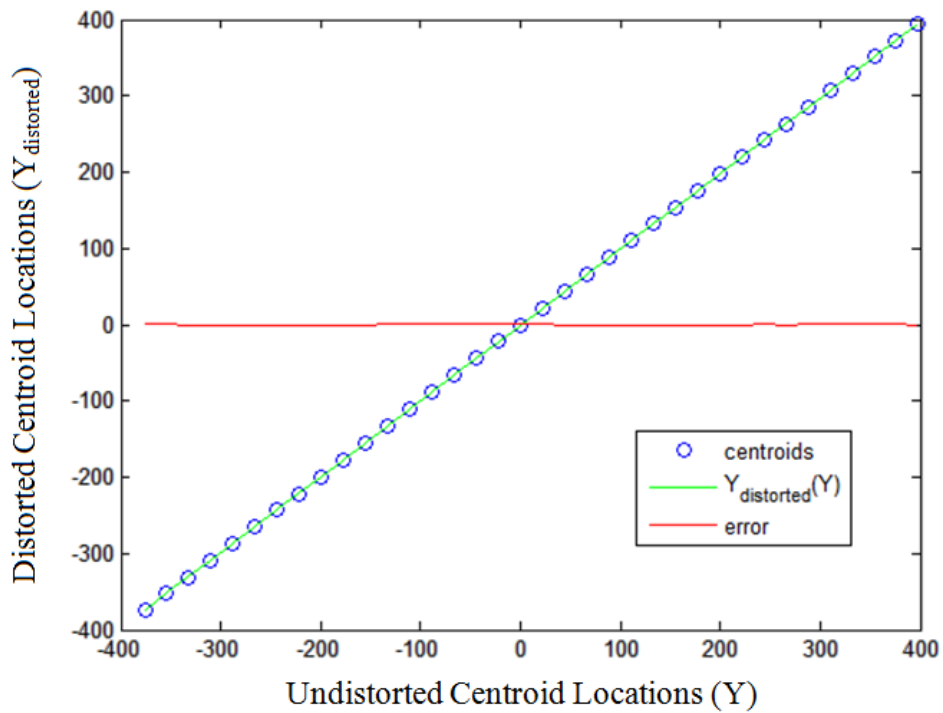


Fig. 32. Distortion Function.

The data appears to be linear, which suggests that optics introduce very little distortions to an image. Despite the appearance of linearity, the better fit for the data is a third-order polynomial. This was determined by plotting the error and varying the order of the polynomial fit until the error was approximately zero. The function fit to the data shown in Fig. 32 is given by:

$$Y_{distorted}(Y) = -4.038 \times 10^{-8} \cdot Y^3 - 3.729 \times 10^{-6} \cdot Y^2 + 0.995 \cdot Y - 0.327 \quad (8.3)$$

where  $Y_{distorted}$ , the location of the distorted centroids, is a function of the original centroid location,  $Y$ . The function describing the distortion could now be implemented to calibrate the image processing software; and the optical distortion the lenses introduce could be removed.

## 9. Validation

The performance of the optical head was validated through the comparison of analytical and computational solutions of the vibration modes of a cantilever beam to the experimental results. A cantilever beam was selected as the geometry to evaluate the miniaturized otoscope with because of its well established analytical and computational models. The copper cantilever modeled and constructed was a 0.002 inches thick, 0.421 inches long, and 0.176 inches wide. Such dimensions were chosen via analytical work to ensure the beams first three modes of vibration were within the audible range for humans, while still fitting approximately in a ten millimeter field of view.

### 9.1. Analytical Validation

This section describes the analytical process carried out to go from the elementary flexural theory to determining the modes of vibration of a cantilever beam<sup>40</sup>. Such analysis is necessary to understand the phenomena of how the mode shapes of a beam and the frequencies which they occur at are developed.

It is assumed that the beam being analyzed has a constant cross section and material properties. A diagram of the theoretical beam is shown in Fig. 33.

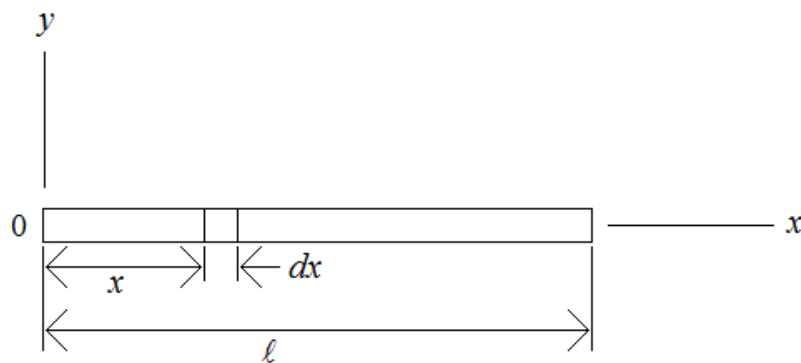


Fig. 33. Prismatic Beam.

The following derivation is based on the fourth-order ordinary differential equation for the free transverse vibration of a beam based on,

$$E \cdot I \cdot \left( \frac{\partial^4}{\partial x^4} y \right) \cdot dx = -\rho \cdot A \cdot dx \cdot \frac{\partial^2}{\partial x^2} y \quad (9.1)$$

where;

$E$  is the modulus of elasticity of the material,

$I$  is the area moment of inertia,

$\rho$  is the density of the material,

$A$  is the cross sectional area of the beam.

If we define  $a = \sqrt{\frac{E \cdot I}{\rho \cdot A}}$  and substitute it into Eq. 9.1. The equation for the free transverse vibration

of a beam can be written as;

$$\left( \frac{\partial^4}{\partial x^4} y \right) = -\frac{1}{a^2} \frac{\partial^2}{\partial x^2} y. \quad (9.2)$$

The deflection at any location on a beam varies harmonically with time as the beam vibrates transversely in a natural mode. The deflection is described by;

$$y = X[A \cdot \cos(p \cdot t) + B \cdot \sin(p \cdot t)] \quad (9.3)$$

If we substitute Eq. 9.3 into Eq. 9.2, and take the partial derivatives this yields:

$$\left[ \frac{\partial^4}{\partial x^4} X \right] \cdot [A \cdot \cos(p \cdot t) + B \cdot \sin(p \cdot t)] = \frac{p^2}{a^2} \cdot X [A \cdot \cos(p \cdot t) + B \cdot \sin(p \cdot t)] \quad (9.4)$$

Simplifying this expression yields;

$$\frac{d^4}{dx^4} X - \frac{p^2}{a^2} \cdot X = 0 \quad (9.5)$$

To make it easier to solve the differential equation we will define  $k^4 = \frac{p^2}{a^2}$ . Now the fourth-order differential ordinary differential equation has the form;

$$\frac{d^4}{dx^4} X - k^4 \cdot X = 0 \quad (9.6)$$

Next the form of the general solution needs to be determined. To satisfy Eq. 9.6 assume  $X = e^{nx}$ .

Substituting the assumed value of X into Eq. 9.6 and simplifying yields:

$$e^{nx} \cdot (n^4 - k^4) = 0 \quad (9.7)$$

To satisfy Eq. 9.7 n can be equal to:  $k$ ,  $-k$ ,  $i \cdot k$ , and  $-i \cdot k$ . So the general solution of the beam in free transverse vibration is given by;

$$X = C \cdot e^{kx} + D \cdot e^{-kx} + E \cdot e^{ikx} + F \cdot e^{-ikx}, \quad (9.8)$$

which can also be written as:

$$X = C_1 (\cos(kx) + \cosh(kx)) + C_2 (\cos(kx) - \cosh(kx)) + C_3 (\sin(kx) + \sinh(kx)) + C_4 (\sin(kx) - \sinh(kx)) \quad (9.9)$$

Equation 9.9 describes any beam in transverse vibration. To determine the constants  $C_1$ ,  $C_2$ ,  $C_3$ , and  $C_4$  for the particular case of the cantilever beam boundary conditions must be applied.  $C_1$  can be solved for by applying the deflection boundary condition at the fixed end of the beam;

$$X|_{x=0} = 0 = C_1(2) + C_2(0) + C_3(0) + C_4(0),$$

Therefore;

$$C_1 = 0 \tag{9.10}$$

$C_3$  can be solved for by applying the slope boundary condition at the fixed end of the beam:

$$\left. \frac{d}{dx} X \right|_{x=0} = 0 = C_2(0) + C_3(2 \cdot k) + C_4(0)$$

Therefore;

$$C_3 = 0 \tag{9.11}$$

$C_2$  and  $C_4$  cannot be solved for directly, but by applying the final two boundary conditions the ratio of  $C_2$  to  $C_4$  is able to be determined. One ratio is found by applying the moment boundary condition at the free end of the beam;

$$\left. \frac{d^2}{dx^2} X \right|_{x=\ell} = 0 = C_2 \cdot k^2 (\cos(k\ell) + \cosh(k\ell)) + C_4 \cdot k^2 (\sin(k\ell) + \sinh(k\ell))$$

Therefore;

$$\frac{C_2}{C_4} = \frac{-\sin(k\ell) - \sinh(k\ell)}{\cos(k\ell) + \cosh(k\ell)} \quad (9.12)$$

Applying the shear force boundary condition yields the second ratio;

$$\left. \frac{d^3}{dx^3} X \right|_{x=\ell} = 0 = C_2 \cdot k^3 (\sin(k\ell) - \sinh(k\ell)) - C_4 \cdot k^3 (\cos(k\ell) + \cosh(k\ell))$$

Therefore;

$$\frac{C_2}{C_4} = \frac{\cos(k\ell) + \cosh(k\ell)}{\sin(k\ell) - \sinh(k\ell)} \quad (9.13)$$

Setting Eq. 9.12 equal to Eq. 9.13 and simplifying yields;

$$\left[ -\sin(k\ell)^2 - \cos(k\ell)^2 \right] + \left[ -\sinh(k\ell)^2 - \cosh(k\ell)^2 \right] = 2 \cdot \cos(k\ell) \cdot \cosh(k\ell)$$

To simplify further we apply the identities;  $\sin(k\ell)^2 + \cos(k\ell)^2 = 1$ , and  $\cosh(k\ell)^2 - \sinh(k\ell)^2 = 1$ .

This yields the frequency equation;

$$\cos(k\ell) \cdot \cosh(k \cdot \ell) = -1 \quad (9.14)$$

The roots of Eq. 9.14 are used to calculate the fundamental modes of vibration of the cantilever beam.

The equation that described the frequencies that the fundamental modes of vibration occur at is;

$$f = \frac{a}{2 \cdot \pi} \cdot \left( \frac{k \cdot \ell}{\ell} \right)^2, \tag{9.15}$$

Where:

$$a \text{ is defined as } \sqrt{\frac{E \cdot I}{\rho \cdot A}},$$

$k \cdot \ell$  is the corresponding root of Eq. 9.14,

$\ell$  is the length of the beam.

For the copper beam used to validate the otoscope head the first three natural frequencies with the corresponding  $k \cdot \ell$  roots are shown in Table 4.

Table 4. Analytically Determine Natural Frequencies.

	Natural Frequency	$k \cdot \ell$ Root
First Mode	244.3 Hz	1.875
Second Mode	1531.3 Hz	4.694
Third Mode	4287.6 Hz	7.855

## 9.2. Computational Validation

A computational model of the cantilever beam was developed to compliment the analytical results, as well as help verify the experimental results. The computational work was done with the ANSYS 11.0, a finite element analysis program. The model was created as an elastic beam element with a constant cross section and material properties. As with all finite element problems the mesh size and computation method had to be carefully considered.

Because only the first three dynamic transverse modes were of interest the beam was analyzed with the Subspace Method in ANSYS. This computational method determines all of the specified modes for all of the degrees of freedom<sup>41</sup>. This method yields quite accurate results, but at the expense of computation time. The computation time was then optimized by determining the appropriate mesh size.

In this finite element problem the mesh size determined how many discrete elements the beam would be divided into. Computations were done with a number of different differential element mesh sizes until a good balance was reached between computation time and accuracy of results. A beam discretized into one-hundred elements with one end having all of its degrees of freedom limited yielded relatively fast computation times and modal frequencies within one percent of the analytical modal frequencies. Fig. 34 is representation of the computational beam developed.

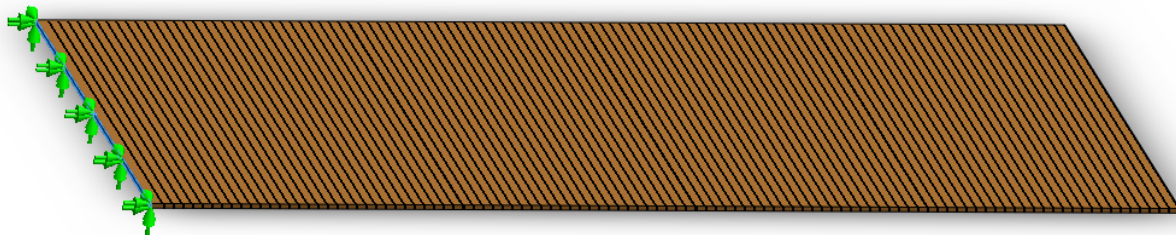
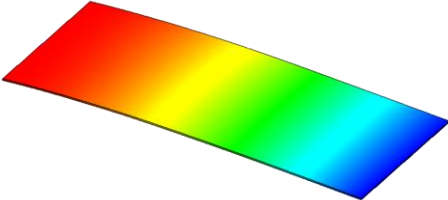
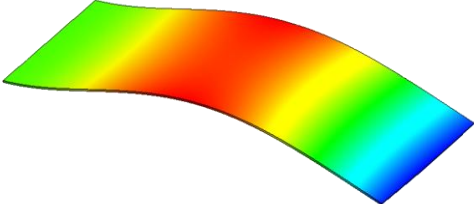
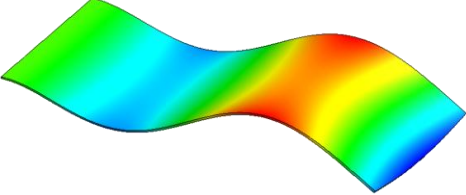


Fig. 34. Finite Element Beam.

The beam is seen here divided into one-hundred discrete elements, each with a length of approximately 107μ-meters. The green arrows on the left of the beam represent the boundary condition that is fully restraining the left face.

The material properties<sup>42</sup> of the beam were defined for a linear elastic isotropic model with a: Young’s Modulus of 103GPa, Poison’s Ratio of 0.34, and density of 8885 kg/m<sup>3</sup>. The computational results from the ANSYS<sup>43</sup> analysis are shown in Table 4.

Table 5. Finite Element Modes of Cantilever.

	Frequency	Three Dimensional Mode Shape
First Mode	244.9 Hz	
Second Mode	1534.7 Hz	
Third Mode	4297.1 Hz	

### ***9.3. Experimental Validation***

The cantilever beam was constructed in order to determine the experimental modes of vibration. The beam was cut from copper shim stock to ensure a uniform thickness of 0.002in and a uniform surface finish. The width of the beam was made to be 0.176in, and the length was left longer than the 0.421in required for the cantilever so it could be clamped. Because diffuse light reflecting off of the object is needed to generate good interferograms, white paint was applied to the surface of the beam to reduce the amount of specular reflections.

#### **9.3.1. Experimental Procedure**

The beam was fixed in a steel clamp so that 0.421in of the beam extended past the clamp. The clamp was then attached to a piezo shaker. The entire assembly was fixed with the beam located within the field of view of the otoscope. Using a white light source the otoscope was focused on the beam. The fixtured cantilever assembly is shown Fig. 35.

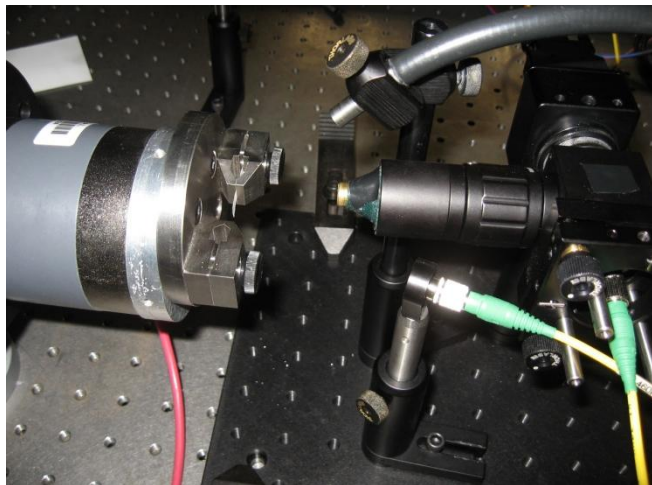


Fig. 35. Cantilever Test Setup.

With the beam both in the field of view and in focus, the laser light for interferometric measurements was setup. Due to the small numerical aperture of the system little light is transmitted from the object to the camera chip. For this reason careful adjustment to the object and reference beams must be carried out.

The first adjustment to the reference beam should be centering it on the recording medium, in this case the camera's complementary metal-oxide semiconductor (CMOS) chip. Centering the reference beam in the region of interest on the CMOS chip is accomplished by mounting the fiber output accurately on the optical axis, so that it illuminates the region of interest evenly. Often this approach is not feasible due to an inability to control tolerances in the system, such as how accurately the lenses are mounted or how square the beam combiner is with the optical paths. Therefore in prototype experimental configurations often the reference beam often must be directed slightly off-center. When this is the case a kinematic fiber mount is required to precisely position the reference beam illumination in the region of interest on the CMOS chip. The prototype system developed uses such a solution.. It should be noted that the likely causes of the image not being perfectly centered on the CMOS chip in the prototype are the tolerances in the achromatic imaging lens's and GRIN lens's mounts.

The object beam is adjusted so that it evenly illuminates the object, while maintaining a minimal angle between the incident object beam light and the axis of the GRIN lens. Because the laser light output from the fiber has a divergent Gaussian intensity distribution it is important to not place the fiber output too close to the object. When the object fiber output is placed far enough away, the object will be illuminated evenly. In order to monitor how evenly the object beam is distributed on the CMOS chip the reference beam should be blocked and the contrast trace tool can be used in Laser View. By tracing across the region of interest one can ensure there is not a significant change

in brightness from one area to another. When the object beam is fixed in its final position, the reference beam can be unblocked so the beam ratio can be set.

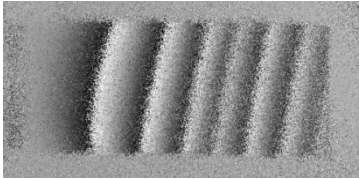
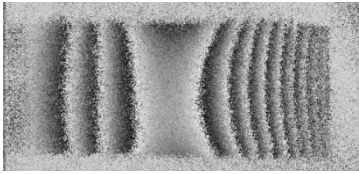
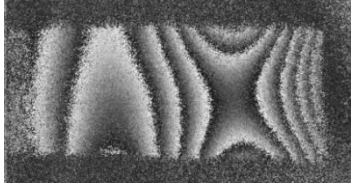
The beam ratio is the ratio of the amount of light from the reference beam to the amount of light from the object beam reaching the CMOS chip. To adjust the beam ratio the amount of light being coupled into the optical fiber is adjusted. Due to low amount of light that can be transmitted through the optical system, the amount of power from object beam is typically maximized; therefore the beam ratio is determined by coupling and de-coupling the reference beam. A beam ratio between one and two is recommended. With the reference and object beams fully setup measurements were taken.

### **9.3.2. Experimental Results**

The piezo shaker was excited via a function generator. The first three modes of vibration were determined by adjusting the excitation frequency at intervals of 100Hz until a mode shape was clear in the time averaged interferograms. When a mode shape was found the frequency and voltage amplitude to the piezo shaker were adjusted to more accurately determine the frequency of that particular mode of vibration. The frequencies that corresponded to the first three modes of vibration were determined, and the optical phase measurements were taken in double exposure mode with stroboscopic illumination.

The frequency generator, controlled via USB from the image processing computer, had the output from channel one connected to the piezo shaker and the output from channel two connected to the AOM driver. A sine wave was input to the piezo shaker, and a pulse wave to the driver. Measurements were made with a beam ratio of 1.8, 10% duty cycle, and camera exposure time of 25ms. The experimental results for the first three modes of vibration are shown in Table 6.

Table 6. Experimental Modal Frequencies obtained with OEHO Functioning in Double-Exposure Stroboscopic Mode.

	Frequency	Interferogram	Piezo Peak-to-peak Voltage
First Mode	238.5 Hz		5 V
Second Mode	1501.5 Hz		7 V
Third Mode	4092.0 Hz		8 V

#### **9.4. Validation Results Comparison**

A comparison of the analytical and computational results with respect to the experimental results is shown in Table 7.

Table 7. Analytical and Computational Percent Error.

	First Mode	Second Mode	Third Mode
Analytical	2.4%	2.0%	4.9%
Computational	2.7%	2.2%	5.0%

The minimal percent error equal to or less than 5% of the analytically and computationally determined frequencies with respect to the experimentally determined frequencies can be attributed to assumptions made in the analysis. Small inconsistencies in parameters used in the analysis such as the material properties, and the geometry of the beam may have introduced the error. Also, it is possible a user error, such fixing the beam imprecisely, may have introduced the error.

## 10. Testing

Testing of the miniaturized otoscope head was performed on 6mm diameter nitrile membrane and on a post mortem chinchilla tympanic membrane.

The nitrile membrane was supplied by the doctors at the Massachusetts Eye and Ear Infirmary to measure because of its resemblance, physically, to a real tympanic membrane in the capacity that it has a small circular shape and is optically semi-transparent. The membrane was imaged with the miniaturized otoscope head while being excited acoustically with a speaker. Fig. 36 shows the test setup used to image the membrane.

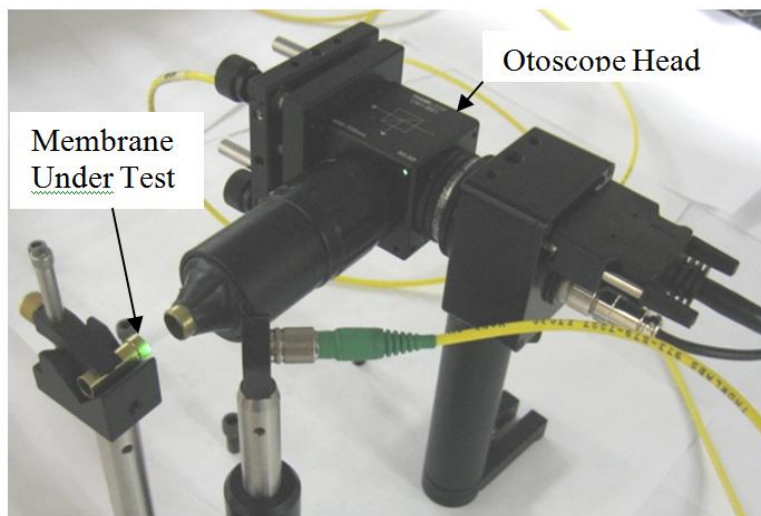


Fig. 36. Nitrile Membrane Test Setup.

The speaker's input frequency and voltage amplitude were set via a function generator, and the optical phase images were acquired. The first mode of vibration of the nitrile membrane was found at 4.228kHz, demonstrating the miniaturized otoscope head's ability to image semi-transparent membranes. A more complex mode of vibration was acquired at 10.66kHz, the optical phase image was unwrapped and plotted, demonstrating the system's ability to acquire three-dimensional

information. The unwrapped optical phase image at 4.228kHz, 10.66kHz and the three-dimensional plot is shown in Fig. 37.

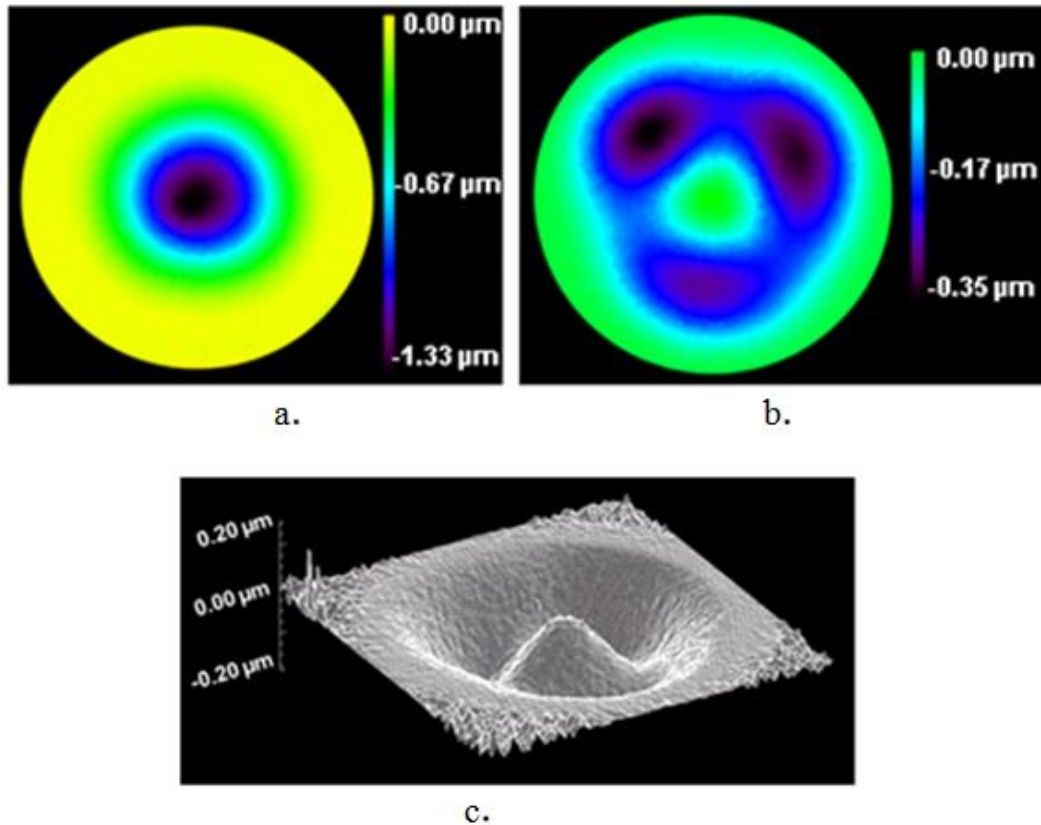


Fig. 37. (a) Nitrile Membrane at 4.228kHz; (b) Nitrile Membrane at 10.66 kHz; (c) 3-D Representation of Nitrile Membrane at 10.66kHz.

A cadaveric chinchilla was brought to the Center for Holographic Studies and Laser  $\mu$ mechaTronics to test how the miniaturized otoscope head measured tympanic membranes. The chinchilla head, with its tympanic membranes exposed, was clamped in a fixture. The tympanic membrane was excited acoustically over a range of frequencies from 100Hz to 16kHz, and over a range of sound pressure levels from 92.9dB to 116.1dB. Fig. 38 is shows the test setup used to test the chinchilla tympanic membrane.

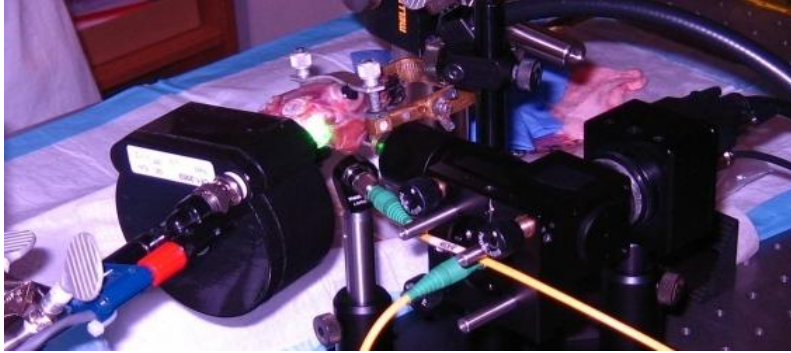


Fig. 38. Chinchilla Test.

Doctors from Massachusetts Eye and Ear Infirmary acquired a number of time-average interferograms and stroboscopic phase images for ordered and complex vibration patterns in the tympanic membrane. Unfortunately, due to the low speckle per fringe resolution few of the stroboscope phase images acquired during the testing were able to be unwrapped. A time-averaged image of a simple mode shape in the chinchilla tympanic membrane demonstrating the large speckle size is shown in Fig. 39.

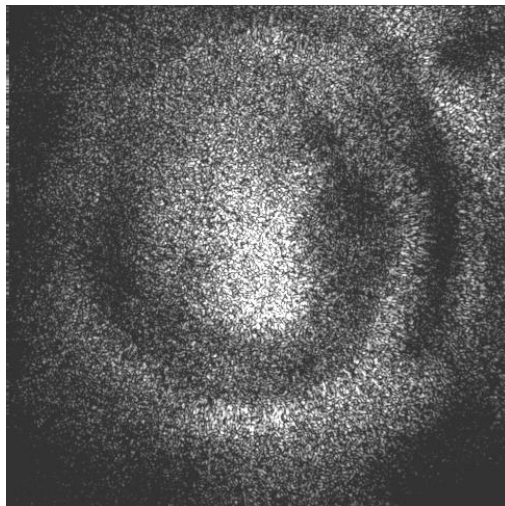


Fig. 39. Time-Averaged Image of Chinchilla Tympanic Membrane at 700 Hz, 102.9dB SPL.

The large speckle size was due to two main factors: small diameter optics inherently have a larger speckle size; and the achromat imaging lens was mounted unparallel to the optical axis. These issues were dealt with by replacing the 5mm diameter achromat lens with a 6.35mm diameter achromat lens, as well as getting the achromat lens mounted professionally to ensure its alignment to the optical axis.

The speckle size was reduced by installing the new 6.35mm diameter achromat imaging lens, though the miniaturized otoscope head has not yet tested tympanic membrane with the improved optics.

## 11. Recommendations and Future Work

The feedback from the medical professionals who performed experiments with the otoscope head provided conclusions and indicated future work regarding the system.

The primary response to the system was positive and in regards to the miniaturized size. The otoscope head is less than 10% the previous generation in overall volume. Additionally, the more otoscope-like appearance was indicated as an important improvement over the previous generation as it will provide a more seamless integration into current clinical practices.

The focusing system, which utilizes a translational tube, was immediately intuitive to all the professionals who experimented with the system. This is a vast improvement over the previous system, whose focusing system was often neglected in favor of moving the sample (which the physicians found simpler despite requiring the unbolting and careful shifting of the sample).

The depth of field has been increased which was beneficial in reducing the time require to set up and administer a round of experiments.

The device was found to have an insufficient speckle size for the work of the researchers at MEEI as originally tested. A larger diameter imaging lens was subsequently installed which reduced the speckle size. Tests with the news lens have yet to be completed by the MEEI researchers but it is expected the speckle size is reduced to an acceptable size for TM measurement.

Thermomechanical stability was addressed only through the reduction of the degrees of freedom of the system, and a full-scale investigation into methods to increase the thermomechanical stability is paramount. Much of the instability of the system stems from having two separate fibers which transfer light to the optical head. This system should be optimized.

A production-type package should be fully designed and manufactured for the optical layout prototyped. A printed circuit-board camera will allow for numerous packaging options and should be considered for the next generation.

Finally, an illumination system for the tympanic membrane must be incorporated into the design and packaging. A bundle of optical fibers to carry light to a ring surrounding the speculum is suggested for further investigation as current otoscopes utilize this system and it provides even illumination on the TM.

## 12. References

- 
- <sup>1</sup> Furlong, C., Rosowski, J.J., Hulli, N. and Ravicz, M.E., *Preliminary analyses of tympanic-membrane motion from holographic measurements*, SEM 8<sup>th</sup> International Symposium Series on MEMS and Nanotechnology (ISMAN), Springfield, MA, June 2007
- <sup>2</sup> Schubert, E.D., *Hearing: Its Function and Dysfunction*, Springer-Verlag, NY, 1980
- <sup>3</sup> Phon.ox.ac.uk. Home Page. Retrieved 15 December 2008, [http://www.phon.ox.ac.uk/~jcoleman/speaking\\_hearing.htm](http://www.phon.ox.ac.uk/~jcoleman/speaking_hearing.htm)
- <sup>4</sup> Katz, J., *Handbook of Clinical Audiology: Fourth Edition*, Williams & Wilkins, MD, 1994
- <sup>5</sup> Standring, S., *Gray's Anatomy: The Anatomical Basis of Clinical Practice, Thirty-Ninth Edition*, Elsevier Ltd., NY, 2005
- <sup>6</sup> Rowsowski, J., personal communication, March 24, 2009
- <sup>7</sup> Wajnberg, J. M.D., "The true shape of the tympanic membrane," *The Journal of Laryngology and Otology*, 101:538-541, 1987
- <sup>8</sup> Koike, T., Wada, H., Kobayashi, T., "Modeling of the human middle ear using the finite-element method," *J. Acoust. Soc. Am.*, 111:1306-1317, 2002
- <sup>9</sup> Chole, R.A., Kodama, K., "Comparative histology of the tympanic membrane and its relationship to cholesteatoma," *Ann. Otol. Rhinol. Laryngol.*, 98:761-766, 1989
- <sup>10</sup> Fay, J., Puria, S., Decraemer, W., Steele, C., "Three approaches for estimating the elastic modulus of the tympanic membrane," *Journal of Biomechanics*, 38:1807-1815 2005
- <sup>11</sup> Lim, D.J., "Structure and function of the tympanic membrane: a review," *Acta oto-rhino-laryngologica Belg.*, 49:101-115, 1995
- <sup>12</sup> Lim, D.J., "Tympanic Membrane: Electron microscopic observation part I: pars tensa," *Acta oto-laryngologica*, 66:181-198, 1968
- <sup>13</sup> Haskel, S. and Sygoda, D., *Biology, A contemporary Approach*, Amsco, NY, 1996
- <sup>14</sup> Williams, K.R., Lesser, T.H.J., "A finite element analysis of the natural frequencies of vibration of the human tympanic membrane. Part I.," *British Journal of Audiology*, 24:319-327, 1990
- <sup>15</sup> Deafness in Dogs & Cats. Frequency Hearing Ranges in Dogs and Other Species. Retrieved 20 January 2008, <http://www.lsu.edu/deafness/HearingRange.html>
- <sup>16</sup> Tontechnik-Rechner – sengpielaudio. Decibel Table – Comparison Chart. Retrieved 20 January 2008, <http://www.sengpielaudio.com/TableOfSoundPressureLevels.htm>

- 
- <sup>17</sup> Project proposal. Rosowski, John J.
- <sup>18</sup> Dywer, B., Maccaferri, M., Wester, C., “Design and Realization of a Laser Holographic Oscope,” MQP, WPI-ME, 2008
- <sup>19</sup> Rabbitt, R.D., Holmes, M.H., “A fibrous dynamic continuum model of the tympanic membrane,” *J. Acoust. Soc. Am.*, 80:1716-1728, 1986
- <sup>20</sup> V.V. Tuchin., “Light scattering studies of tissues,” *Physics-Uspekhi*, 40:495-515, 1997
- <sup>21</sup> Tuchin, V.V., Utz, S.R., Yaroslavsky, I.V., “Tissue optics, light distribution, and spectroscopy,” *Optical Engineering*, 33:3178-3188, 1994
- <sup>22</sup> Sundberg, M., Peebo, M., Oberg, P.A., Lundquist, P.G., Stromberg, T., “Diffuse reflectance spectroscopy of the human tympanic membrane in otitis media,” *Physiol. Meas.*, 25:1473-1483, 2004
- <sup>23</sup> Doladov, M.Yu., Kazakevich, V.S., Kalashnikov, I.G., Kupaeva, V.V., Shcherbakov, V.A., “Optical reflection of the human tympanic membrane,” *J. App.Spectroscopy*, 66:708-710, 2001
- <sup>24</sup> Dirckx, J.J.J., Decraemer, W.F.,” Reflective coatings in optical interferometry for in-vitro studies of the eardrum,” *SPIE*, 2927:2-10, 1996
- <sup>25</sup> Hulli, N., “Development of an optoelectronic holographic otoscope system for characterization of sound-induced displacements in tympanic membranes,” *Thesis, WPI-ME*, 2008
- <sup>26</sup> Waldo’s World “Oscope” (2009). <http://www.waldosworld.org/gallery03/otoscope.jpg>
- <sup>27</sup> Gerrard, Anthony. Matrix Methods in Optics (1975). The Gresham Press, Old Woking, Surrey, UK.
- <sup>28</sup> Adapted from 27
- <sup>29</sup> Nufern.com. “Fiber Details – 460HP” (2004). [http://www.nufern.com/fiber\\_detail.php/95](http://www.nufern.com/fiber_detail.php/95)
- <sup>30</sup> Silicon Imaging. “Silicon Imaging is proud to continue its innovation in ultra” (2009). <http://www.siliconimaging.com/SI-1280CL%20spec.htm>
- <sup>31</sup> GRINTECH.de (2006). [http://www.grintech.de/datasheets/grin\\_endoscope\\_systems.pdf](http://www.grintech.de/datasheets/grin_endoscope_systems.pdf)
- <sup>32</sup> NSG Europe “Rod Lens Table” (2009). <http://www.nsg europe.com/technology/rodlens.shtml>
- <sup>33</sup> Nikon.com “Nikon MicroscopyU – Concepts and Formulas” (2009). <http://www.microscopyu.com/articles/formulas/formulasfielddepth.html>
- <sup>34</sup> NSG Europe “Physics of the Selfoc Lens” (2009). <http://www.nsg europe.com/physics.shtml>

- 
- <sup>35</sup> Thorlabs.com “Visible Achromat Doublets” (2008).  
[http://www.thorlabs.com/NewGroupPage9.cfm?ObjectGroup\\_ID=120&pn=AC050-010-A1&CFID=34603318&CFTOKEN=89480372](http://www.thorlabs.com/NewGroupPage9.cfm?ObjectGroup_ID=120&pn=AC050-010-A1&CFID=34603318&CFTOKEN=89480372)
- <sup>36</sup> Thorlabs.com “Visible Achromat Doublets” (2008).  
[http://www.thorlabs.com/NewGroupPage9.cfm?ObjectGroup\\_ID=120&pn=AC050-010-A1&CFID=34603318&CFTOKEN=89480372](http://www.thorlabs.com/NewGroupPage9.cfm?ObjectGroup_ID=120&pn=AC050-010-A1&CFID=34603318&CFTOKEN=89480372)
- <sup>37</sup> Silicon Imaging. “Spectral Response” (2009).  
<http://www.siliconimaging.com/si1280%20Spectral%20Response.htm>
- <sup>38</sup> EdmundOptics.com. “1951 USAF Glass Resolution Targets.” (2009).  
<http://www.edmundoptics.com/onlinecatalog/displayproduct.cfm?productID=1790>
- <sup>39</sup> Hernandex-Montes, M. del Socorro, Furlong, C., Rosowski, J. J., Hulli, N., Harrington, E., Cheng, T. J., Ravicz, M. E., Santoyo, F. M., “Optoelectronic holographic otoscope for measurement of nano-displacements in tympanic membranes,” 8
- <sup>40</sup> Timoshenko, S., Young, D.H., W. Weaver, Jr., Vibration Problems in Engineering: Fourth Edition, 415-426, 1974
- <sup>41</sup> Mece.ualberta.ca. “Modal Analysis of Cantilever Beam.” (2009).  
<http://www.mece.ualberta.ca/tutorials/ansys/IT/Modal/Modal.html>
- <sup>42</sup> Oberg, E., Jones, F.D., Horton, H. L., Ryffel, H. H.. *Machinery’s Handbook: 28<sup>th</sup> Edition*, Industrial Press, NY, 2008
- <sup>43</sup> Ansys,. *V 9.0*. Ansys, Inc., Canonsburg, PA, 2007

### 13. Appendix A. Biology Summary – Human TM.

<b>Dimensions:</b>	9-10mm horizontally, 8-9mm vertically
<b>Density:</b>	1200kg/m <sup>3</sup>
<b>Thickness:</b>	34μm (pars tensa); 110μm (pars flaccida)
<b>Elastic Modulus:</b>	Conflicting literature, between 0.1 and 0.3GPa
<hr/>	
<b>Max displacement:</b>	1μm
<b>Min displacement:</b>	sub-nanometer scale
<b>Audible Freq's:</b>	16Hz – 20kHz. Complex patterns beginning at 3kHz.
<b>Safe dB SPL's:</b>	0-100dB
<hr/>	
<b>Percent light reflected:</b>	0-17%
<b>Max reflective λ:</b>	620nm – 680nm
<b>Coatings of interest:</b>	White Chinese ink, Magnesium oxide (obtained by burning Mg wire)

## **14. Appendix B. TracePro Model Details.**

Lambda Research's *TracePro* suite was used for the three dimensional modeling and ray tracing analysis of the optical configuration. In order for the future of this project to benefit fully from our work it is important that a working knowledge of TracePro be developed. With knowledge of the TracePro suite it is possible to understand, analyze and continue the optimization studies of the configuration developed. The team feels the model is an important contribution to the project and it should be further investigated.

In this appendix we developed a tutorial which should provide a stable grounds to begin working in TracePro, as subsequently outline the specifics of the TracePro model created.

## 14.1. Introduction to TracePro

### 14.1.1. Defining Geometry and Optical Characteristics

TracePro is a three dimensional modeling CAD suite, much like AutoCAD, Solidworks, Pro/E, and similar applications. As such, it should look and feel familiar to those capable in any CAD environment. Fig. 40 is a screenshot of the TracePro window.

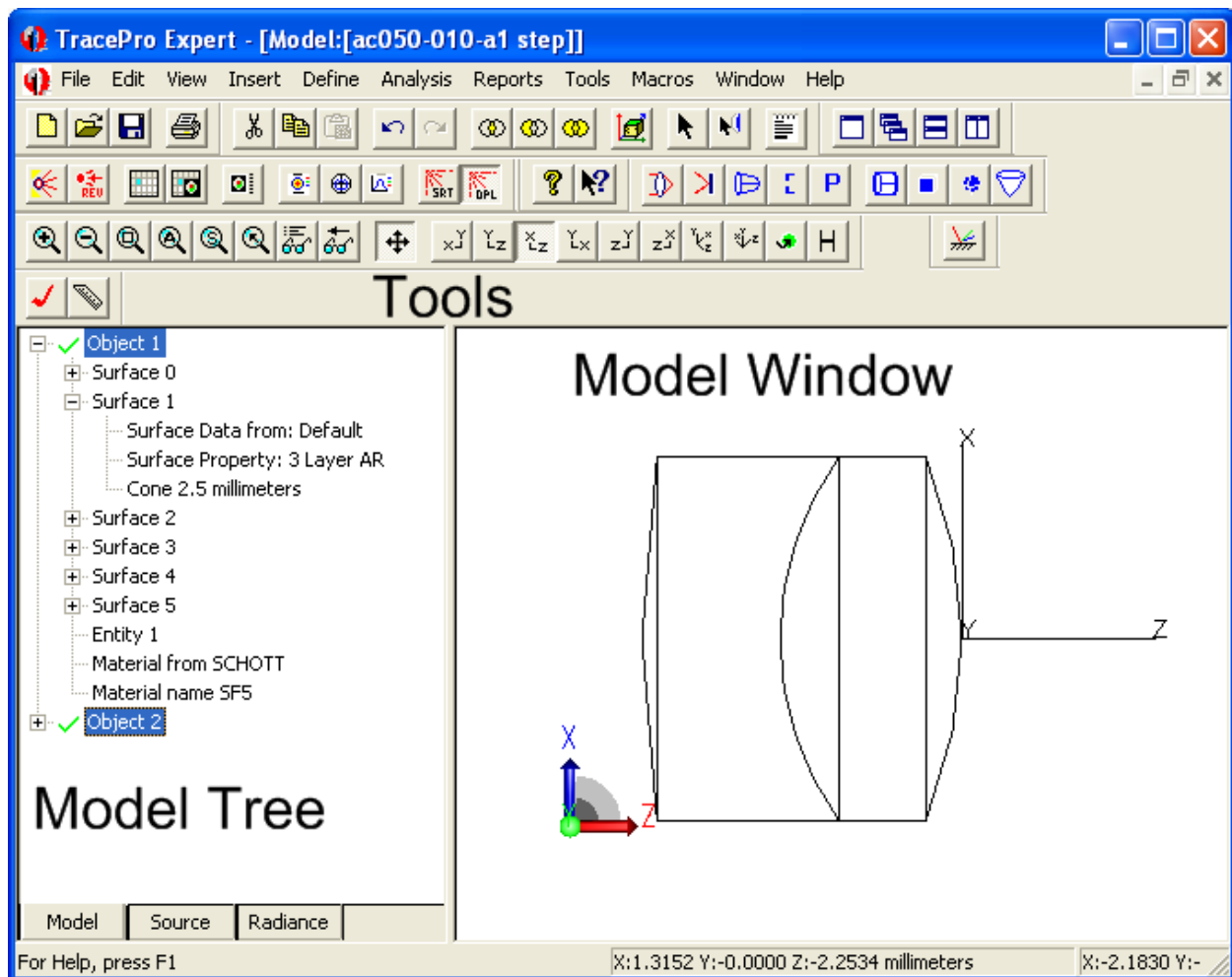


Fig. 40. Annotated screenshot of TracePro environment.



The 'Primitive Solid' selection is used often, and allows you to create common solid objects, such as cubes, cones, and spheres.

Complex 3d geometries are constructed by inserting overlapping primitive solids and using the Boolean operations, accessible from the Boolean toolbar:



Fig. 44. TracePro: Boolean toolbar.

Alternatively, these operations can be accessed from the 'Edit' menu. These operations will become available for selection after first selecting two objects.

At the left of the image is the Model Tree. In *TracePro*, solid objects consist of multiple surfaces (as shown in the tree structure):

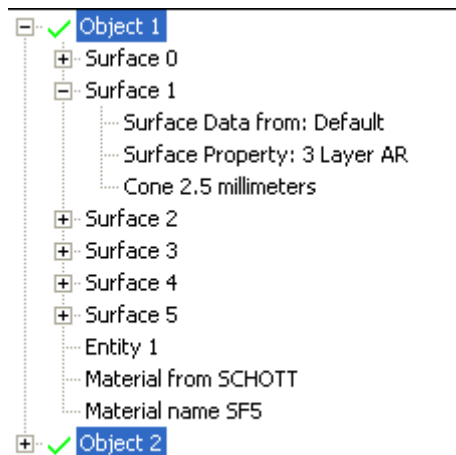


Fig. 45. TracePro: Example Model Tree.

Properties, for example material properties (such as refractive indices; absorption, reflection, and transmission coefficients; etc...) and surface properties (such as surface coatings and characteristics) can be applied to objects or individual surfaces by right clicking and selecting 'Properties':

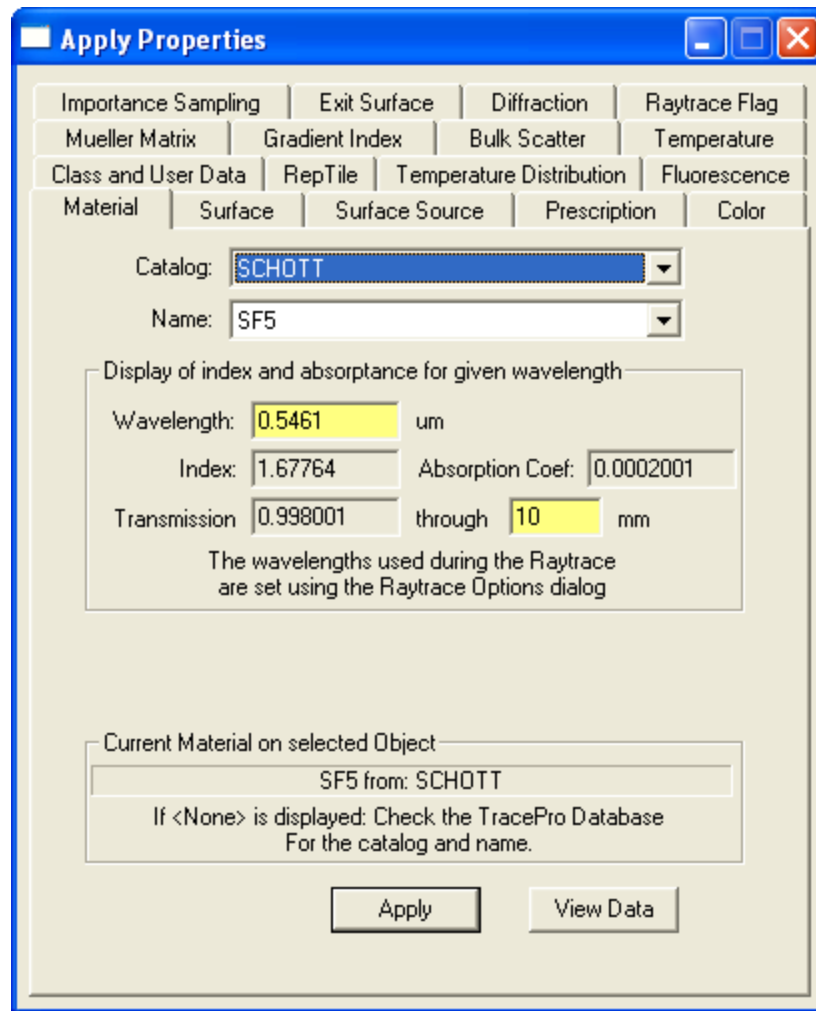


Fig. 46. TracePro: 'Apply Properties' dialog.

All characteristics of the TracePro objects and surfaces can be changed and applied via this dialog. *TracePro* features data on numerous commercial materials and coatings (see the 'Catalog' and 'Name' drop-boxes). To further investigate or alter the properties of a material or coating click the 'View Data' button.

This produces the Material Property Editor, which provides the mathematical model used for a particular item, as well as the coefficients which characterize it.

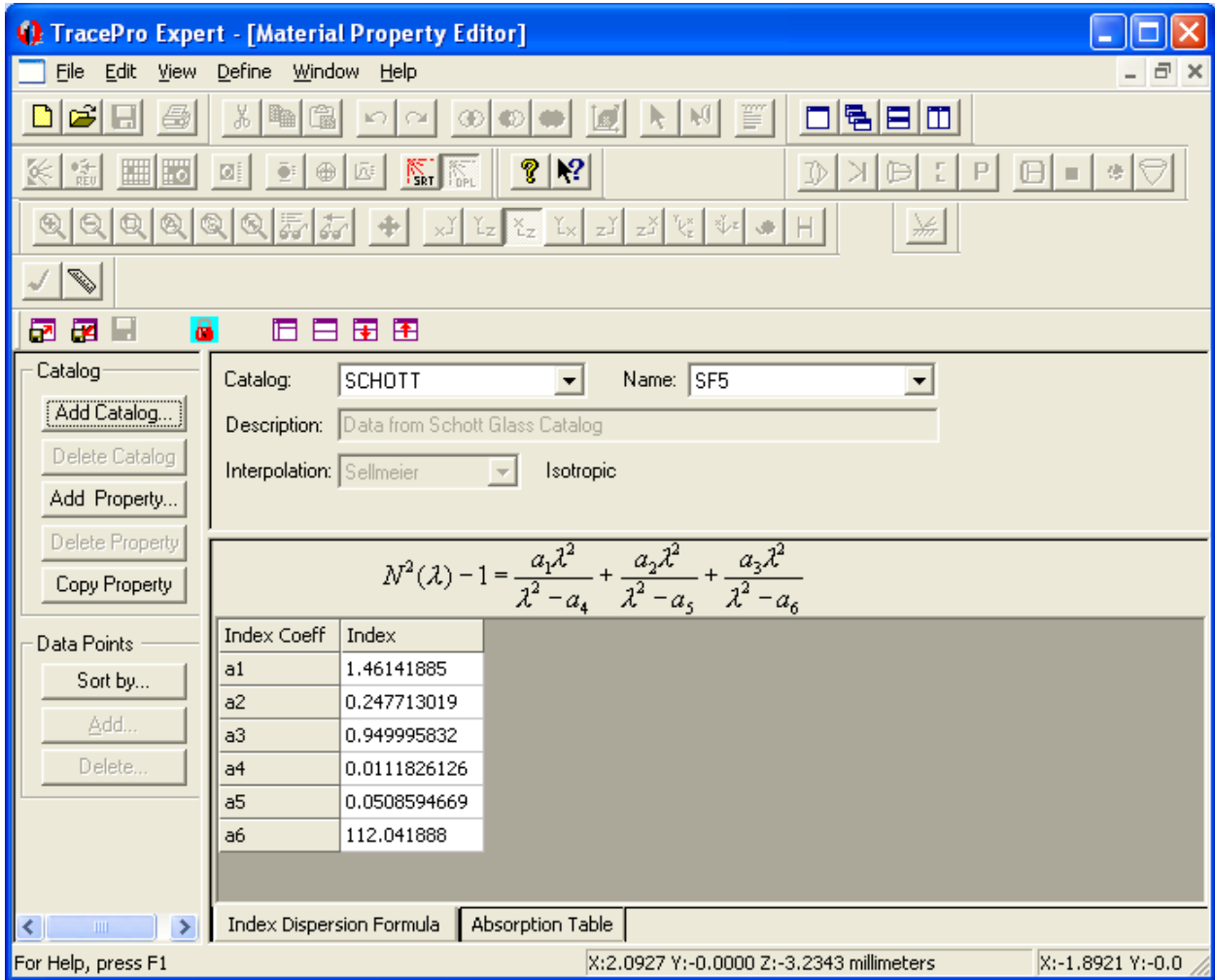


Fig. 47. TracePro: Material Property Editor.

This editor is necessary to input new materials into the system. Occasionally, updated catalogs are made available at the Lambda Research website (LambdaResearch.com), and can be imported into the system to provide more up-to-date models of optical components.

All the different catalog property editors can be accessed via the ‘Define’ menu.

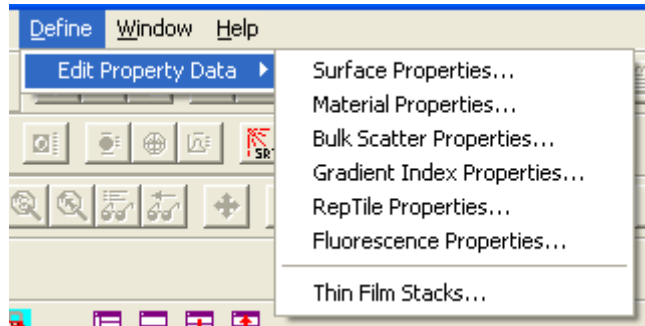


Fig. 48. TracePro: Menu for editing of property data catalogs.

In summary, TracePro is very similar in usage to other geometric CAD software. On top of the geometry characteristics, however, optical properties can be applied to objects and surfaces by selecting them in the model tree and choosing 'Properties'.

#### **14.1.2. Light sources and ray trace options**

In order to perform a ray trace on the model created its necessary to define a light source. There are three types of light sources in TracePro: Grid sources, surface sources, and a file sources. Clicking the tab 'Sources' in the model tree switches to a source tree view. See Fig. 49.

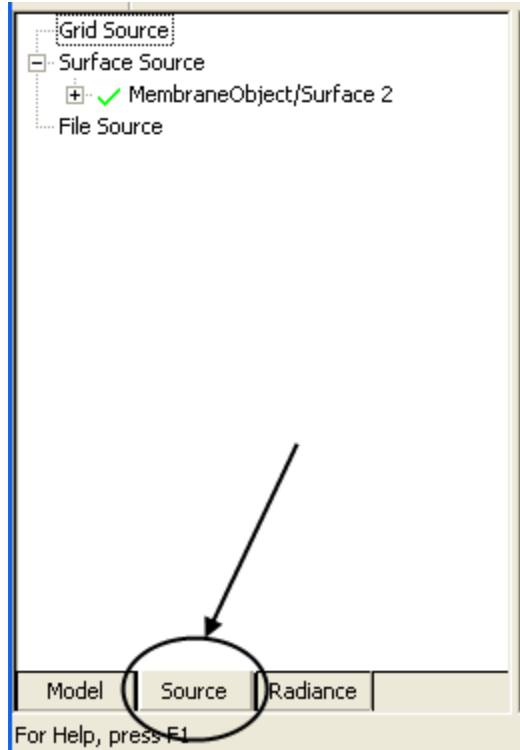


Fig. 49. TracePro: Source Tree.

Sources are defined by the 'Define' menu.

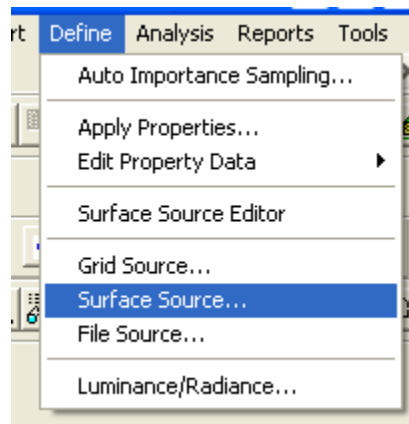


Fig. 50. TracePro: 'Define' menu.

A file source allows you to input a text file with a specific point intensities specified. A surface source allows you to define a surfaces light emitting properties.

Grid sources are the most versatile sources and the most often used in laser-based illumination design. The dialog for a grid source is presented below, both 'grid' and 'beam' setup tabs.

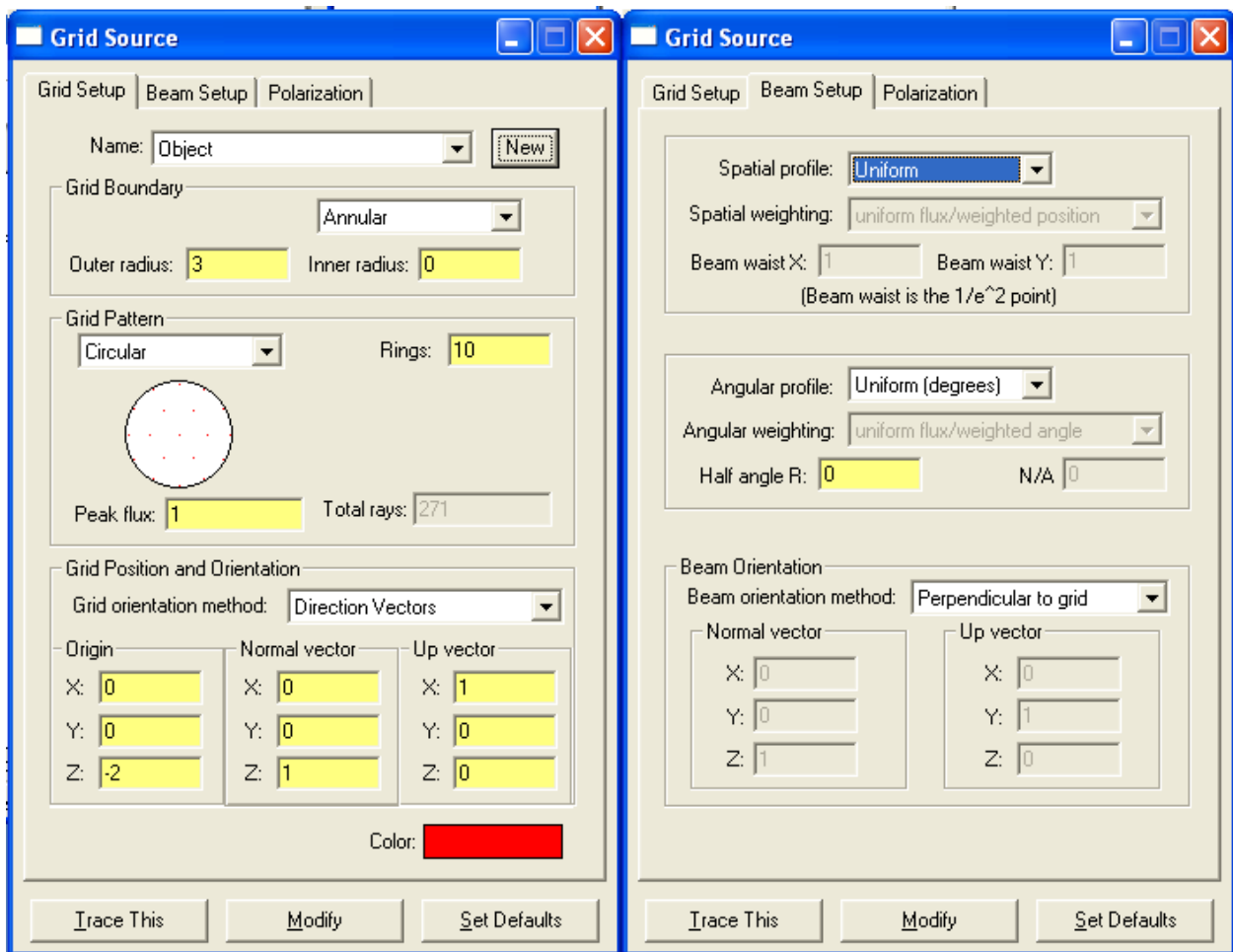


Fig. 51. TracePro: Definition of a grid source.

Several options are available in the ‘Grid Setup’ tab, including origin point, direction, peak flux, and shape and size. Additionally the input ‘Rings’ allows you to define the number of rays traced from the particular source. Increasing the number of rings in an annular grid will exponentially increase the number of rays. Computational time will vary between both number of rays in a source and the specifics of a model, as optical complexity greatly increases the number of computations the software is required to perform. For much of the work undertaken in this MQP, 30,000 rays was an acceptable starting point.

The ‘Beam Setup’ tab allows the definition of the profile of the beam. A Gaussian distribution, with a specific waist in the x and y directions, can easily be defined here. Note that selecting a Gaussian spatial distribution negates the pattern selection of the source, as a Gaussian distribution always uses a random pattern with Gaussian probabilities defining the annular shape.

A divergent beam can be defined via half angle in the ‘angular profile’ section of this window. Note that the combination of a Gaussian spatial distribution and a divergent beam allows for modeling of the output of laser light from an optical fiber.

With a source (or sources) defined, a raytrace can be performed. Prior to a raytrace, ray tracing options are available in the ‘Analysis->Ray Trace Options’ menu.

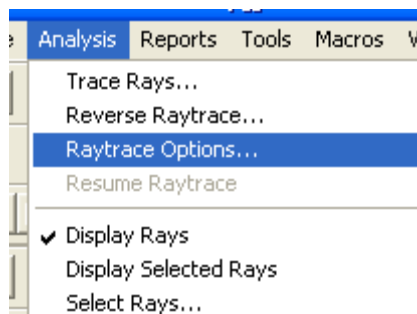


Fig. 52. TracePro: Accessing ‘Raytrace Options’.

The dialog of options is presented:

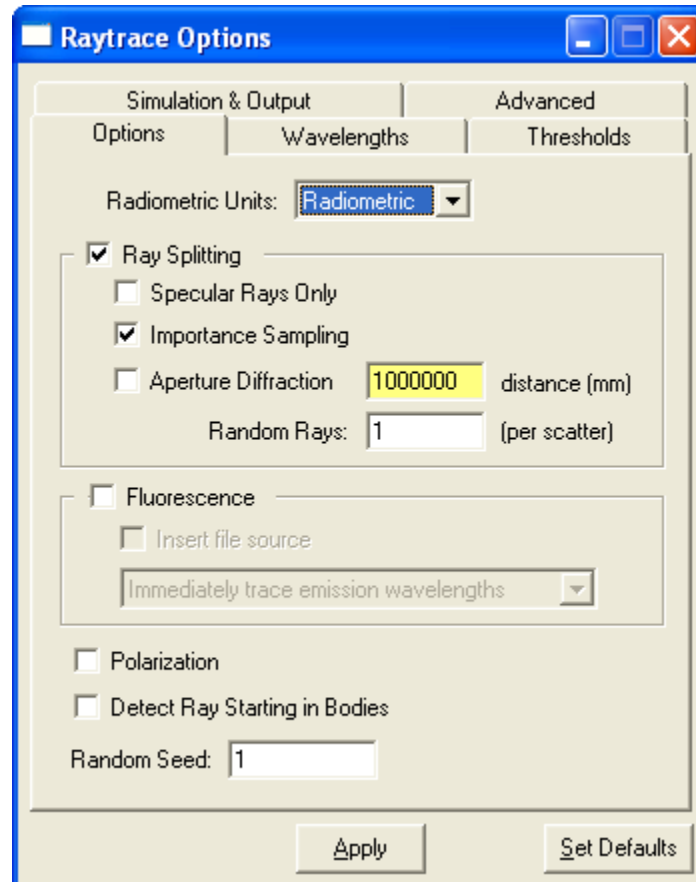


Fig. 53. TracePro: 'Raytrace Options' Dialog.

Here, ray splitting can be toggled on or off. Ray splitting refers to the behavior of a ray/surface interaction. With ray splitting on, a ray is split into multiple rays at each surface based on the absorption, reflection, and transmission coefficients of that surface. For example, if a surface has a reflection coefficient of .30 and a transmission coefficient of .70, a single ray will be split into two rays: One transmitted with a power 70% of the initial ray, and one reflected with a power 30% of the original.

Without ray splitting, an interaction instead happens probabilistically. Therefore, in the example above, the ray will be transmitted 70% of the time, and reflected 30% of the time. However, the interaction will NOT produce multiple rays.

Removing ray splitting can greatly reduce the computation time of a model, as the number of rays propagating through space is not exponentially increasing. In the MQP, ray splitting was found to have little effect on the outcome of the data, while decreasing computation time, and was most often not in effect.

The raytrace options menu also provides the definition of specific wavelengths, and the percentage power a ray must reach (compared to its original power) before it is excluded from the raytrace. Also, 'Importance Sampling' can be toggled on and off.

Importance Sampling causes TracePro to alter the Monte Carlo probability method used to favor certain surfaces. In other words, scattered ray directions favor locations indicated in the dialog. The overall probability is kept faithful by dividing by the amount of weighting used (all done internally in TracePro). Optimization of the amount of importance sampling allows vastly reduced computation times by allowing for a reduced total ray count. More information, including a tutorial for applying importance sampling, can be found in the 'Support' section of the Lambda Research website ([LambdaResearch.com](http://LambdaResearch.com)).

Importance sampling targets are applied from a surface to a point in space through the apply properties dialog. Each surface can have multiple targets.

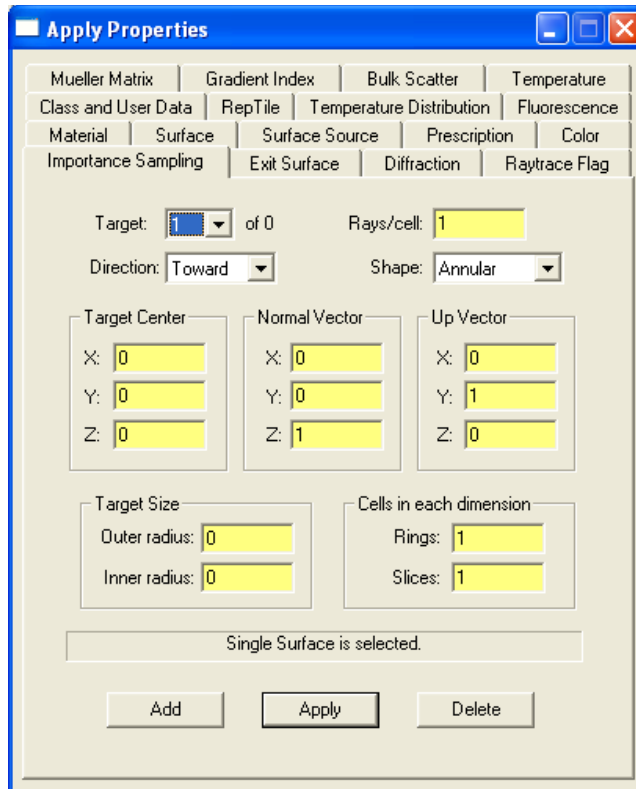


Fig. 54. TracePro: Importance Sampling target definition.

### 14.1.3. Tracing Rays and Analysis Tools

Tracing analysis tools are accessible from the 'Analysis' toolbar, as well as the button to perform a raytrace.



Fig. 55. TracePro: 'Analysis' Toolbar.

The leftmost icon performs a raytrace. The rightmost toggles the display of rays on and off.

Computation times are greatly reduced by disabling the display of rays. The '  ' button presents the sort rays dialog:

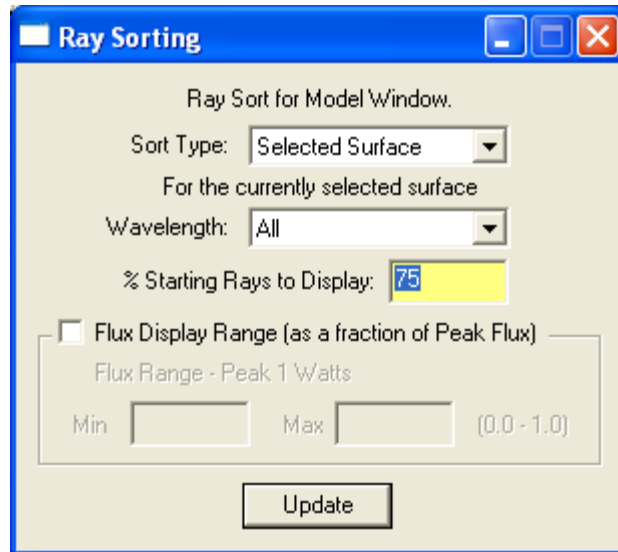


Fig. 56. TracePro: 'Ray Sorting' Dialog.

This menu is incredibly useful in reducing the number of rays displayed to a manageable and informational level. For example, the follow two screenshots (Fig. 57 and Fig. 58) present a model with a typical number of rays traced, and the same trace where only those rays which collide with the CMOS surface are displayed:

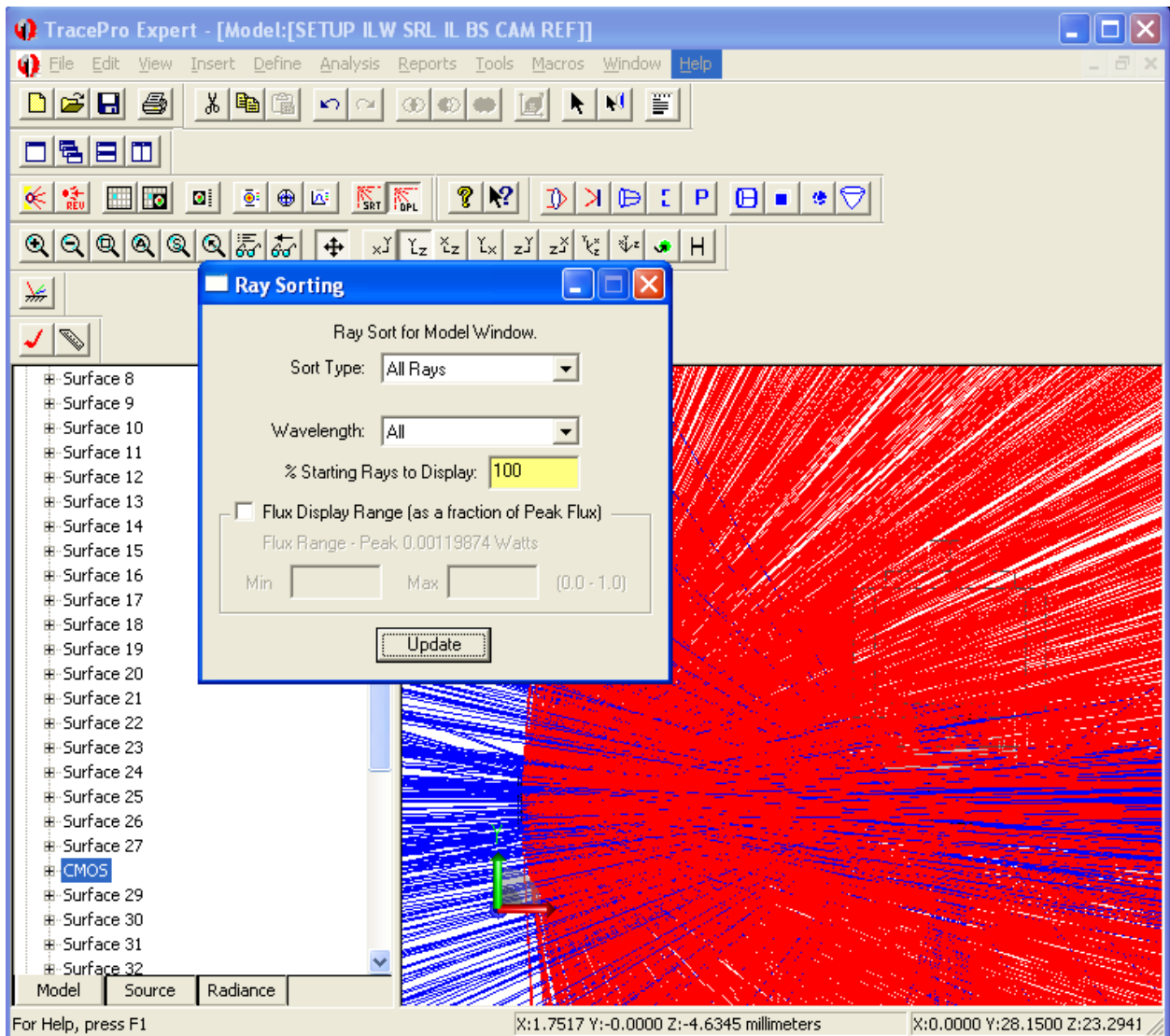


Fig. 57. TracePro: Raytrace with no ray sorting.

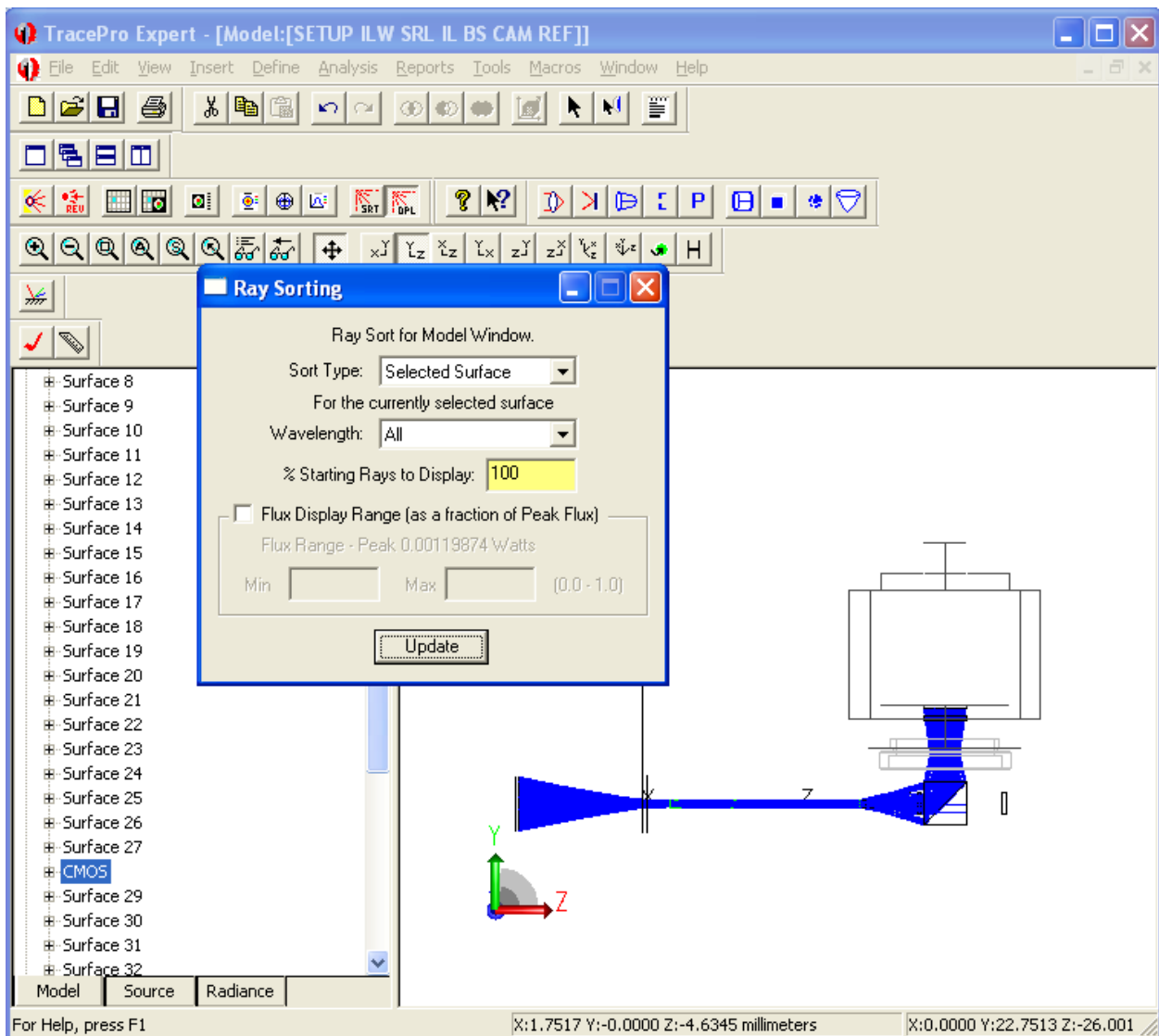


Fig. 58. TracePro: Ray trace with ray sorting, 'Selected Surface', enabled.

This middle six buttons of the 'Analysis' toolbar provide tools for analyzing the ray data.



Fig. 59. TracePro: Analysis Tool Buttons.

The leftmost two buttons present the ray tables, in spreadsheet format, for each ray traced through the system which encounters the surface selected. See Fig. 60.

SI1280 CMOS							
Wavelength	OPL	X Vec.	Y Vec.	Z Vec.	Type	History	Object
0.5461	0	-0.0466185	-0.0613205	0.997029		Emitted	Membr
0.5461	29.0864	-0.0288228	-0.0379126	0.998865	SpecTran		Cylindr
0.5461	-----	0.167595	-0.0338793	0.985274	SpecTran	Coinc Surf	Cylindr
0.5461	-----	0.167595	-0.0338793	0.985274	SpecTran		SRL
0.5461	-----	-0.272143	0.054617	0.960706	SpecTran		SRL
0.5461	-----	-0.272143	0.054617	0.960706	SpecTran		Absorb
0.5461	-----	-0.272143	0.054617	0.960706	SpecTran		Absorb

Fig. 60. TracePro: Ray table excerpt.

Often of more use is the ‘Irradiance Map’ selection, which provides a map of the light intensities experienced on the selected surface.

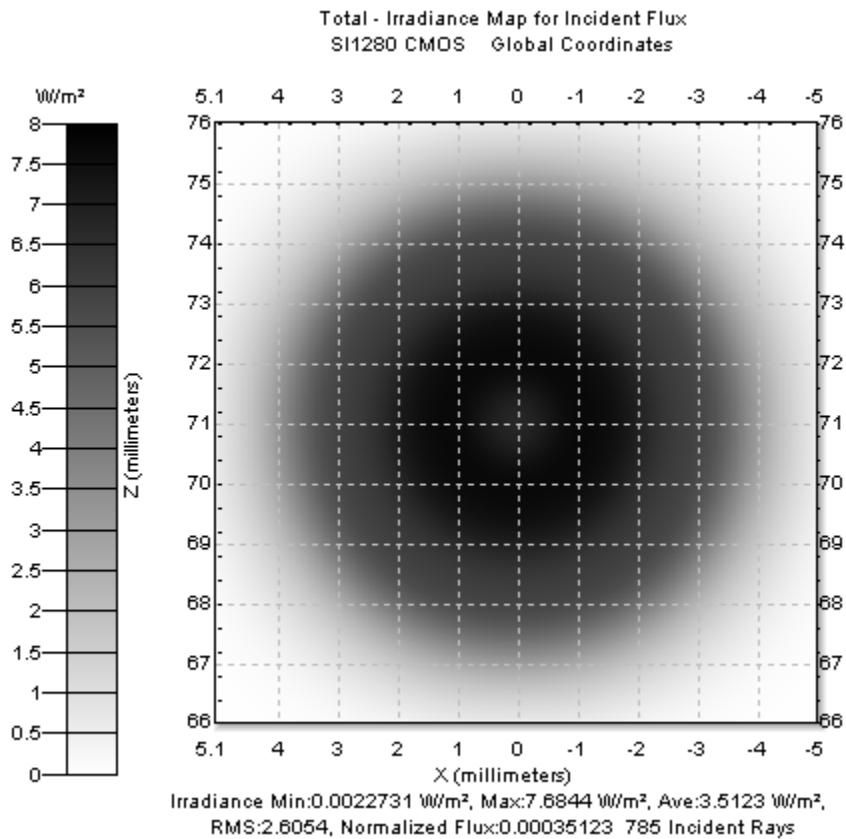


Fig. 61. TracePro: Sample Irradiance Map.

This tool was used above all others to evaluate the performance and function of the optical system. Options for the irradiance map are accessible by right clicking the map and selecting ‘Irradiance/Illuminance options’. Be sure the normal and up vectors are set appropriately for the surface under investigation, and note the availability of line profiles, logarithmic plotting, contour plotting, and various other display options.

Often, an irradiance profile is desired at a location between surfaces. In this case, simply create a thin block with no material or surface properties at the location of interest. Monitor the distribution at this plane in space by changing the irradiance map to display incident light (as opposed to absorbed, via the ‘Irradiance/Illuminance options’ dialog) on a surface of this block.

The preceding information, combined with a short time spent experimenting with the program, should provide an ample understanding for future *TracePro* computational analysis. More advance techniques are available in the *TracePro* suite but require formal training for full utilization.

## 14.2. Oscope Head Model Details

Details about the modeling of each optical component follow. The final step in each components modeling was the demonstration of a faithful Gaussian intensity distribution throughput.

For the source of specifications listed as ‘Manufacturer’s Specification,’ see Appendix D.

### 14.2.1. GRIN Lens ILW

The SRL GRIN lens purchased from NSG America has two components, a ILW lens cemented to the front of a GRIN rod lens. The ILW lens parameters are listed below:

Table 8. ILW Tracepro specifications.

Characteristic	Value	Source
Diameter	2 mm	Manufacturer’s Specification
Length	6.54 mm	Manufacturer’s Specification
Material and GRIN coefficients	SELFOC SLW 300	Material was identified as proprietary, but was identified as a SELFOC material, by NSG America representative Walter Boyles. The TracePro catalog contains several SELFOC materials, SLW300 matched the refractive index on axis provided from <a href="http://www.nsgamerica.com">http://www.nsgamerica.com</a> , and resulted in rays which are focused directly behind the ILW, as expected by the function of the lens.

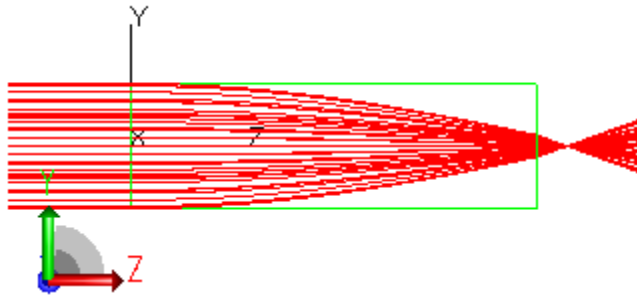


Fig. 62. TracePro: Image of raytrace through ILW component, with characteristic result.

### 14.2.2. GRIN ROD

Table 9. GRIN rod TracePro parameters.

Characteristic	Value	Source
Diameter	2 mm	Manufacturer's Specification
Length	43.87 mm	Inspection Certificate supplied with SRL combination lists overall length as 50.41mm. 50.41mm less 6.54 mm for imaging lens equate a rod length of 43.89mm.
Material and GRIN coefficients	SELFOC SLW 200	Material was identified as proprietary, but was identified as a SELFOC material, by NSG America representative Walter Boyles. The TracePro catalog contains several SELFOC materials; SLW200 closely matched the pitch specified with the length specified.
Pitch	0.5	Inspection Certificate supplied with Lens.



Fig. 63. TracePro: Image of raytrace through SRL (ILW and Rod combination) component, with characteristic result.

**Notes:** The GRIN elements are plano-plano, therefore the geometry can be created simply via inserting a primitive cylinder.

Ensure that when building a GRIN lens, both 'Material' and 'Gradient Index' properties are applied, and applied as the same type of SELFOC material. Also, the origin and direction (normal and up vectors) or the index must be specified. See Fig. 64, a screenshot of the apply properties dialog.

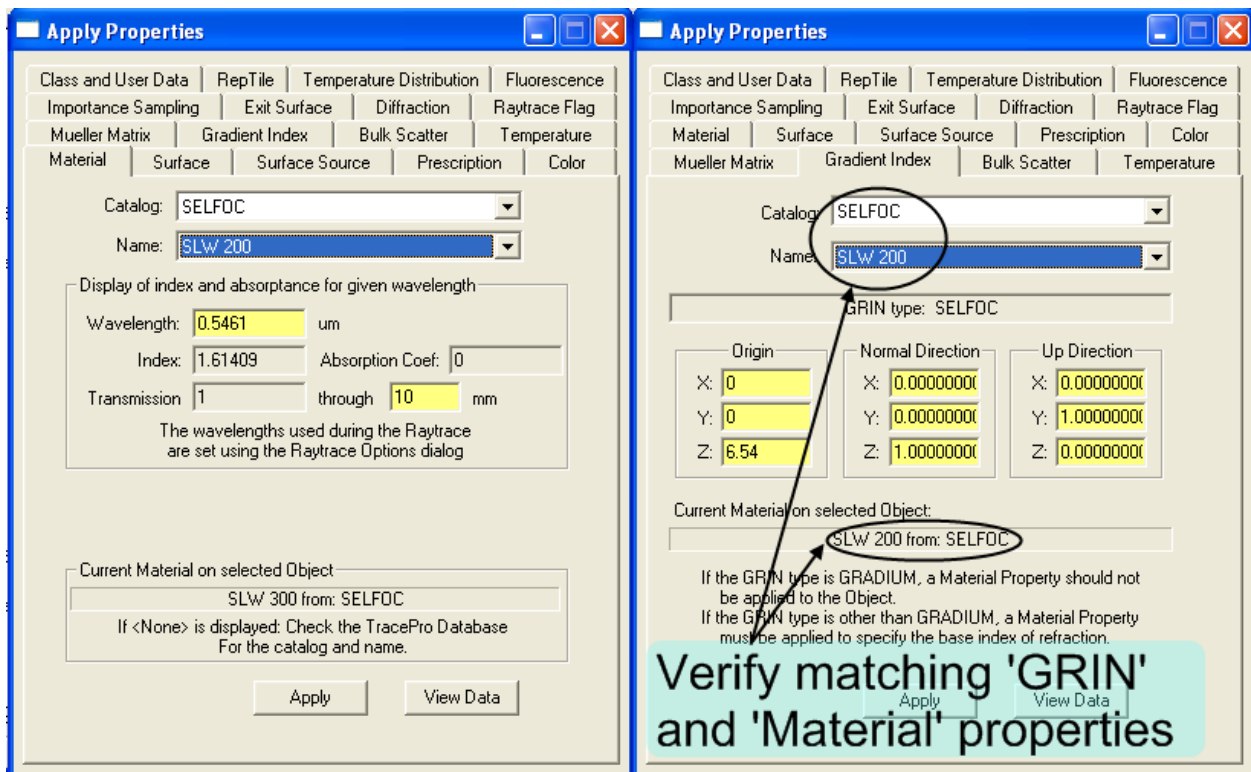


Fig. 64. TracePro: 'Apply Properties' dialog for Gradient Index definition.

The gradient index material is treated as a series of discreet small steps in order to facilitate the RTM method of raytracing. The size of this step can be selected in the 'Ray Trace Options' dialog ('Analysis' > 'Raytrace Options').

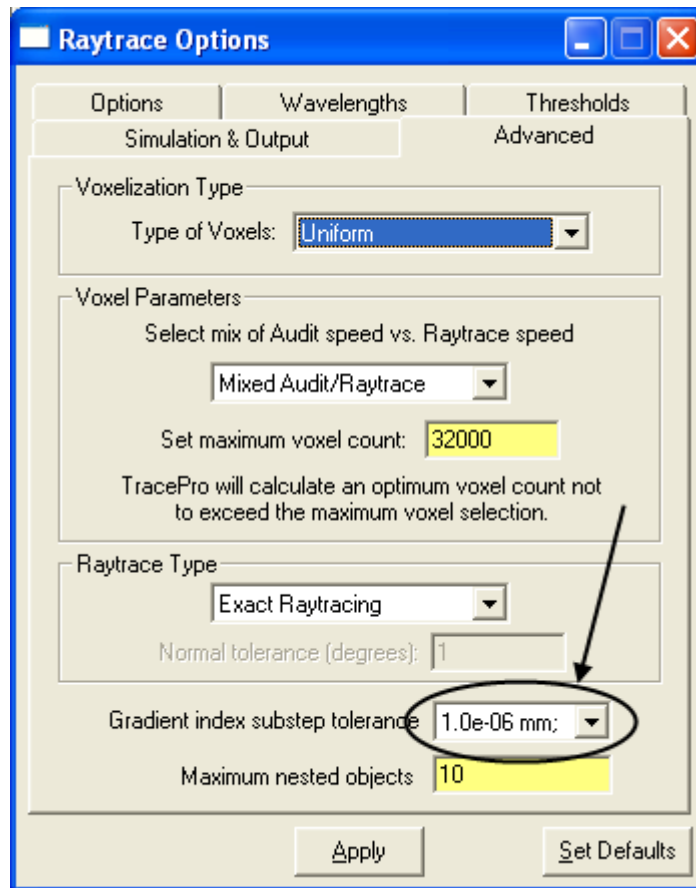


Fig. 65. TracePro: Selecting the step size of the gradient index.

### 14.2.3. Imaging Lens Achromat

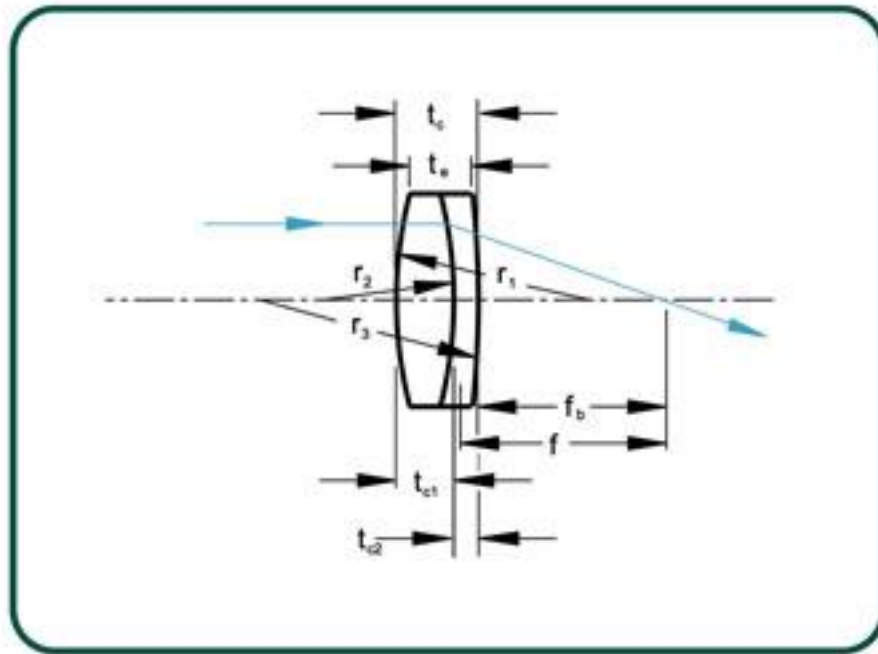


Fig. 66. Achromat diagram with variable convention<sup>1</sup>.

<sup>1</sup> Source: [http://www.thorlabs.com/NewGroupPage9.cfm?ObjectGroup\\_ID=120&pn=AC050-010-A1&CFID=34705449&CFTOKEN=15261036](http://www.thorlabs.com/NewGroupPage9.cfm?ObjectGroup_ID=120&pn=AC050-010-A1&CFID=34705449&CFTOKEN=15261036)

Table 10. AC050-010-A1 TracePro parameter table.

Characteristic	Value	Source
Diameter	5.0 mm	Manufacturer's Specification
R1	6.55 mm	Manufacturer's Specification
R2	-4.25 mm	Manufacturer's Specification
R3	-15.42 mm	Manufacturer's Specification
Tc1	2.5 mm	Manufacturer's Specification
Tc2	1.9 mm	Manufacturer's Specification
Te	3.7 mm	Manufacturer's Specification
Crown Material	Schott BAK4	Manufacturer's Specification
Flint Material	Schott SF5	Manufacturer's Specification
Focal Length	10mm	Manufacturer's Specification

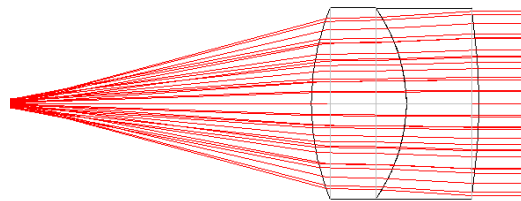


Fig. 67. TracePro: Image of raytrace through achromatic doublet component, with characteristic result.

**Notes:** Several achromatic lens doublets were modeled during the course of this project. Some of the geometries were able to be imported from STEP files available on the Thorlabs, or other manufacturer, website.

The lenses for which a compatible lens file was unavailable were constructed using the 'Insert Lens' feature to construct the lenses used in the doublet. For example; the crown consists of two curved surfaces. Inserting a lens with the appropriate radii of curvature, thickness, and material (see

Table 10) is the first step:

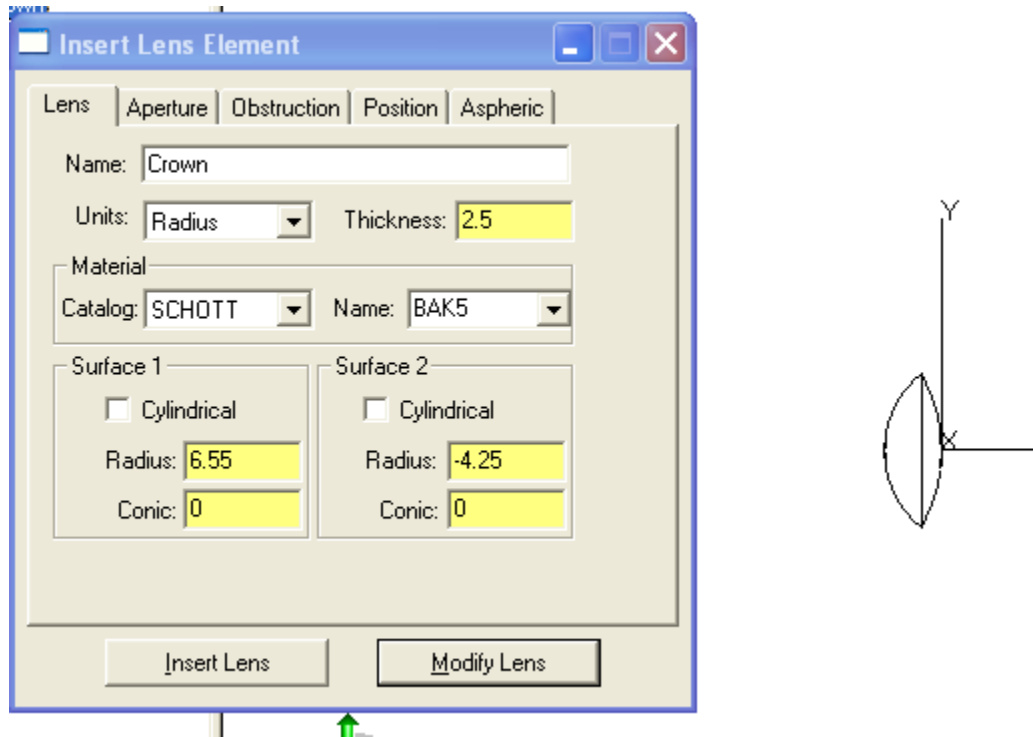


Fig. 68. TracePro: Building the achromat crown, showing the untrimmed surfaces.

The crown is then given the proper diameter by inserting a tube (from the primitive solids menu), selecting the crown and the tube sequentially, and using 'Boolean Subtract' (  ) tool. See Fig. 69 and Fig. 70.

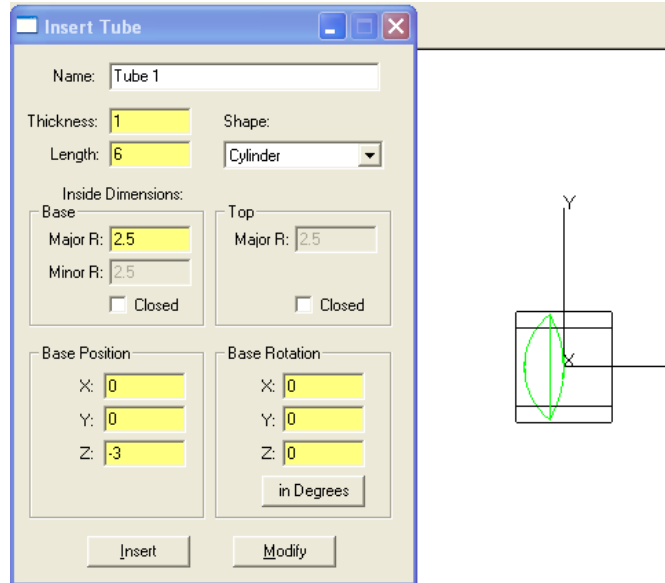


Fig. 69. TracePro: Building the achromat crown, showing the tube used to trim for diameter specification.

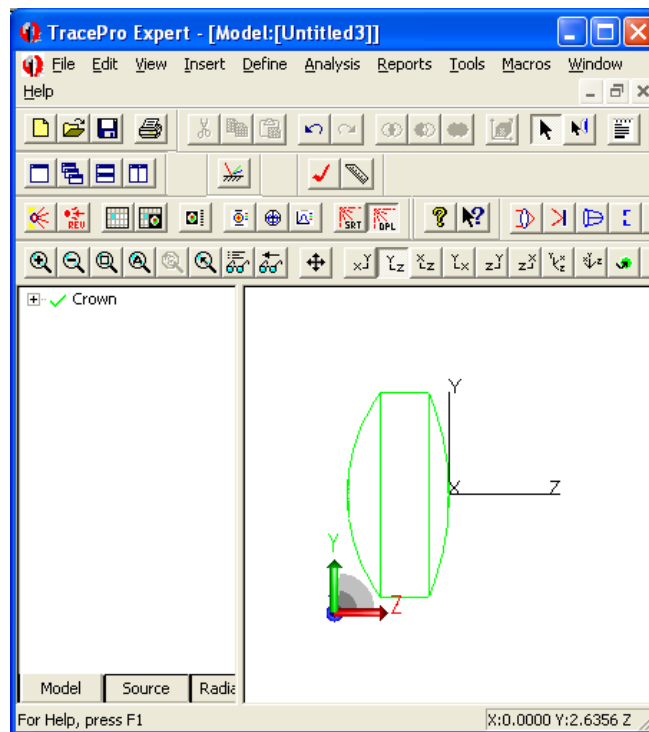


Fig. 70. TracePro: Resulting achromat crown.

This method of lens creation can be repeated for the creation of the flint of an achromatic doublet.

#### 14.2.4. Beamsplitter Cube

A Thorlabs BS010 beam splitter is used in the TracePro model. Properties follow:

Table 11. Beamsplitter (BS010) TracePro parameter table.

Characteristic	Value	Source
Side Length	10 mm	Manufacturer's Specification
Shape	Cube	Manufacturer's Specification

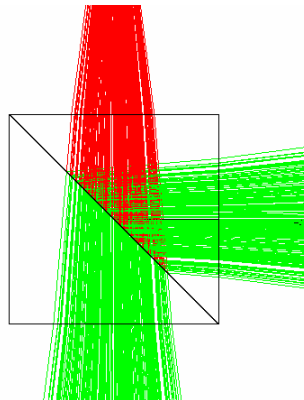


Fig. 71. TracePro: Image of raytrace through beamsplitter component, with characteristic result.

**Notes:** The construction of the BS cube was not immediately successful. The construction method which produced the best results is presented below:

First, create a cube of the appropriate size. Create a larger rectangle, at  $45^\circ$  from the first cube with one side which passes through the origin and which completely contains one half of the BS cube:

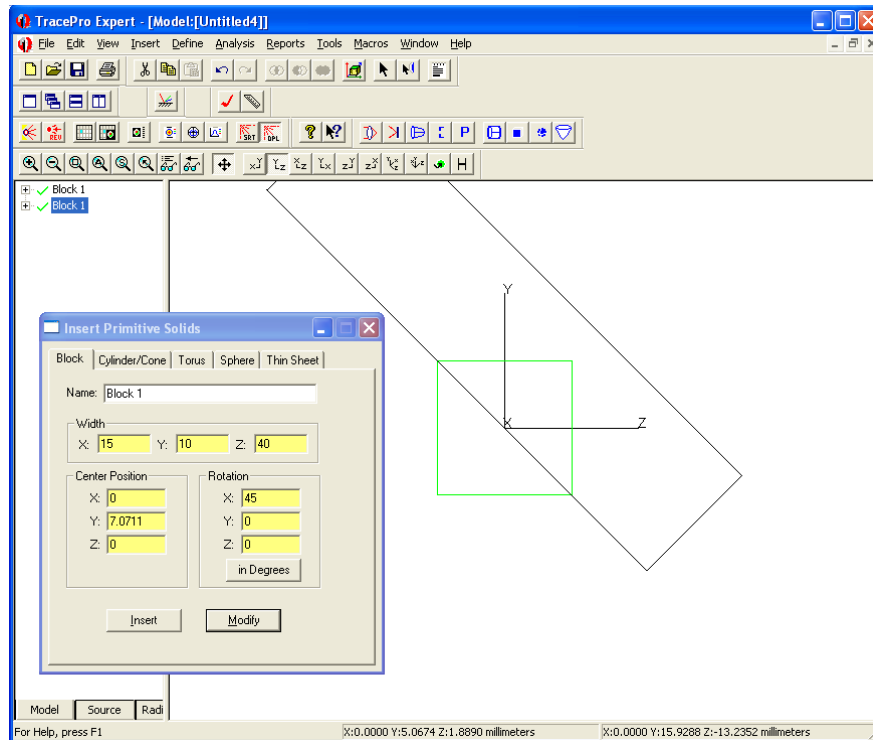


Fig. 72. TracePro: Construction of the BS cube, showing the base block and trimming rectangle  
 Use 'Boolean Subtract'  to create a prism from the BS cube.

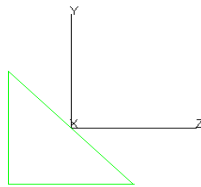


Fig. 73. TracePro: Beamsplitter prism.

Next, create another cube of equal size to the first, and copy the prism create above (so there are two overlapping instances):

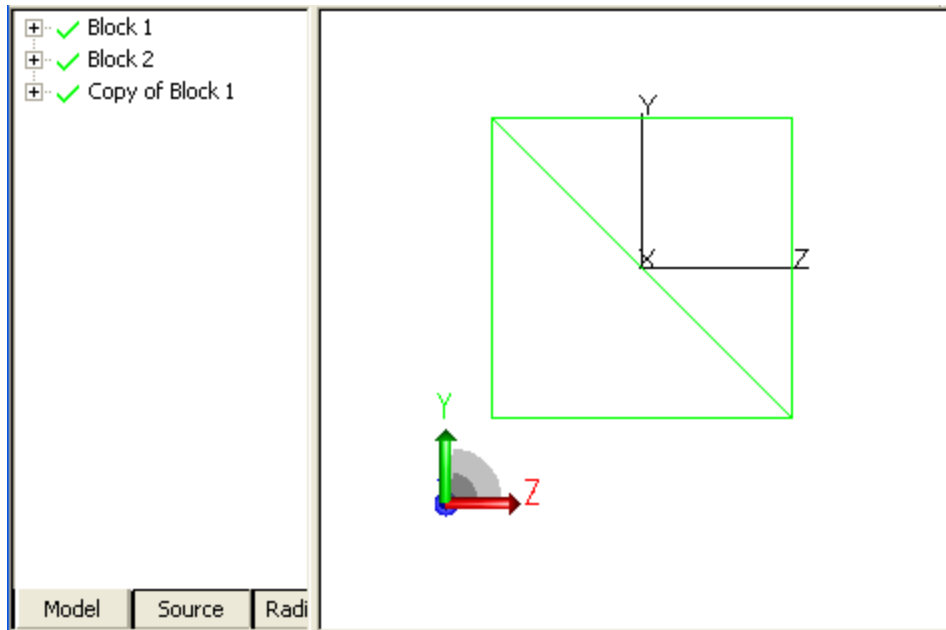


Fig. 74. TracePro: BS construction image, showing the three bodies required to create the splitter.

Select the copy of the prism, and the cube created, and use ‘Boolean Subtract’ to reduce the cube to a BS prism opposite the first. Apply AR coatings to the outside surfaces, and a Beamsplitter surface property to the diagonal. The BS should now behave as expected.

### 14.2.5. Optical Fibers

Optical fibers are easily modeled by using a cylinder of the appropriate glass and diameter. This was verified using the specifications from the 460HP fiber (see appendix D). ‘Sweep’ and ‘revolve’ allow for radiused corners and 3d paths for the fibers. Tracing light sources through the optical fibers was deemed as unnecessary computation time for this particular model, so for the purposes of the model the optical fibers are not physically modeled, only their light source output is.

The light output was modeled as a grid source with the following properties (see Nufern 460HP specification sheet):

Table 12. Grid Source parameters for Nufern 460HP optical fiber.

Characteristic	Value	Source
Diameter (1/e <sup>2</sup> Gaussian Waist)	3.5 μm	Manufacturer’s Specification
Beam half angle	7.45 degrees	Manufacturer’s Specification states a NA of 0.13, therefore the half angle is 7.44 degrees.
Distribution Profile	Gaussian	Inherent from Laser source.

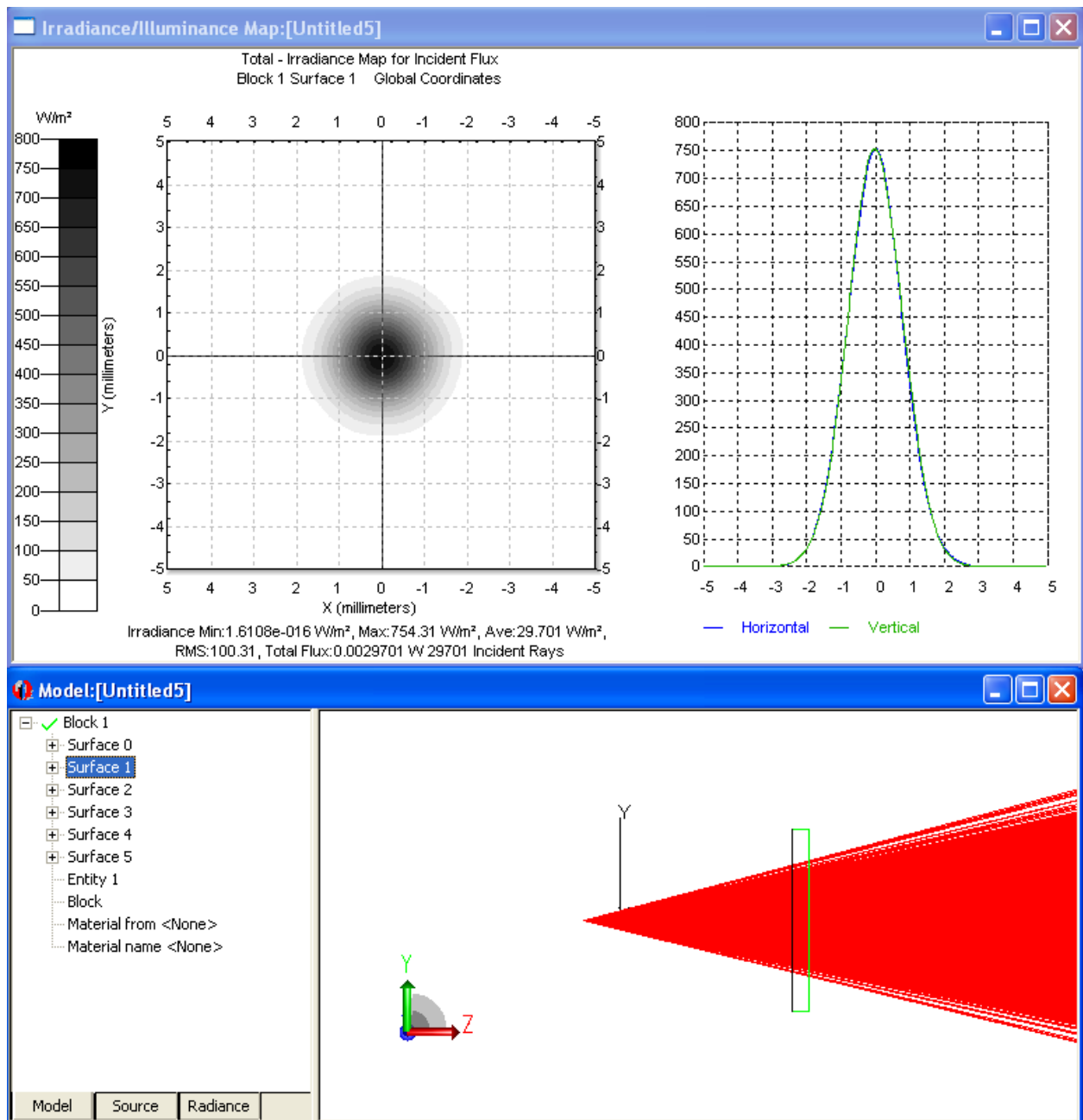


Fig. 75. TracePro: Distribution plot and raytrace of grid source with Nufern 460HP optical fiber characteristics. Block for distribution monitoring.

**Notes:** The power of a grid source depends both on the number of rays traced and the peak flux parameters, so as the number of rays is adjusted its necessary to adjust the peak flux to keep the desired output power.

The easiest way to monitor this and make adjustments is to place a block directly in front of the fiber which covers the beam completely. Making this a perfect absorber and tracing the source allows one to read the irradiance map total output power.

Use the check box next to this block in the model tree to remove it from the raytrace once a power and ray number is settled upon. See Fig. 76.

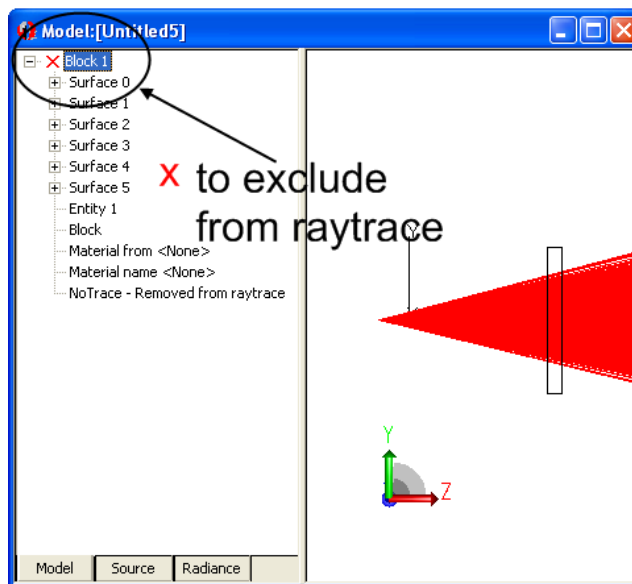


Fig. 76. TracePro: Grid source testing block.

#### 14.2.6. CMOS sensor chip

The sensor was modeled as a thin block. Dimensions are listed below:

Table 13. SI1280 CMOS sensor parameter table.

Characteristic	Value	Source
Width	6.83 mm	Manufacturer's Specification
Height	5.45 mm	Manufacturer's Specification

**Notes:** In actuality, the chip is behind a piece of glass of specific thickness. See appendix D. This is not modeled in the TracePro model, but proper modeling of this glass may provide insight into the appearance of secondary fringes from the angle of the reference beam.

## 15. Appendix C. Optical Characterization Details.

### 15.1. Resolution Algorithm

The code below can be directly put into MATLAB to perform the contrast trace of a resolution target to determine an optical system's resolution.

```
%% This file will let you determine the line-pairs/millimeter resolution of
% the optical system

clc; clear; close all;

% Input bitmap file type into imread function
Image = imread('Resolution_target.bmp');

% Image may be stored as color image, so each color is a repeat. This means
% you can strip off the extra layers of the array by allowing the command
% below to run. If the image is stored as a one dimensional array comment
% out the command below.
Image = Image(:,:,1:1);

% Show image and choose where to trace
% Left click to pick start point of trace and right click to pick end point
imshow(Image);
improfile

%% Determine resolution

% Region of interest
% Group being measured -
% Element being measured -

% What is minimum level:
dark = input('dark = ');

% What is maximum brightness at peak of area interest
peak = input('peak = ');

% What is minimum brightness in the valley of the area of interest
valley = input('valley = ');

% Contrast as a percent is:
contrast = (peak - valley)/(peak - dark)*100
```

## 15.2. Depth of Field Algorithm

The code below can be directly put into MATLAB to perform the contrast trace of depth of field target.

```
%% This file will let you determine dof of the optical system

clc; clear; close all;

Image = imread('Depth_of_field_image.bmp');

% Image may be stored as color image, so each color is a repeat. This means
% you can strip off the extra layers of the array by allowing the command
% below to run. If the image is stored as a one dimensional array comment
% out the command below.
Image = Image(:,:,1:1);

% Show image and choose where to trace
% Left click to pick start point of trace and right click to pick end point
imshow(Image)

% W will be a matrix of the gray scale variation along the trace. This
% matrix can be plotted. Depending on what the minimum contrast level
% to be considered in focus is, the depth of field can be determined.
W = improfile;
```

### 15.3. Image Aberration Algorithm

The code below can be directly put into MATLAB to determine the optical distortion function. Note that there are specific options that can be changed in this code depending on the image being analyzed..

```
%% Steps to evaluate optical distortions for grid target.
clc; clear; close all;

%% These steps create a matrix of the distorted positions

% The starting image must be cropped, so that only one column of dots is in
% the entire image.

%Define image as matrix
Image = imread('Dot_Grid.bmp');

% Image may be stored as color image, so each color is a repeat. This means
% you can strip off the extra layers of the array by allowing the command
% below to run. If the image is stored as a one dimensional array comment
% out the command below.
Image = Image(:,1:3);

%Determine appropriate gray scale threshold to determine what is white and
%what is black. You can either let MATLAB determine what it thinks should
%be the threshold by allowing the command below to run
graylevel = graythresh(Image);

%or you can specify the gray threshold by allowing the command below to
%run. It may be necessary to specify the gray threshold if the automatic
%command eliminates certain dots. Note: One "graylevel" command lines MUST
%be commented out.
graylevel = .30;

%Convert image to only black and white (1's and 0's in the matrix) with the
%appropriate grayscale threshold
BWImage = im2bw(Image,graylevel);

%Image may need to be inverted if dots are black and background is white.
%To invert image uncomment next line
%inv_BWImage = ~BWImage;

%fill holes in black/white image
filled=imfill(inv_BWImage,'holes');

%Each region must be assigned a different label so the correct number of
%centroids are calculated
labeled_Image = bwlabel(filled,8);
```

```

%Filtering out small areas is necessary to ensure that random specs that
%are not centroids are not labeled and used in the centroid calculation.
A = regionprops(labeled_Image,'Area');
%to adjust the minimum area change what [A.Area] must be greater than in
%the next line.
idx = find([A.Area] > 8);
BW_area_filtered = ismember(labeled_Image,idx);

%label image again after filtering
labeled_Image2 = bwlabel(BW_area_filtered,8);

%A structure is created with all of the centroids of the dot grid
struct = regionprops(labeled_Image2,'Centroid');

%Create a matrix with the centroid centers
M_Centroid_distort = cat(1,struct.Centroid);

%% These next steps create a matrix of the original positions

% The matrix of the centroid positions needs to be sorted in ascending
% order with respect to the vertical centroid coordinate while maintaining
% the horizontal and vertical correlation
Sorted_M_Centroid_distort = sortrows(M_Centroid_distort,2);

%Length of centroid matrix
Length_M_Centroid_distort = size(Sorted_M_Centroid_distort,1);

%It is assumed there is no distortion at the center of the principle axes.
%This step determines the point all the aberrations are centered around.
aberration_center = round(Length_M_Centroid_distort/2);

%If the actual distance between the centroids is unknown then you need a
%estimate the distance. Estimation is done by taking the average distance
%from the aberration center to the centroids immediately above and below
%it.

% Coordinates of centroids above and below aberration center
coordinate_above = Sorted_M_Centroid_distort(round(Length_M_Centroid_distort/2)-1,2);
coordinate_below = Sorted_M_Centroid_distort(round(Length_M_Centroid_distort/2)+1,2);

Distance = (coordinate_below-coordinate_above)/2;

%Build matrix of original centroid locations. This step only changes the
%vertical location and keeps the horizontal location from the distorted
%image.

%make an empty matrix for filling up
M_Centroid = zeros(Length_M_Centroid_distort,2);

i = 0;
while i < Length_M_Centroid_distort - aberration_center;
    j = i+1;

```

```

M_Centroid(aberration_center + j,2) = Sorted_M_Centroid_distort(aberration_center,2) + (Distance * j);
M_Centroid(aberration_center - i,2) = Sorted_M_Centroid_distort(aberration_center,2) - (Distance * i);
M_Centroid(aberration_center + j,1) = Sorted_M_Centroid_distort(aberration_center + i,1);
M_Centroid(aberration_center - i,1) = Sorted_M_Centroid_distort(aberration_center - i,1);
i = i+1;
end

%% Plot Centroids on original image

% This section can be uncommented to see what the distorted centroid
% locations look like plotted on the original image.

% imshow(Image)
% hold on
% plot(M_Centroid(:,1), M_Centroid(:,2), 'b*')
% hold off

%% Plot aberration

% Want to shift plot by coordinate of aberration center
aberration = Sorted_M_Centroid_distort(round(Length_M_Centroid_distort/2),2);

%make plot
plot(M_Centroid(:,2)-aberration,Sorted_M_Centroid_distort(:,2)-aberration, 'bo');

%% Polynomial fitting
%Choose polynomial order
order = 3;

p = polyfit(M_Centroid(:,2)-aberration,Sorted_M_Centroid_distort(:,2)-aberration,order);
f = polyval(p,M_Centroid(:,2)-aberration);
error=Sorted_M_Centroid_distort(:,2)-aberration-f;

%% Plot fitting results
hold on;
plot(M_Centroid(:,2)-aberration,f,'g', M_Centroid(:,2)-aberration, error,'r')
legend('centroids', 'Y_d_i_s_t_o_r_t_e_d(Y)', 'error')

xlabel('Undistorted Centroid Locations (Y)', 'FontSize',16)
ylabel('Distorted Centroid Locations (Y_d_i_s_t_o_r_t_e_d)', 'FontSize',16)

```

## **16. Appendix D. Component Specifications.**

**16.1: GRIN Lens**

**16.2: 5mm Diameter Imaging Lens**

**16.3: 6.35mm Diameter Imaging Lens**

**16.4: Beam Splitter**

**16.5: Patch Cable**

**16.6: si1280 Camera**

## 16.1. GRIN Lens<sup>2</sup>

### SRL-2.0-0.5-2000

LOT No 1253Y07-2C

The SRL is a combination of the ILW imaging lens, and a GRIN rod.

Optical Properties and Dimensions of: **SELFOC® Rod Lens (SRL)**

Diam.(mm)	Pitch	Dimensions (mm)				Optical Properties (@550 nm)
		SRL Length	ILW Length	W/D (ISL W/H)	Resolution	View Angle (2θ)
2.0± 8.05	0.5	50.41	6.54+/- 0.60	5	40.3 LP/mm (5·3)	52<_<58

- For all SRL, diameter tolerance for all SRL is +0/-0.05 mm, and refractive index on axis is 1.610 @ 550 nm.
- Material for cover glass is F-2 with refractive index of 1.62 @ 550 nm.
- Longitudinal chromatic aberration from C-line (656.3 nm) to F-line (486.1 nm) is approx. 0.23% per pitch for all SRL.

Optical Properties and Dimensions of: **SELFOC® Imaging Lens** (unpainted lens on end of GRIN rod)

Lens Type & Dia.(mm)	Lens Length Z (mm)	Resolution (LP/mm) center	Resolution (LP/mm) @0.8R	Typ. Chromatic Aberration (μm)	Typical √A (mm-1)	Magnif <sub>i</sub> at WD=5 mm	Field Curvature (μm)	View Angle (2θ)	Refract. Index (N <sub>0</sub> )
ILW-2.00	6.54 +/- 0.60	160	30	261	0.299	2.7	150	50° min.	1.643 on axis

Specification Notes:

- Standard working distance is 5 mm for all ILW and ILH.
- Diameter tolerance is +0/-0.05 mm for all ILW and ILH.
- Resolution is measured on a U.S. Air Force chart while a 100X microscope is focused on the back surface of the imaging lens (see Fig.). The chart is placed at 5 mm, the standard

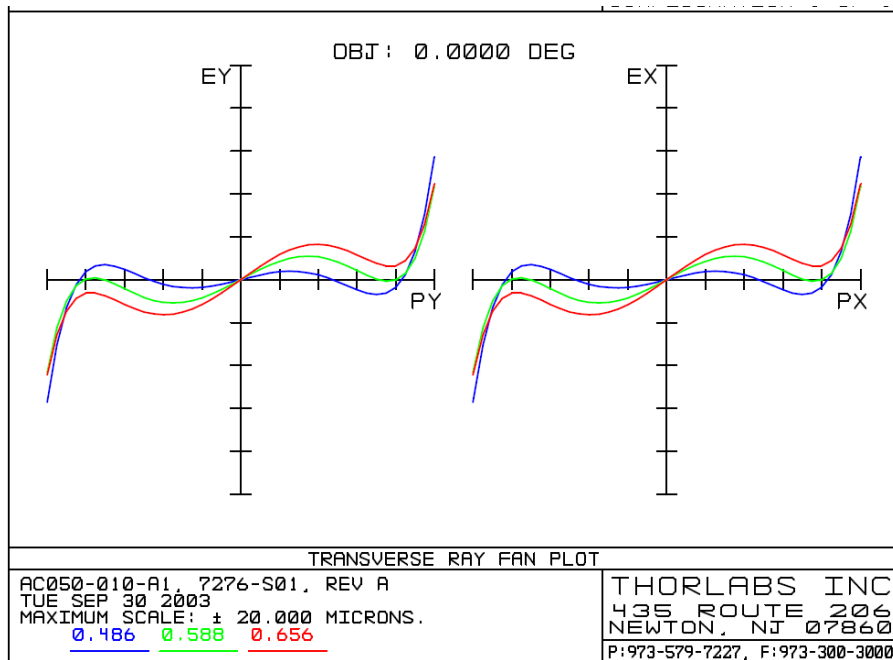
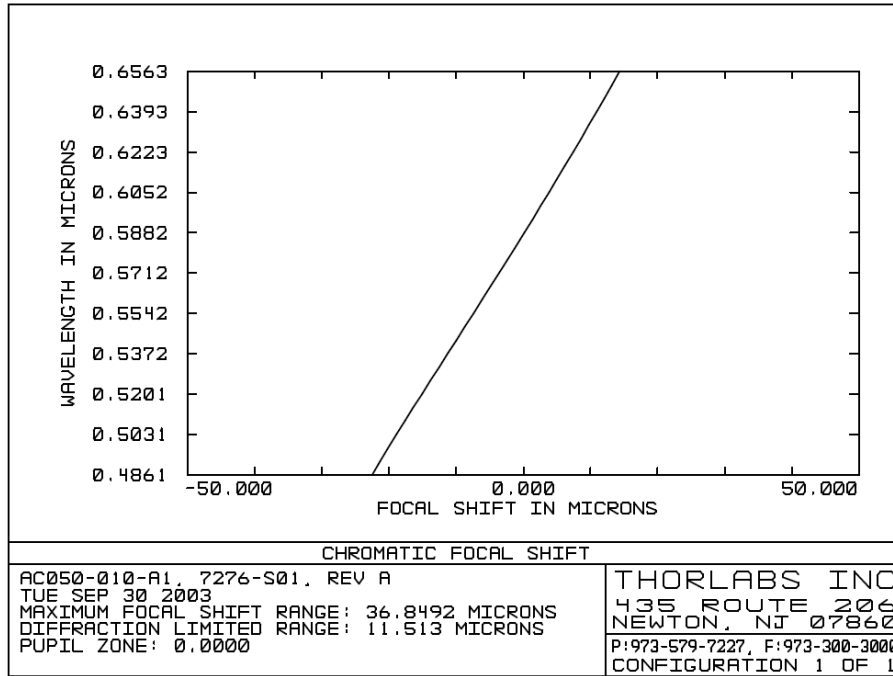
<sup>2</sup> NSG America. <http://www.nsgamerica.com/>. February 2009.

working distance, away from the lens. Resolution is measured at both lens center and 80% of the lens radius and normalized by the magnification factor.

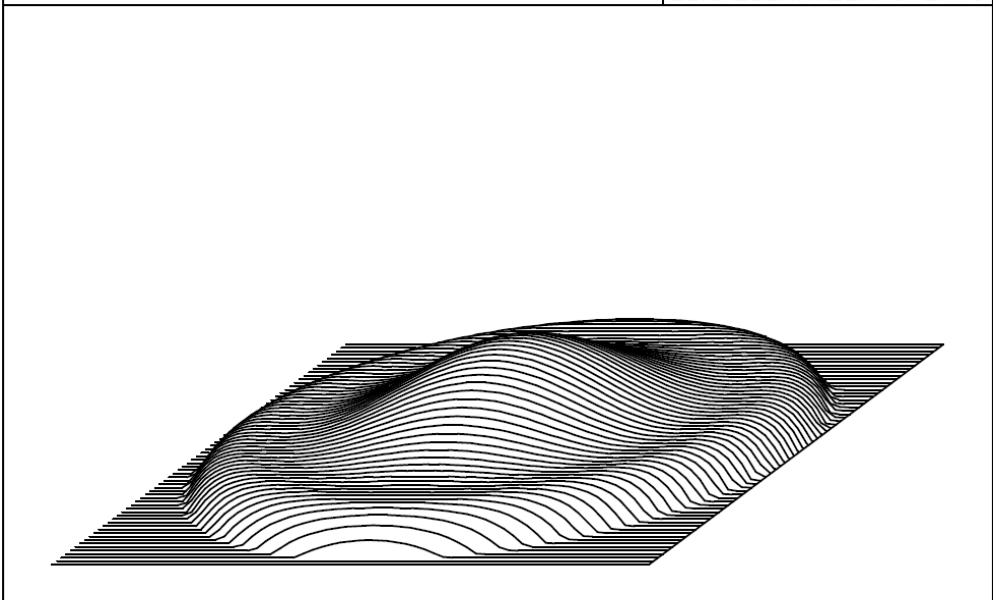
- Field curvature is the difference in focal positions between the lens center and at 80% of the lens radius.
- End surface is inspected at 20X magnification. No chips and cracks are allowed within 90% of the lens radius.
- Material Toxicity: This product contains components which might be toxic. The user is advised to pay special attention to such toxicity when using this product in medical devices for people or animals.
- Storage
- For extended periods of time, the lenses should be stored in a "dry box" environment. This entails the use of a desiccant (e.g., silica gel) or a heat source to prevent humidity from leaching the lens material. This is much more critical for non-coated lenses, since AR coatings help to protect the lens surfaces from humidity. For short term storage (less than a month), the plastic box and foam packing in which the lenses are shipped will provide adequate storage.
- In addition to humidity requirement, the lenses need to have sufficient spacing to avoid potential damage such as chipping and scratching from other lenses. For this reason, NSG storage boxes have built-in slots in which the lenses are placed, with surrounding packaging to hold them securely in place.
- Handling: After opening the lens boxes, it is important to exercise extra care in lifting the plastic shield. Particularly with smaller lenses, it is possible that they may cling to the shield and be lost during removal. Lenses should be handled with stainless steel tweezers, preferably those with a tapered end. Lenses should be picked up out of their individual compartments by firmly holding each by its side surface (not the ends).
- Cleaning: At times it is necessary to clean the lens surfaces due to the presence of some dust or film which may impair the image. NSG generally recommends the use of methyl alcohol as a cleaning solvent. Acetone may also be used, without harm to the lens, but it should be pure enough to no leave a residue on the lens' surface.

## 16.2. 5mm Diameter Imaging Lens<sup>3</sup>

AC050-010-A1 -  $f = 10.0$  mm,  $\varnothing 5$  mm Unmounted Visible Achromat, ARC: 400-700 nm



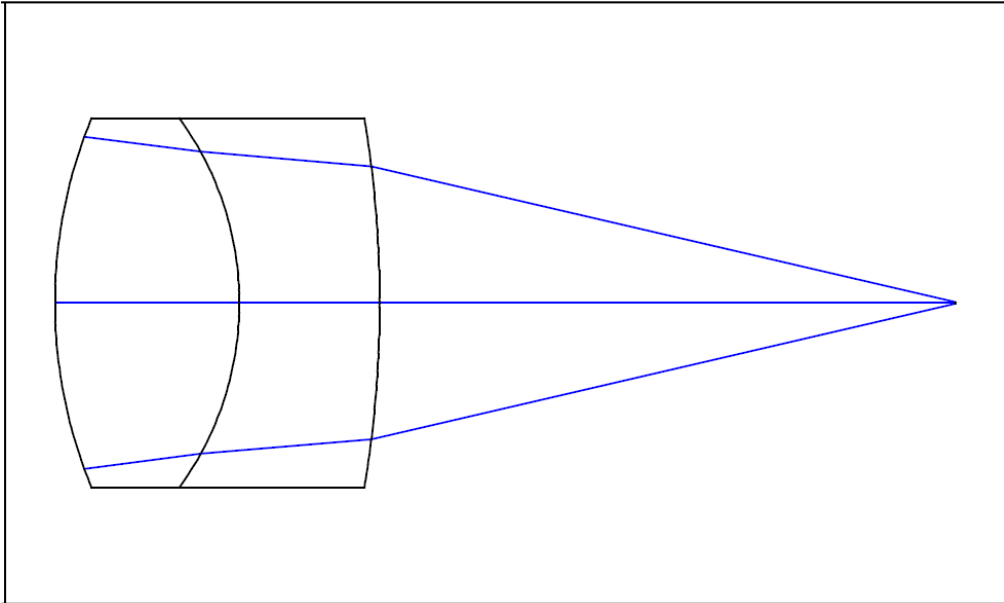
<sup>3</sup> Thorlabs. <http://www.thorlabs.com/thorProduct.cfm?partNumber=AC050-010-A1>. April 2009.



WAVEFRONT FUNCTION

AC050-010-A1, 7276-S01, REV A  
 TUE SEP 30 2003  
 0.5876 MICRONS AT 0.0000 DEG.  
 PEAK TO VALLEY IS 0.5768 WAVES.

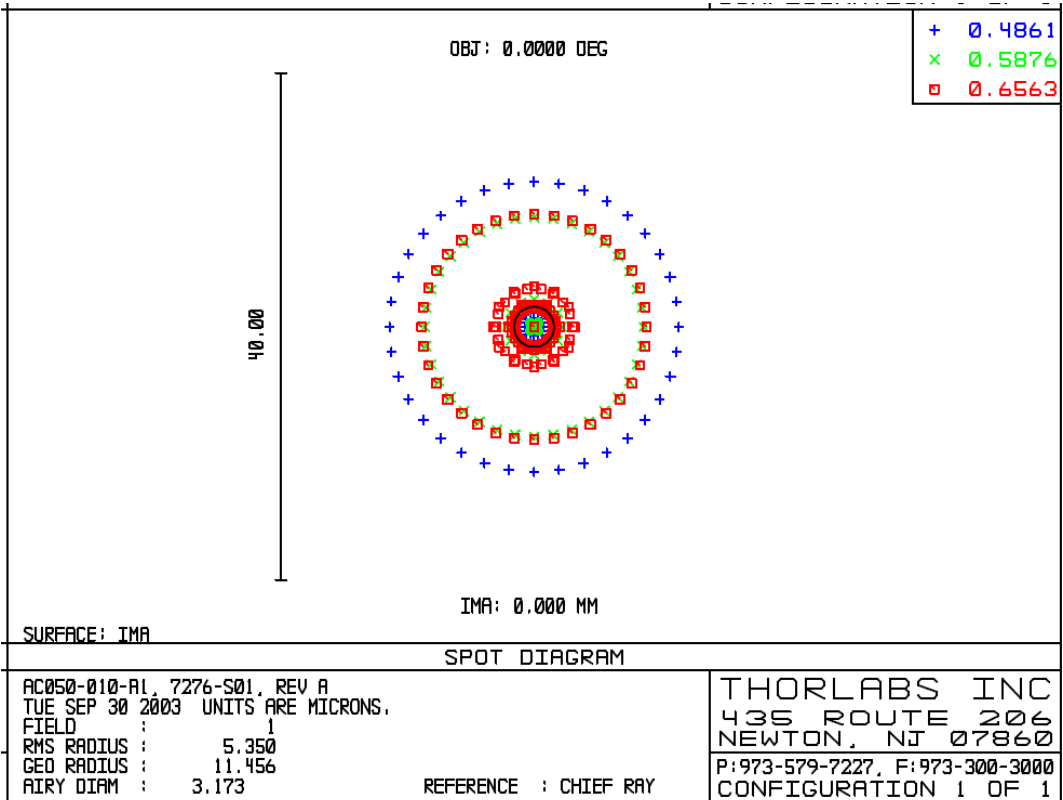
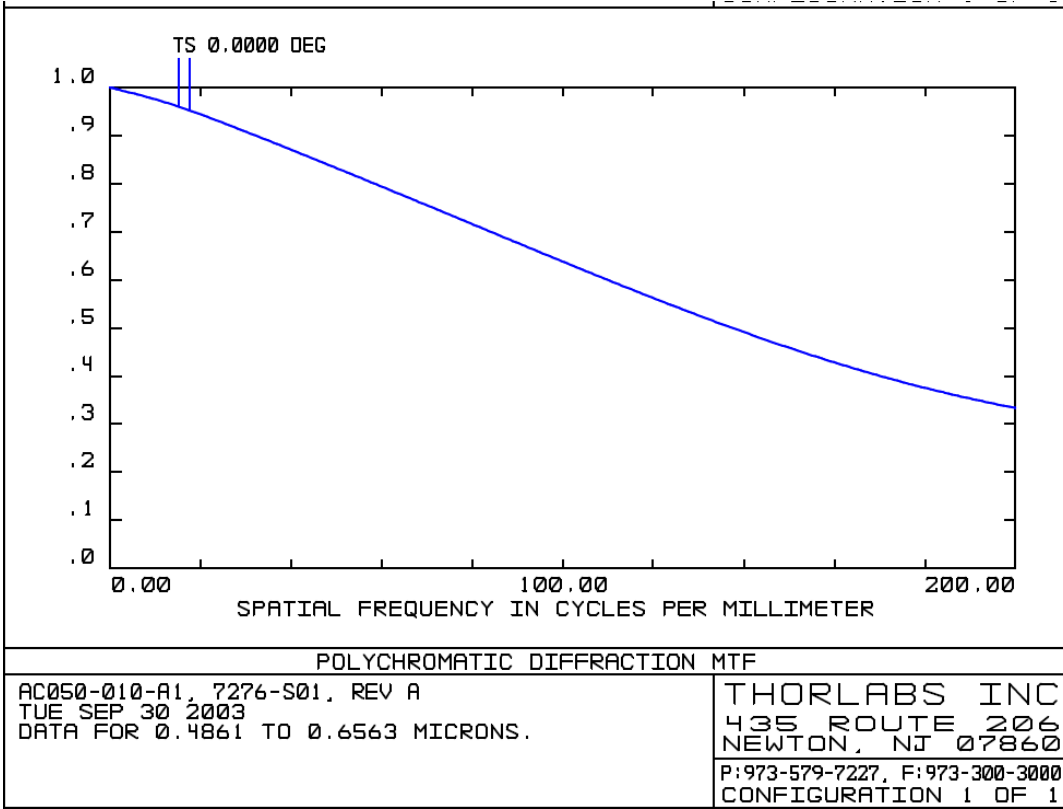
THORLABS INC  
 435 ROUTE 206  
 NEWTON, NJ 07860  
 P:973-579-7227, F:973-300-3000  
 CONFIGURATION 1 OF 1

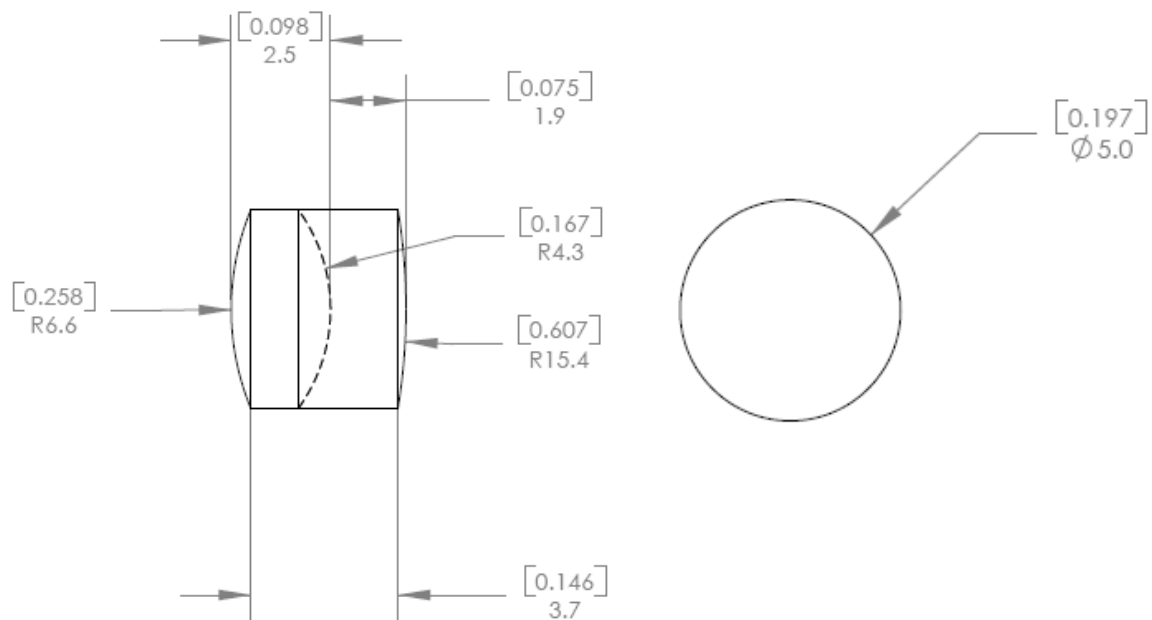


LAYOUT

AC050-010-A1, 7276-S01, REV A  
 TUE SEP 30 2003  
 TOTAL LENGTH: 12.21281 MM

THORLABS INC  
 435 ROUTE 206  
 NEWTON, NJ 07860  
 P:973-579-7227, F:973-300-3000  
 CONFIGURATION 1 OF 1





FOCAL LENGTH: 10.0mm  
 BACK FOCAL LENGTH: 7.9mm  
 FOCAL LENGTH TOLERANCE:  $\pm 1\%$   
 COATING: (A1) 400nm-700nm RAVG<0.5%  
 DESIGN WAVELENGTH: 486.1nm 587.6nm 656.3nm  
 DIAMETER TOLERANCE: +0.00/-0.10mm  
 SCRATCH/DIG: 40/20  
 CENTRATION:  $\leq 3$  ARCMIN  
 CLEAR APERTURE: > 90% OF DIAMETER  
 OPERATING TEMPERATURE: -40°C TO 85°C

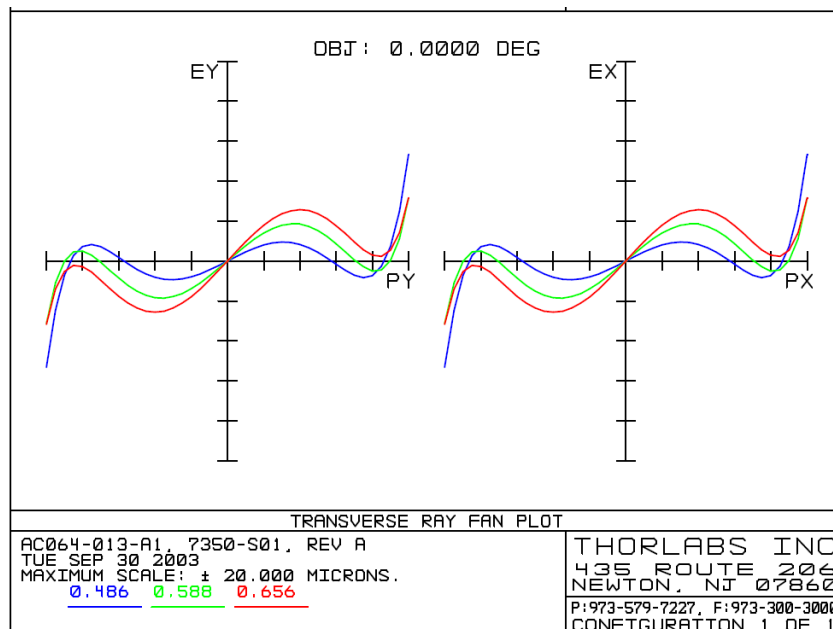
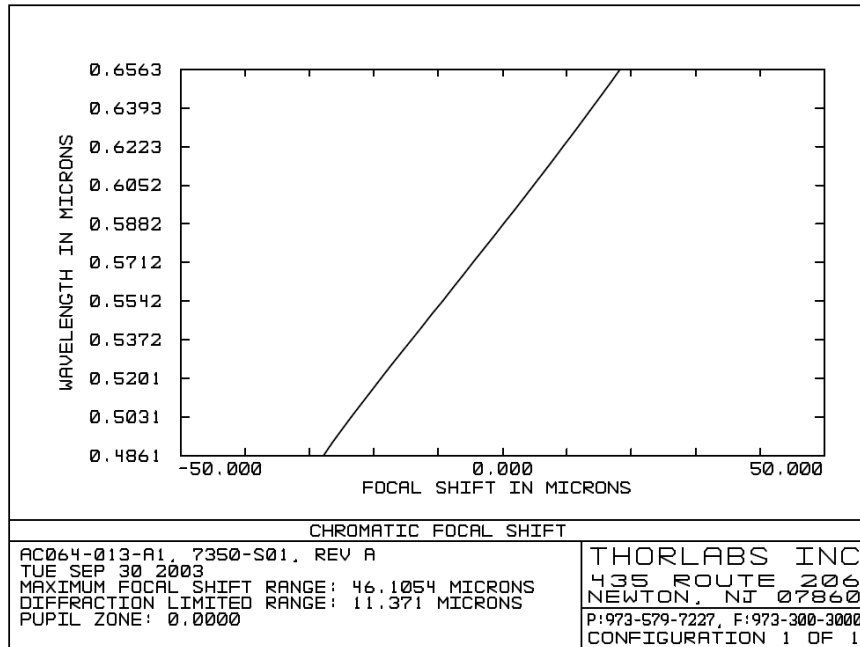
\*NOTE: ALL DEMENSIONS IN MILLIMETERS

TOLERANCES		NAME	DATE
UNLESS OTHERWISE SPECIFIED:		DRAWN	BAG 05/23/2006
<b>DIMENSIONS ARE IN INCHES</b>		ENG APPR.	TO 05/23/2006
<b>LINEAR TOLERANCES:</b>		MFG APPR.	TO 05/23/2006
TWO PLACE DECIMAL: $\pm 0.010$		<b>PROPRIETARY AND CONFIDENTIAL</b>	
THREE PLACE DECIMAL: $\pm 0.005$		THE INFORMATION CONTAINED IN THIS	
ANGULAR: $\pm 30'$		DRAWING IS THE SOLE PROPERTY OF	
SURFACE FINISH: 32 MICRINCHES		THORLABS, INC. ANY REPRODUCTION	
PARALLELISM: 0.002		IN PART OR AS A WHOLE WITHOUT	
FLATNESS: 0.002		THE WRITTEN PERMISSION OF	
STRAIGHTNESS: 0.002		THORLABS, INC. IS PROHIBITED.	
CONCENTRICITY: 0.002			
PERPENDICULARITY: 0.002			
THREAD: CLASS 2 FIT			

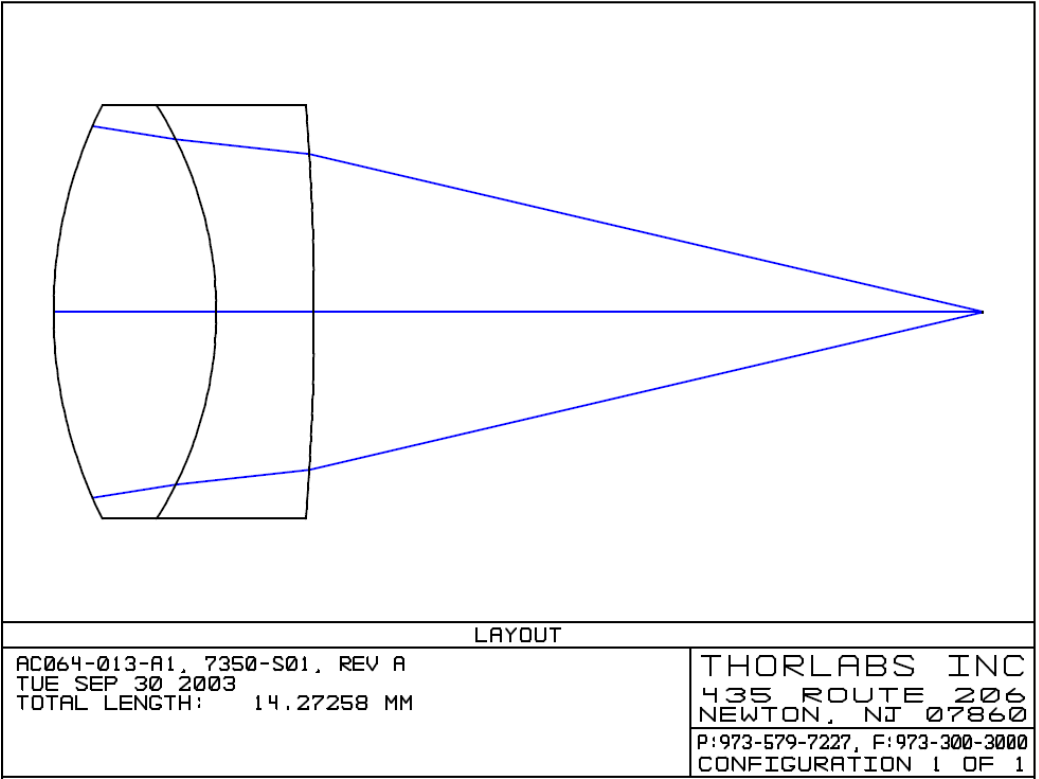
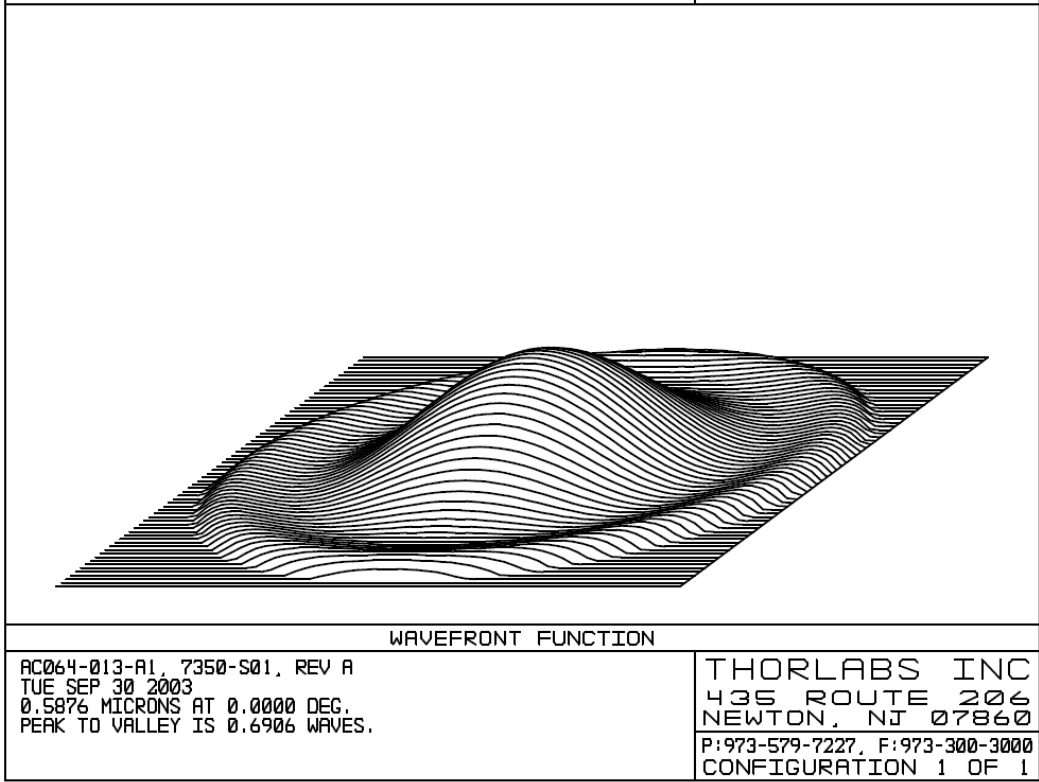
<b>THORLABS INC.</b>		PO BOX 366 NEWTON NJ	
TITLE: ACHROMATIC DOUBLET D=5.0mm, F=10.0mm			
MATERIAL: BAK4 - SF5		SIZE A	REV. A
SCALE: 5:1		SHEET 1 OF 1	
DWG. NO. 7276-E01	PART NO. AC050-010-A1		

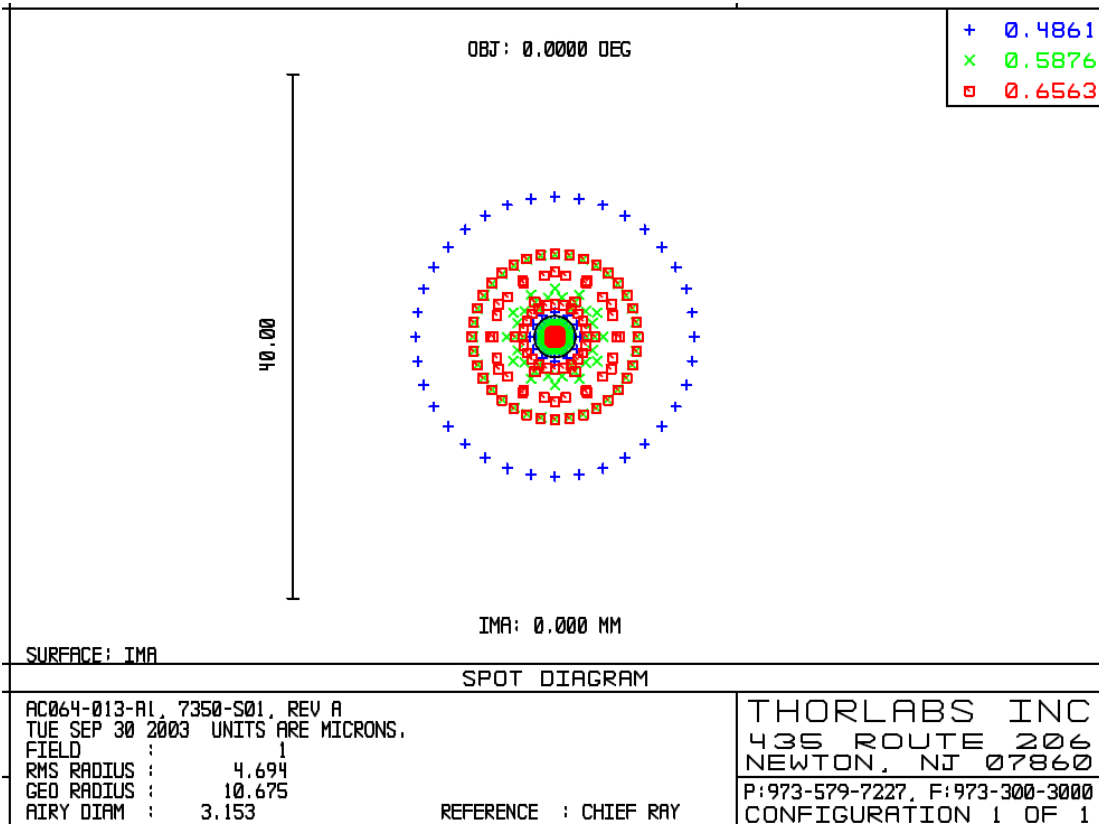
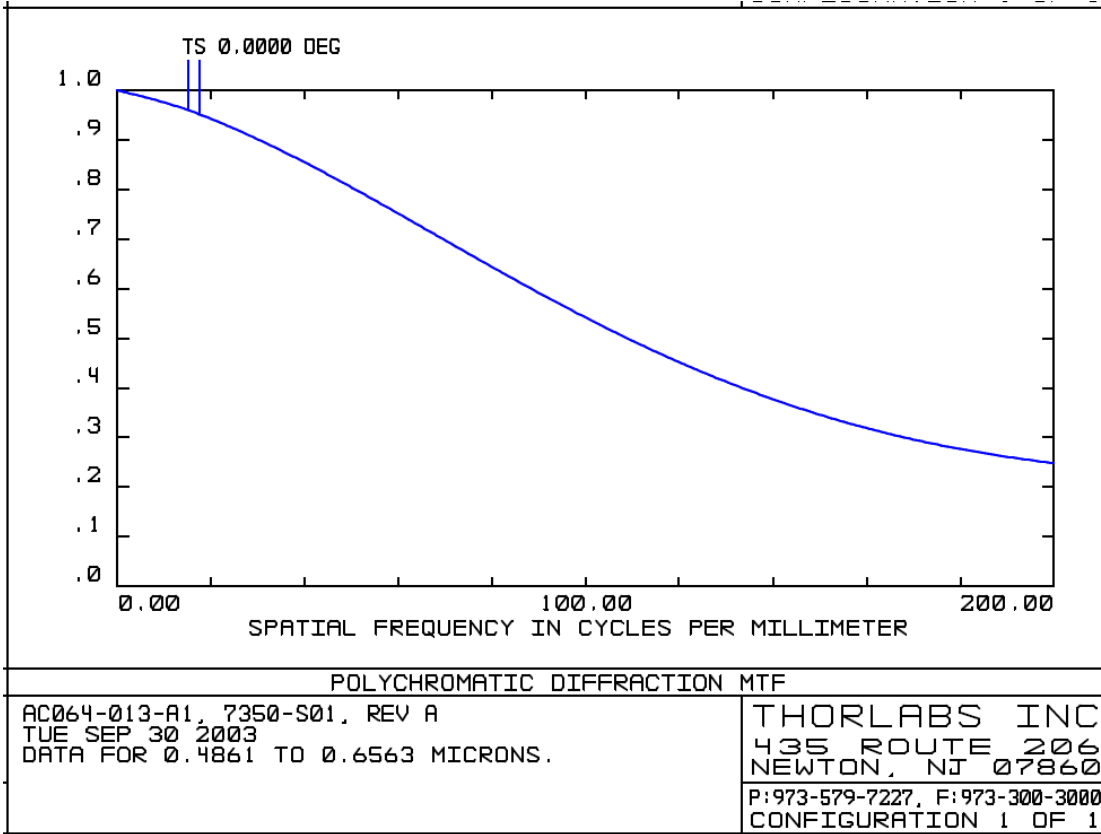
### 16.3. 6.35mm Diameter Imaging Lens<sup>4</sup>

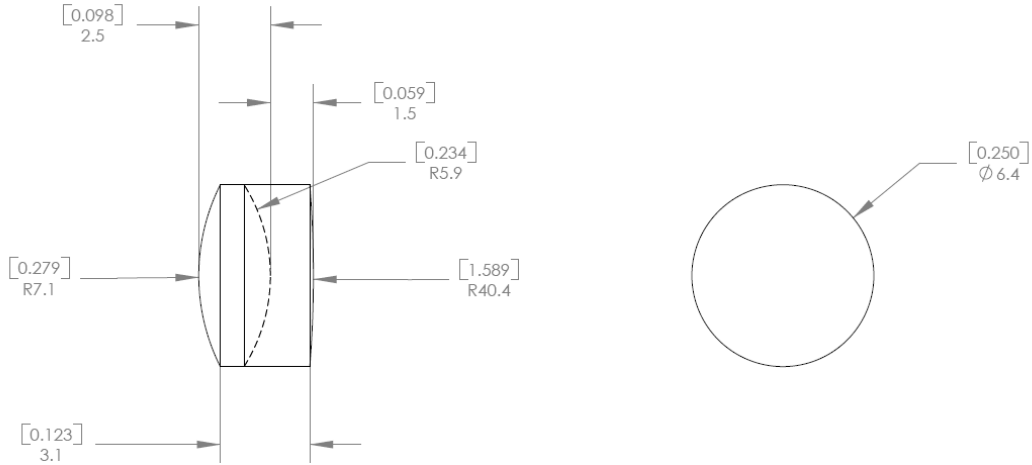
AC064-013-A1 - f = 12.7 mm, Ø6.35 mm Unmounted Visible Achromat, ARC: 400-700 nm



<sup>4</sup> Thorlabs. <http://www.thorlabs.com/thorProduct.cfm?partNumber=AC064-013-A1>. April 2009.







FOCAL LENGTH: 12.7mm  
 BACK FOCAL LENGTH: 10.3mm  
 FOCAL LENGTH TOLERANCE:  $\pm 1\%$   
 COATING: (A1) 400nm-700nm RAVG<0.5%  
 DESIGN WAVELENGTH: 486.1nm 587.6nm 656.3nm  
 DIAMETER TOLERANCE: +0.00/-0.10mm  
 SCRATCH/DIG: 40/20  
 CENTRATION:  $\leq 3$  ARCMIN  
 CLEAR APERTURE:  $> 90\%$  OF DIAMETER  
 OPERATING TEMPERATURE: -40°C TO 85°C

\*NOTE: ALL DEMENSIONS IN MILLIMETERS

TOLERANCES		NAME	DATE
UNLESS OTHERWISE SPECIFIED:		DRAWN	BAG 05/23/2006
DIMENSIONS ARE IN INCHES		ENG APPR.	TO 05/23/2006
LINEAR TOLERANCES:		MFG APPR.	TO 05/23/2006
TWO PLACE DECIMAL: $\pm 0.010$		<b>PROPRIETARY AND CONFIDENTIAL</b> THE INFORMATION CONTAINED IN THIS DRAWING IS THE SOLE PROPERTY OF THORLABS, INC. ANY REPRODUCTION IN PART OR AS A WHOLE WITHOUT THE WRITTEN PERMISSION OF THORLABS, INC. IS PROHIBITED.	
THREE PLACE DECIMAL: $\pm 0.005$			
ANGULAR: $\pm 30'$			
SURFACE FINISH: 32 MICRINCHES			
PARALLELISM: 0.002			
FLATNESS: 0.002			
STRAIGHTNESS: 0.002			
CONCENTRICITY: 0.002			
PERPENDICULARITY: 0.002			
THREAD: CLASS 2 FIT			

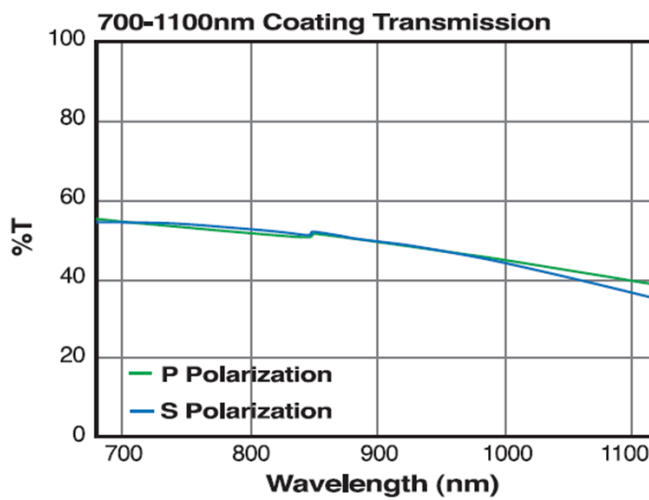
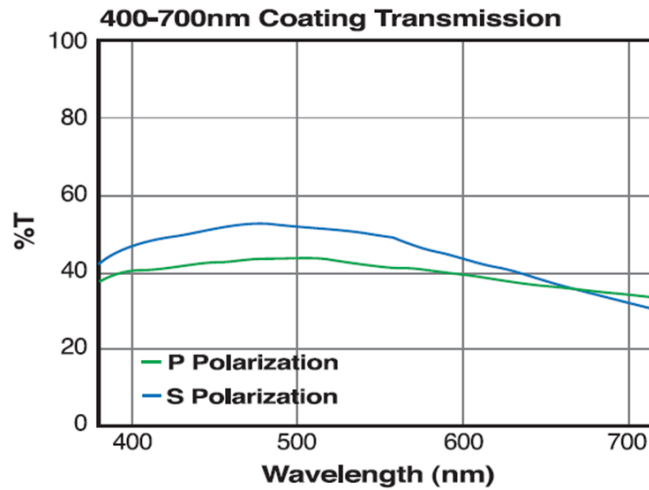
<b>THORLABS INC.</b>		PO BOX 366 NEWTON NJ	
TITLE: ACHROMATIC DOUBLET, D=6.35mm, F=12.7mm			
MATERIAL: BAK4 - SF5		SIZE A	REV. A
SCALE: 5:1		SHEET 1 OF 1	
DWG. NO. 7350-E01	PART NO. AC064-013-A1		

## 16.4. Beam Splitter<sup>5</sup>

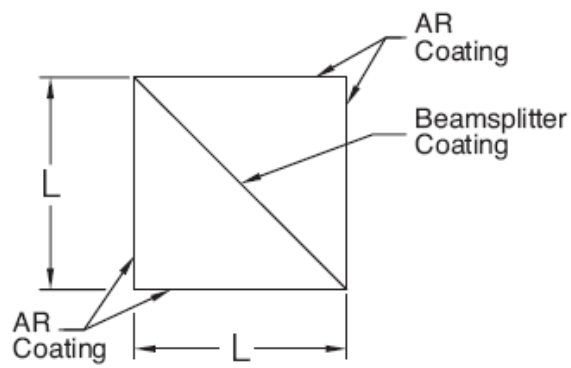
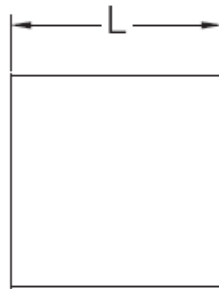
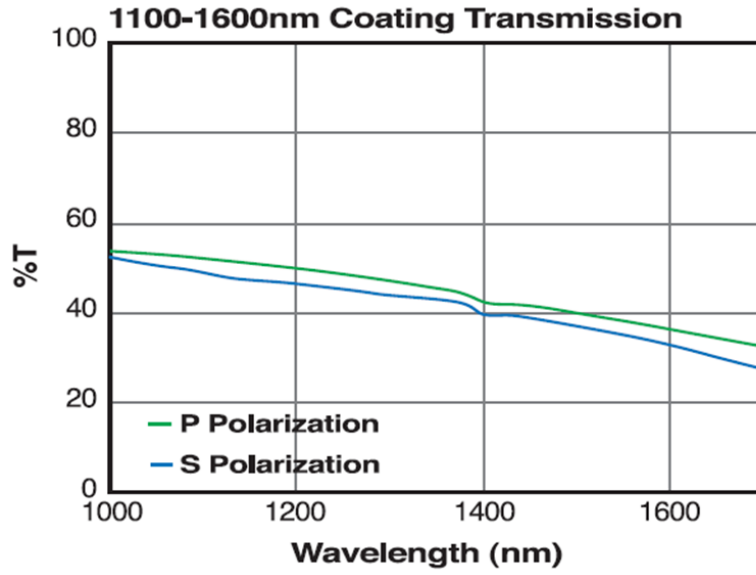
### BS013 - 400-700 nm Broadband Non-Polarizing Beamsplitter Cube, 25.4 mm

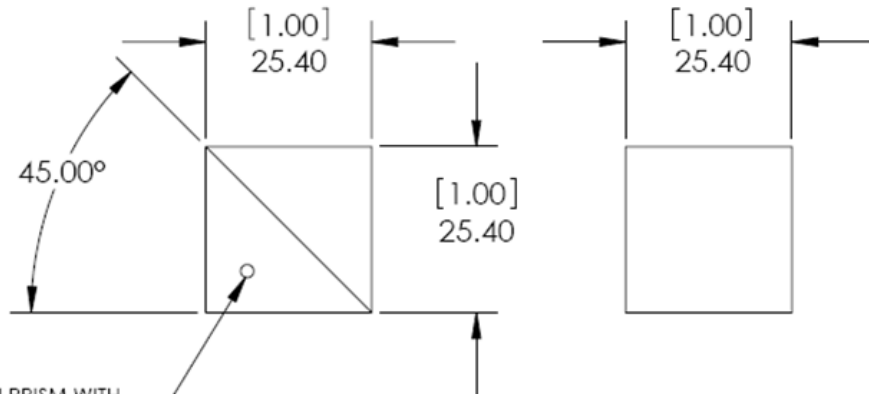
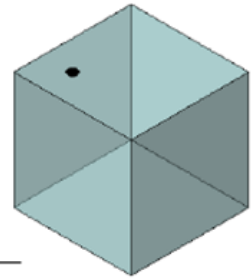
#### Specifications

- Material: BK7 - Grade A
- Flatness:  $\lambda/10$  Over 90% on All Optical Surfaces at 635nm
- Max Transmitted Beam Deviation:  $<5$ arcmin
- Reflected Beam Deviation:  $90^\circ \pm 5$ arcmin
- Splitter Ratio Tolerance:  $<15\%$  Over Entire Wavelength Range  $|T_s - T_p| < 15\%$  and  $|R_s - R_p| < 15\%$
- Clear Aperture:  $>80\%$  of Central Diameter
- Durability: MIL-M-13508C, MIL-C-675C, MIL-C-14806
- Surface Quality: 40/20 Scratch/Dig
- Broadband AR Coating: All 4 Input/Output Faces
- Wavelength Range: See Plots and Description



<sup>5</sup> Thorlabs. <http://www.thorlabs.com/thorProduct.cfm?partNumber=BS013>. April 2009.





DOT PLACED ON PRISM WITH COATED SURFACE INDICATING RECOMMENDED ENTRANCE FACES

SPECIFICATIONS:  
 WAVELENGTH RANGE: 400nm-700nm  
 CLEAR APERTURE: >80% OF DIMENSION  
 SURFACE FLATNESS:  $\lambda/10$  AT 633nm  
 WAVEFRONT DISTORTION:  $<\lambda/4$  AT 633nm  
 SURFACE QUALITY: 40-20 SCRATCH-DIG  
 DIMENSION TOLERANCE: +0.0/-0.2  
 SPLITTER RATIO: 50:50  
 TRANSMITTED BEAM DEVIATION:  $<5$  arcmin  
 REFLECTED BEAM DEVIATION:  $90^\circ \pm 5$  arcmin  
 SPLITTER RATIO TOLERANCE:  $<15\%$  OVER ENTIRE WAVELENGTH RANGE  $|T_p - T_s| < 15\%$  AND  $|T_p - T_s| < 15\%$   
 COATING (ALL 4 OUTER OPTICAL SURFACES):  
 BBAR COATING  $R_{avg} < 0.5\%$  at  $0^\circ$  AOI

DIMENSIONS IN [in]  
mm

NOTE:  
 FOR INFORMATIONAL PURPOSES ONLY.  
 NOT FOR MANUFACTURING.

	NAME	DATE
DRAWN	AP	04/20/06
ENG APPR.	DJ	01/16/09
MFG APPR.	PM	02/06/09

PROPRIETARY AND CONFIDENTIAL  
 THE INFORMATION CONTAINED IN THIS DRAWING IS THE SOLE PROPERTY OF THORLABS, INC. ANY REPRODUCTION IN PART OR AS A WHOLE WITHOUT THE WRITTEN PERMISSION OF THORLABS, INC. IS PROHIBITED.

THORLABS INC. PO BOX 366 NEWTON NJ	
TITLE: 25.4mm NON-POLARIZING 50:50 BEAMSPLITTER CUBE 400-700nm	
MATERIAL: BK7 GRADE A	SIZE A
SCALE: 1:1	REV. B
DWG. NO. 3618-E01	PART NO. BS013
SHEET 1 OF 1	

## 16.5. Patch Cable<sup>6</sup>

### P1-460A-FC-2 - Single Mode Fiber Patch Cable, 2m, 450-600nm, FC/PC

#### Features

- Connectorized on Both Ends
- Typical Return Loss of 50dB (40dB min.)
- Ceramic Radiused Ferrules (PC)
- 2, 5, and 10 Meter Lengths
- Ø3mm Protective Outer Jacket

#### 488/514nm FC Single Mode Patch Cables<sup>1</sup>

ITEM#	CUTOFF WAVELENGTH	L	FIBER (see page 1060)	MFD <sup>2</sup> /CLAD	NA <sup>3</sup>
P1-460A-FC-2	410-450nm <sup>1</sup>	2m	460HP	3.3/125µm	0.13
P1-460A-FC-5	410-450nm <sup>1</sup>	5m	460HP	3.3/125µm	0.13

1) Operating wavelength: 450-600nm.      3) Nominal NA

2) MFD: mode field diameter (@ 515nm)

### 460HP - Single Mode Optical Fiber, 450-600 nm

Source: <http://www.thorlabs.com/thorProduct.cfm?partNumber=460HP>

ITEM#	OPERATING WAVELENGTH	MODE FIELD DIAMETER	CLADDING	COATING	CUTOFF WAVELENGTH	ATTENUATION MAXIMUM	NA	VENDOR
460HP <sup>5</sup>	450-600 nm	3.5 ± 0.5 µm @ 515 nm	125 ± 1.5 µm	245 ± 15 µm	430 ± 20 nm	<30dB/km @ 630 nm	0.13	Nufern

1) Operating wavelength range is typically 200 nm above the cutoff wavelength.

2) MFD is a nominal, calculated value, estimated at the operating wavelength(s)

3) 0.10 ≤ NA ≤ 0.14

4) Pure Silica Core Fibers

5) Short term bend radius ≥ 6 mm

<sup>6</sup> Thorlabs. <http://www.thorlabs.com/thorProduct.cfm?partNumber=P1-460A-FC-2>. April 2009.

<b>Optical Specifications</b>	<b>460-HP</b>
Operating Wavelength (nominal)	450 – 600 nm
Mode Field Diameter (1/e <sup>2</sup> fit - near field)	3.5 ± 0.5 μm @ 515 nm
Second Mode Cutoff	430 ± 20 nm
Attenuation	30 dB/km @ 515 nm (nominal)
Numerical Aperture (nominal)	0.13
Bend Loss for 100 turns @ LTBR (nominal)	<0.001 dB @ 460 nm
Bend Radius for 0.05 dB per 100 turns (nominal)	Much less than LTBR @ 460 nm
<b>Geometrical &amp; Mechanical Specifications</b>	
Clad Diameter	125.0 ± 1.5 μm
Coating Diameter	245 ± 15 μm
Core-Clad Concentricity	< 0.5 μm
Coating/Clad Offset	≤ 5 μm
Coating Material	UV Cured, Dual Acrylate
Operating Temperature	- 55 to + 85°C
Short-Term Bend Radius	≥ 6 mm
Long-Term Bend Radius	≥ 13 mm
Proof Test Level	≥ 200 kpsi (1.4 GN/m <sup>2</sup> )

## 16.6. si1280 Camera<sup>7</sup>

### Sensor:

Active Pixels	1280 (H) x 1024 (V)
Optical Imaging Format	2/3" (8.576mm X 6.861mm)
Pixel Size (pitch)	6.7um x 6.7um
Pixel Type	CMOS
Aspect Ratio	1 : 1
Spectral Response	400 ~ 1000 nm
FPN (on chip corrected)	<0.5%
PRNU	10%p/p; 1.1%RMS
Conversion Gain	12 mV/electron
Sensitivity	1.85V/Lux.sec (visible) or 336 V.m2WV.s
Fill Factor	~55%
Read Noise	80-90 e <sup>-</sup> (sync shutter); 70-80 e <sup>-</sup> (rolling)
Dark Current	2100 pA/cm <sup>2</sup> at RT or 5900 e <sup>-</sup> /s
Saturation Charge	120,000 e <sup>-</sup>
Windowing (ROI)	Programmable row/column
Sub-sampling	1:2 for color and monochrome
Noise Reduction	Correlated Double Sampling (CDS)
Readout Method	Progressive Scan
Readout Types	Destructive
Shutter	Full Frame Shutter or Rolling Shutter
Shutter Speed / Integration	Variable, 1 to 1280 Line times
Minimum Blanking	150 Clocks/line

### A/D Conversion & Sampling Clock Synthesizer

A/D Conversion	30MHz (Nominal), 60MHz (max)
Vertical Resolution	12 Bit
Pixel Clock Frequency	20 ~ 60MHz Programmable
Adjustment Method	Serial command Protocol
A/D SNR	67.5dB
Output Noise	0.2 LSB rms

### Digital Video Output

Readout Rate	60 MHz Maximum, PCI 8 bit @ 60MHz, PCI 12 bit @ 50MHz; PCI-X @ 60MHz USB @ 45MHz		
Readout Format	CL-12 Bit (Ports A, B)		
Frame Rate @ Max Clock	USB 8 bit	PCI-CL(12)	PCI-X - CL(12) And PCI-CL(8)
1280 x 1024	24	34	41
1280 x 720	36	48	58
768 x 768	45	70	85
640 x 512	75	123	148
512 x 512	85	147	177
360 x 300	150	326	392
320 x 240	180	443	532
256 x 256	190	481	577
64 x 64	375	3650	4380
Line Readout Rate	23.9 usec per line @ 55MHz		
Signal-to-Noise	> 60dB (fc=20MHz, Gains=1.0)		
Connector	MDR 26-pin (3M 10226-6212VC) (-CL) USB 2.0 Integrated cable (-U)		

### CameraLink Frame Grabber Control:

Serial Communication	RS-232 Protocol 9600bps
Signaling	TX & RX (LVDS)
Asynchronous Triggers	LVDS – CC1, 2, 3, 4 (-CL) TTL Trigger-In & Strobe-Out (-U)
High Speed Shutter	1usec ~ 4sec, in 1usec increments
Trigger-to-Exposure	128 clocks (3.2usec @40MHz)
Long Integration	n-Frame Times
Region-of-Interest	Programmable Horiz & Vertical
Gain & Offset	7 Settings (1.0x, 1.33x, 2.0x, 4x)
Programmable Modes	Full-Frame, Window, Subsampling Long Integration & Single-Shot
Setting Timing	Next top of Frame
Ext Clock Sync	Clock in or Clock Out (-X Option)

### Power

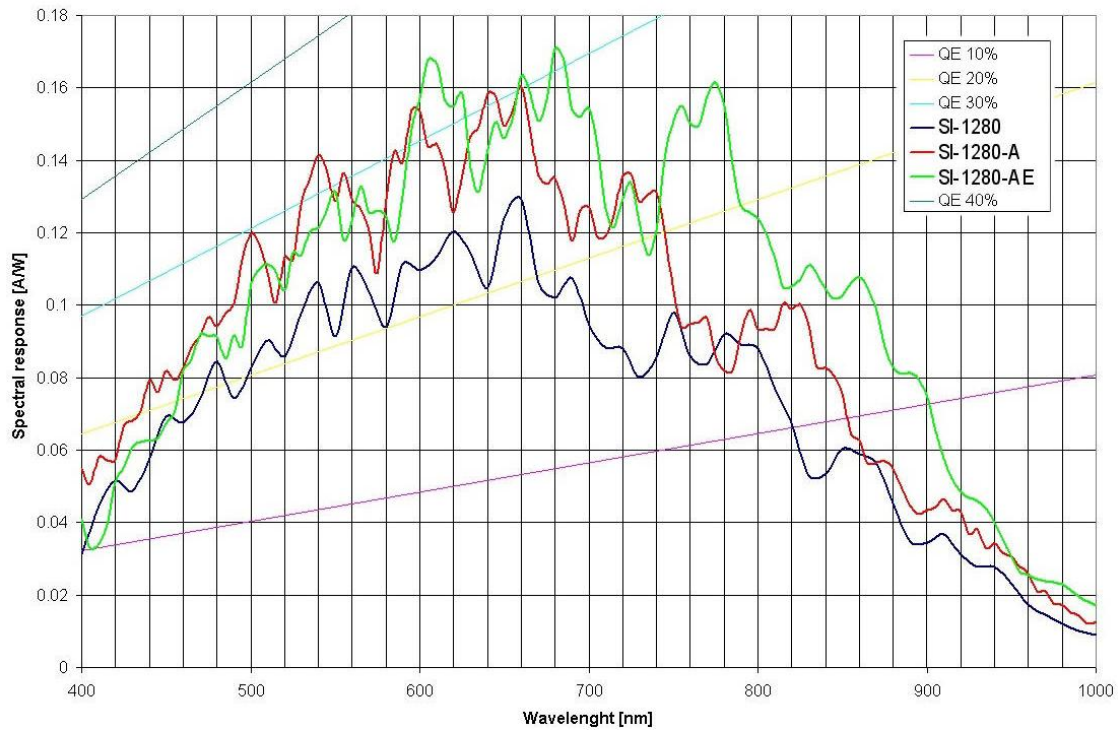
Input Voltage	+5 VDC +/- 10%
Power	2.5 Watts
Power/Trigger Connection	Tajimi RO3-PB3M 3Pin (-CL) Tajimi RO3-PB5M 5Pin (-X)

### Mechanical

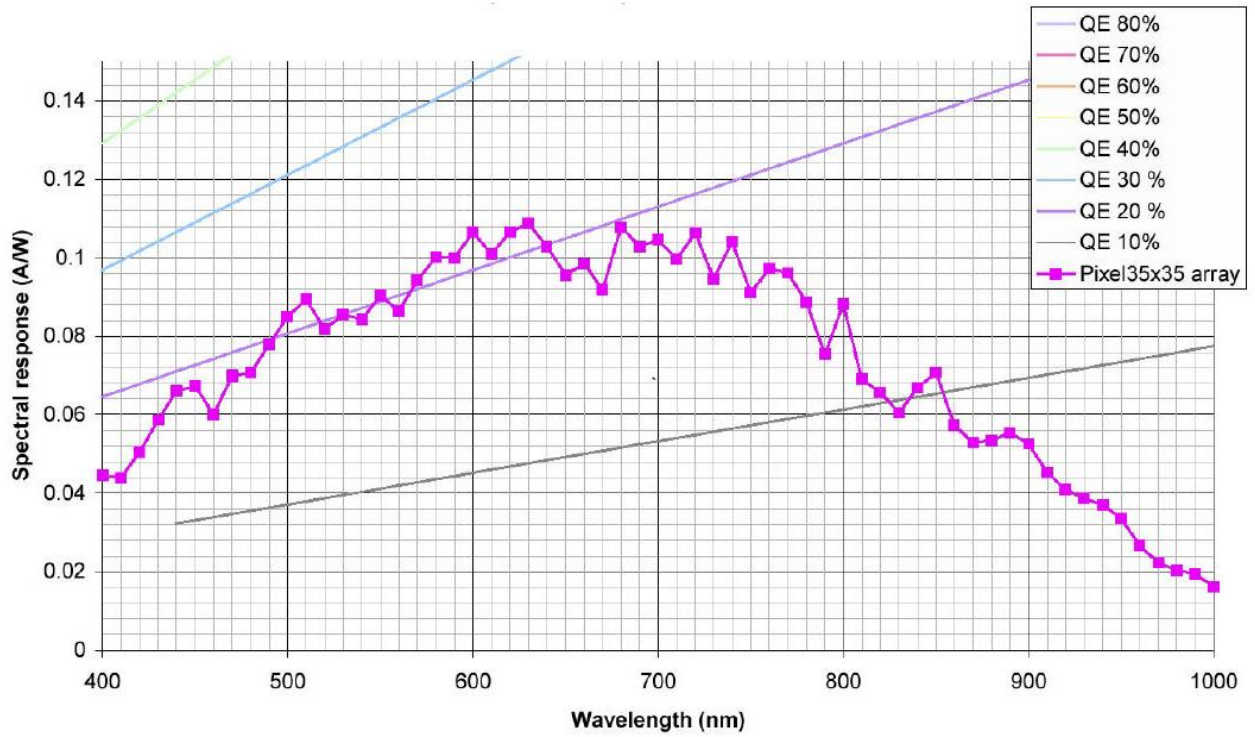
Lens Mount	C-Mount, 7mm Back focus Adj.
Enclosure Size	45mm W x 52mm H x 50mm L
Weight	12 oz.
Camera Mount	1/4" x 20standard tripod mount
Cable Connector	CameraLink MDR-26 (-CL) High-Speed 3-meter USB Cable with Type-A Connector (-U)

<sup>7</sup> Silicon Imaging. <http://www.siliconimaging.com/SI-1280CL%20spec.htm>. April 2009.

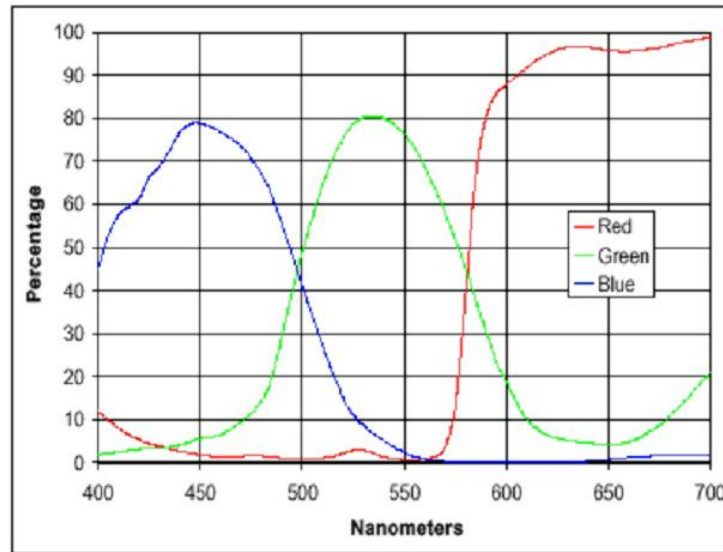
SI-1280 Spectral Response Curve



SI-6600 Spectral Response Curve



### SI-3170 Spectral Response Curve



### SI-1280F CameraLink Frame Rates

The SI-1280F has a Digital Clock Synthesizer capable of generating a range of frequencies from 20MHz to 60MHz. The pixel data output rate is the same as the sampling clock rate. A range of preset frequencies are listed below. There are 150 clocks overhead per row for readout

MHz	SI-1280F Frame Rate							
	1280x1024	1280 x 700	800 x 600	640x480	320x200	240x180	200 x 150	128x128
20 MHz	14	20	35	53	177	285	381	562
25 MHz	17	25	44	66	222	356	476	703
30 MHz	20	30	53	79	266	427	571	843
35 MHz	24	35	61	92	310	499	667	984
40 MHz	27	40	70	105	355	570	762	1124
45 MHz	31	45	79	119	399	641	857	1265
50 MHz	34	50	88	132	443	712	952	1405
55 MHz	38	55	96	145	488	783	1048	1546
60 MHz	41	60	105	158	532	855	1143	1686

#### Frame Rate Calculation

To calculate the frame rate for any clock rate the equation is:

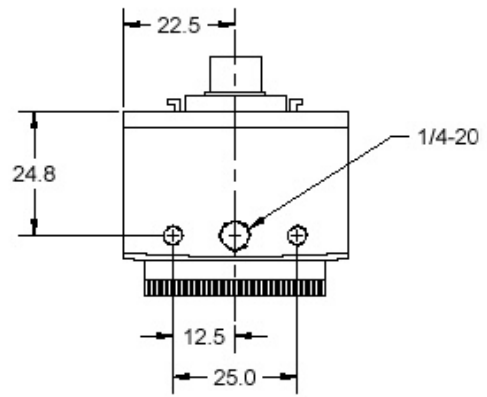
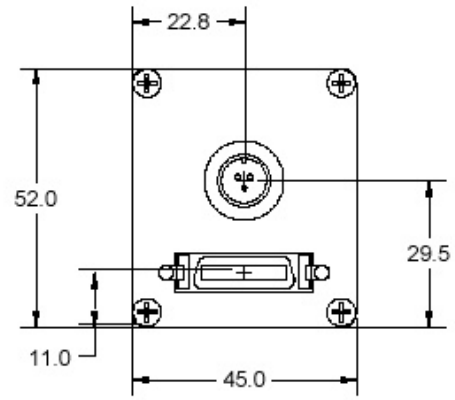
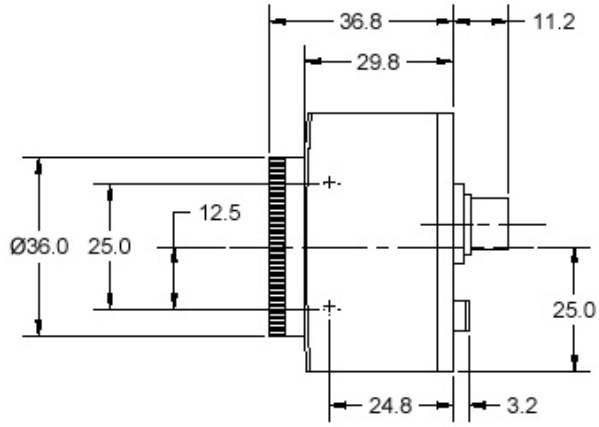
$$\frac{\text{clock rate(Hz)}}{(\# \text{ of columns} + 150) * (\# \text{ of rows})} = \# \text{ Frames Per Second (fps)}$$

**Example:** What is the frame rate, at 60MHz clock rate for an image size of 800 x 600?

$$\frac{60 \times 10^6}{(800 + 150) * (600)} = 105 \text{ Frames Per Second (fps)}$$

\*\* FRAME RATES are based on ROLLING SHUTTER operation. Full-Frame Shutter requires the additional time for exposure for each frame. Subsampling frame rates are based on the resulting size of the subsampled image or window.

## Camera Dimensions



# CMOS Chip

## MegaCamera \ Sensor Mounting 33x44

February 15, 2003

